

---

# MATRIX-PRODUCT-STATE BASED STUDIES OF BOSONIC FLUX LADDERS

Maximilian Buser

---



München, 2021



---

MATRIX-PRODUCT-STATE BASED STUDIES OF  
BOSONIC FLUX LADDERS

---



Dissertation

an der Fakultät für Physik

der Ludwig-Maximilians-Universität München

vorgelegt von

MAXIMILIAN BUSER

München, den 11.02.2021

Erstgutachter: Prof. Dr. Ulrich Schollwöck  
Zweitgutachter: Prof. Dr. André Eckardt  
Abgabedatum: 11.02.2021  
Datum der mündlichen Prüfung: 12.04.2021

# Zusammenfassung

Flussleitermodelle beschreiben das komplexe Zusammenspiel von wechselwirkenden quantenmechanischen Teilchen, die sich unter dem Einfluss von effektiven Magnetfeldern in quasi-eindimensionalen Gittern bewegen. In den letzten Jahren konnten diese Modelle in optischen Gittern durch die Erzeugung von künstlichen Magnetfeldern für kalte Atome experimentell realisiert werden. Flussleitermodelle sind aufgrund ihrer formalen Einfachheit, ihrer reichhaltigen Phasendiagramme und gegenwärtiger Quantengasexperimente von großem Interesse. Die vorliegende Arbeit befasst sich mit der theoretischen Untersuchung von bosonischen Flussleitermodellen unter Verwendung numerischer Methoden, die auf Matrixproduktzuständen basieren. Wir erkunden Grundzustandsphasendiagramme mit dem Verfahren der Dichtematrix-Renormierungsgruppe. Darüber hinaus untersuchen wir thermische Zustände sowie dynamische Vielteilchenprobleme in Flussleitern mithilfe moderner Zeitentwicklungsmethoden.

In einem einleitenden Teil dieser Arbeit wird das zentrale bosonische Flussleitermodell in den breiteren Forschungskontext eingeordnet. Wir diskutieren dessen wesentliche Eigenschaften und stellen die in dieser Arbeit verwendeten numerischen Methoden vor. Im Anschluss präsentieren wir die gewonnenen Forschungsergebnisse wie folgt.

Zunächst liegt der Fokus auf Modellparametern, die durch ein angedachtes Experiment motiviert sind. In dem Experiment soll eine zweibeinige bosonische Flussleiter unter der Ausnutzung interner Spinzustände von kalten bosonischen Kaliumatomen realisiert werden. Wir zeigen, dass das zugehörige Grundzustandsphasendiagramm eine Mott-isolierende Meissner-Phase sowie superfluide und Mott-isolierende Biased-Ladder-Phasen aufweist. Mithilfe zeitabhängiger Simulationen demonstrieren wir, dass realistische Quantenquenchprotokolle es erlauben, Gleichgewichtseigenschaften der relevanten Grundzustandsphasen in der transienten Vielteilchendynamik zu beobachten und zu quantifizieren.

Im Weiteren untersuchen wir die Quantenzustände von Flussleitern bei endlichen Temperaturen. Während die Nulltemperaturphasen von Flussleitermodellen im Zentrum zahlreicher theoretischer Arbeiten stehen, bleibt der Einfluss von Temperatureffekten auf die charakteristischen Grundzustandseigenschaften weitestgehend unerforscht. Dieser Einfluss spielt in Experimenten allerdings eine wichtige Rolle. Um die bei endlichen Temperaturen angenommenen Quantenzustände zu untersuchen bedienen wir uns einer Matrixproduktzustandsmethode, die im Rahmen dieser Arbeit im-

plementiert wurde. Unsere Studie konzentriert sich auf chirale Randströme und charakteristische Quasiimpuls-Verteilungen, die in gegenwärtigen Quantengasexperimenten gemessen werden können. Für stark wechselwirkende Bosonen und ausgehend von dem Quantenphasenübergang von einer Vortex-Phase zu einer Meissner-Phase erarbeiten wir das zugehörige Crossoverdiagramm bei endlichen Temperaturen.

Darüber hinaus untersuchen wir die Hall-Antwort bosonischer Flussleitermodelle. Flussleitern sind die minimalsten Gittermodelle, in denen sich ein Hall-Effekt untersuchen lässt. Dessen ungeachtet ist die Frage nach der Hall-Antwort in Quantenphasen, die auf Vielteilcheneffekten beruhen, theoretisch schwierig und Gegenstand aktueller Forschung. Vor dem Hintergrund gegenwärtiger Quantengasexperimente berichten wir über zeitabhängige Protokolle, mit denen sich Messungen der Hall-Polarisation auf Messungen der Hall-Spannung erweitern lassen. Durch umfangreiche numerische Simulationen zeigen wir, dass die Hall-Spannung in verschiedenen Quantenphasen eine große Robustheit im Hinblick auf die Wechselwirkungsstärke und die Teilchenfüllung aufweist. Diese Robustheit lässt sich in der Hall-Polarisation nicht beobachten. Wir untermauern unsere numerischen Ergebnisse mit semiklassischen Rechnungen und diskutieren die lokal aufgelöste Hall-Antwort in räumlich inhomogenen Vortexgitter-Phasen.

Abschließend fassen wir die gewonnenen Ergebnisse kurz zusammen und erwähnen Folgestudien, die unmittelbar mit der vorliegenden Arbeit in Verbindung stehen.

# Abstract

Flux ladders constitute the minimal setup enabling a systematic understanding of the rich physics of interacting particles subjected simultaneously to a strong magnetic field and a lattice potential. The recent realization of flux ladders in ultracold quantum gases with artificial magnetic fields has attracted great interest. In this thesis, we study various aspects of interacting bosonic flux ladders using extensive matrix-product-state based calculations. Specifically, the numerical techniques include the variational ground-state optimization by means of the density-matrix renormalization-group method, a purification approach for the study of finite-temperature states, as well as time-evolution methods for the simulation of quench dynamics.

In an introductory part, we recapitulate key features and important ground-state phases of the flux-ladder model and discuss the numerical methods. Subsequently, the main results are presented as follows.

First, the emphasis is put on model parameters which are envisioned to be realized in a future quantum gas experiment exploiting the internal states of potassium atoms as a synthetic dimension. Considering a particle filling of one boson per rung, we map out the ground-state phase diagram and report on a Mott-insulating Meissner phase as well as on biased-ladder phases, which might exist on top of superfluids and Mott insulators. Moreover, we demonstrate that quantum quenches of suitably chosen initial states can be used to probe the equilibrium properties in the transient dynamics. Concretely, we consider the instantaneous turning on of particle hopping along the rungs or legs in the synthetic flux-ladder model, with different initial particle distributions. We show that clear signatures of the biased-ladder phase and the Meissner phase can be observed in the transient dynamics.

Second, we study the effect of finite temperatures in flux ladders. So far, most of the theoretical work on these systems has concentrated on zero-temperature phases while the finite-temperature regime remains largely unexplored. However, the question if and up to which temperature characteristic features of the ground-state phases persist is relevant in experimental realizations. In order to explore the finite-temperature regime, a matrix-product-state based purification approach for the simulation of strongly interacting bosons has been implemented. Our study is focused on chiral currents and momentum-distribution functions, which are key observables in ultracold quantum gases, and our main results concern the most prominent vortex liquid-to-Meissner crossover. We demonstrate that signatures of the vortex-liquid phase can still be detected at elevated temperatures from characteristic finite-momentum maxima in the

momentum-distribution functions, while the vortex-liquid phase leaves weaker fingerprints in the chiral current. In order to determine the range of temperatures over which these signatures can be observed, we introduce a suitable measure for the contrast of these maxima. The results are condensed into a finite-temperature crossover diagram.

Third, we investigate the Hall response in bosonic flux ladders. While flux ladders are the most simple lattice models giving rise to the Hall effect, the theoretical description of the many-body ground-state Hall response in these systems remains a tricky problem and an active line of research. In view of current quantum gas experiments, we discuss feasible schemes to extend measurements of the Hall polarization to a study of the Hall voltage, allowing for direct comparison with solid state systems. Most importantly, we report on characteristic zero crossings and a remarkable robustness of the Hall voltage with respect to interaction strengths, particle fillings, and ladder geometries, which is unobservable in the Hall polarization. Moreover, we investigate the site-resolved Hall response in spatially inhomogeneous quantum phases using a semiclassical approach.

In conclusion, we present a brief summary of our work and touch on possible follow-up studies which are directly connected to the contents of this thesis.

# Publications

In the following, you can find a complete list of the author's publications and preprints [1–6]. Published articles are in inverse chronological order. This thesis is based on publications marked with a star (★), which are partially reprinted. Publications marked with a dagger (†) are not treated in this thesis.

**Probing the Hall Voltage in Synthetic Quantum Systems (★)**

Maximilian Buser, Sebastian Greschner, Ulrich Schollwöck, and Thierry Giamarchi  
Physical Review Letters **126**, 030501 (2021) [1]

**Interacting bosonic flux ladders with a synthetic dimension:  
Ground-state phases and quantum quench dynamics (★)**

Maximilian Buser, Claudius Hubig, Ulrich Schollwöck, Leticia Tarruell,  
and Fabian Heidrich-Meisner  
Physical Review A **102**, 053314 (2020) [2]

**Finite-temperature properties of interacting bosons on a two-leg flux ladder (★)**

Maximilian Buser, Fabian Heidrich-Meisner, and Ulrich Schollwöck  
Physical Review A **99**, 053601 (2019) [3]

**Initial system-environment correlations via the transfer-tensor method (†)**

Maximilian Buser, Javier Cerrillo, Gernot Schaller, and Jianshu Cao  
Physical Review A **96**, 062122 (2017) [4]

**Nonequilibrium quantum transport coefficients and transient dynamics of full counting  
statistics in the strong-coupling and non-Markovian regimes (†)**

Javier Cerrillo, Maximilian Buser, and Tobias Brandes  
Physical Review B **94**, 214308 (2016) [5]

**Bosonic Pfaffian State in the Hofstadter-Bose-Hubbard Model (†)**

Felix A. Palm, Maximilian Buser, Julian Léonard, Monika Aidelsburger,  
Ulrich Schollwöck, and Fabian Grusdt  
arXiv:2011.02477 [6]

# Acknowledgements

First of all, I would like to thank Professor Uli Schollwöck for the chance to join his group and his mentorship. I highly appreciate his support and advice.

I am grateful to Professor Fabian Heidrich-Meisner for the supervision of our joint projects. Our papers vastly profited from his efforts. I am also thankful to Professor Leticia Tarruell for our collaboration, the chance to visit her group in Castelldefels, and her valuable feedback.

It was a great experience to work with Sebastian Greschner and Professor Thierry Giamarchi. I would like to thank them for our discussions, valuable feedback, and the chance to visit Professor Thierry Giamarchi's group in Geneva.

I would like to thank Professor André Eckardt for the kind invitation to visit his group in Dresden and for examining this thesis. Professor Monika Aidelsburger and Professor Dieter Braun kindly agreed to be a part of the examination board, which is gratefully acknowledged.

I am thankful to Cordula Weber for her kind and patient support concerning all administrative tasks.

Over the last years, I have had the great pleasure to exchange ideas with many companions. Here, in particular, I would like to thank Leo Stenzel, Botao Wang, Rajah Nutakki, and Felix Palm for helpful comments on my work.

Collaborating with Fabian Grusdt and with the other members of his young group is a great experience. I would like to thank him for our discussions, his support, and for creating a positive and motivating atmosphere.

Finally, I would like to thank Gernot Schaller, Professor Tobias Brandes, Professor Jianshu Cao, and, most importantly, Javier Cerrillo, from whom I had the chance to learn before moving to Munich.



# Contents

<b>Zusammenfassung</b>	<b>iii</b>
<b>Abstract</b>	<b>v</b>
<b>Publications</b>	<b>vii</b>
<b>Contents</b>	<b>x</b>
<b>1 Introduction</b>	<b>1</b>
1.1 Quantum states of matter . . . . .	3
1.2 Quantum simulation . . . . .	8
1.3 Flux ladders . . . . .	14
1.4 Outline of this thesis . . . . .	17
<b>2 Flux-ladder model</b>	<b>19</b>
2.1 Model Hamiltonian . . . . .	19
2.1.1 Noninteracting model . . . . .	20
2.1.2 Observables of interest . . . . .	22
2.2 Ground-state phases in the presence of interactions . . . . .	25
<b>3 Numerical methods</b>	<b>29</b>
3.1 Quantum states and entanglement . . . . .	29
3.2 Matrix-product states . . . . .	32
3.3 Density-matrix renormalization-group method . . . . .	40
3.4 Finite-temperature calculations with matrix-product states . . . . .	42
3.5 Time-propagation of matrix-product states . . . . .	46
<b>4 Interacting bosonic flux ladders with a synthetic dimension</b>	<b>49</b>
4.1 Specifics of the experimental implementation . . . . .	49
4.2 Zero-temperature phase diagram . . . . .	52
4.3 Quench dynamics . . . . .	61
4.3.1 Probing the chiral current . . . . .	62
4.3.2 Signatures of the biased-ladder phase . . . . .	64
4.4 Summary . . . . .	67
<b>5 Vortex-to-Meissner crossover at finite temperatures</b>	<b>69</b>

<b>Contents</b>	<b>xi</b>
5.1 Noninteracting bosons . . . . .	70
5.2 Noninteracting fermions . . . . .	74
5.3 Hard-core bosons . . . . .	76
5.4 Summary . . . . .	81
<b>6 Probing the Hall voltage in synthetic quantum systems</b>	<b>83</b>
6.1 The Hall response in few-leg flux ladders . . . . .	84
6.2 Measuring the Hall voltage . . . . .	87
6.3 Interacting systems . . . . .	90
6.4 Rung-resolved Hall response . . . . .	95
6.5 Robustness of the Hall voltage . . . . .	98
6.6 Numerical approach . . . . .	100
6.7 Summary . . . . .	101
<b>7 Conclusion and outlook</b>	<b>103</b>
<b>References</b>	<b>107</b>



# Introduction

## A brief overview

The understanding and design of quantum materials is one of the biggest challenges of modern physics. While the underlying laws of quantum mechanics, which govern the interplay of the atomic constituents of all material objects, are well established, the mathematical treatment of quantum mechanical systems comprising just a few of these basic constituents is well known to be quite challenging [7]. Furthermore, various physical phenomena emerging in systems of increasing size and complexity are hardly predictable from these basic laws [8–10]. Studying suitable representations of physical systems at a carefully chosen level of abstraction is at the heart of theoretical physics. In this sense, quantum lattice models are ideal theoretical laboratories for the exploration of novel quantum states of matter and a cornerstone of condensed matter physics. The lattice sites of these models typically represent local quantum degrees of freedom, such as the orientation of a local spin or the presence of a certain type of particle, while the edges of the underlying lattice represent Hamiltonian interactions, which determine the overall behavior of the models.

Arguably, one of the most famous examples of a quantum lattice model is the Fermi-Hubbard model [11–13], which accounts for interacting electrons hopping between neighboring lattice sites. The Fermi-Hubbard model is based on only two parameters, namely the particle hopping strength and the site-local interparticle interaction strength. Nonetheless, it captures a broad range of phenomena, including the emergence of insulating and magnetic phases, which arise due to the interplay of many electrons and cannot be described in a single-particle framework. Its two-dimensional variant is considered to play an essential role in the understanding of high-temperature superconductivity [14]. Traditionally, there is great interest in Hubbard-like models because they are effective representations of solid state systems exhibiting a crystalline arrangement of localized atomic cores and tightly bound valence electrons. Despite their formal simplicity when written down, quantum many-body lattice models are mathematically challenging. Exact solutions have indeed been found only for exceptional cases, and, throughout the last decades, extensive efforts have focused on the development and optimization of various numerical methods addressing quantum many-body lattice problems.

Complementary to theoretical efforts, an alternative path to the study of challenging lattice systems is provided by so-called quantum simulators [15]. These simulators are

engineered and controllable quantum devices which faithfully realize specific Hamiltonians of interest. Ultracold quantum gases are a particularly promising platform for this purpose [16–18]. Impressive advances in the field of cooling, trapping, and controlling atomic gases have enabled the simulation of almost arbitrary condensed matter toy models in optical lattices, which are built from the interference patterns of counter-propagating laser beams. A first milestone in the field of quantum simulation with cold atoms was achieved in 2002 with the observation of the superfluid-to-Mott insulator transition in the bosonic variant of the Hubbard model [19].

Magnetic fields can drastically alter the behavior of solid state systems. This is best exemplified by the integer [20] and fractional quantum Hall effect [21] in two-dimensional electron gases. While varying the strength of a magnetic field at low temperatures, the integer quantum Hall effect reveals extended plateaus with an amazingly precise quantization of the Hall conductivity. Importantly, the quantum Hall states corresponding to different plateaus cannot be distinguished by means of local order parameters and the concept of spontaneous symmetry breaking. After the unexpected discovery of these effects in the 1980s, it has become clear that they are rooted in the topological ground-state properties of the underlying two-dimensional systems [22–24]. Topological properties of quantum states occupy a central position in modern condensed matter research.

In quantum lattice models, an effective magnetic field can be directly incorporated by means of complex phase factors accompanying the particle-hopping terms, employing Peierls substitution [25]. A prime example is the noninteracting Hofstadter model, accounting for charged particles hopping in a two-dimensional square lattice which is pierced by a magnetic field [26]. The Hofstadter model is famous for its fractal energy spectrum referred to as Hofstadter’s butterfly and has played an important role in the study of the quantum Hall effect. Over the last decade, Hofstadter-like models with artificial magnetic fields for charge-neutral atoms have been realized in optical lattice experiments [27–29]. In these experiments, the complex Peierls phase factors accompanying the hopping terms are directly implemented, which also enables the emulation of arbitrarily strong magnetic fields [30, 31].

Flux ladders, which are at the focus of this thesis, are the most simple quantum lattice models which incorporate the effect of a magnetic field. They can be thought of as quasi-one-dimensional variants of the two-dimensional square-lattice Hofstadter model with a reduced width such that ladderlike structures with only a few legs remain. Due to the interplay of lattice effects, effective magnetic fields, and interparticle interactions, flux ladders host rich physics and a myriad of ground-state phases. However,

it should be stressed that in the crossover from two spatial dimensions to one spatial dimension the topological properties of the Hofstadter model blur out. Flux ladders are currently particularly relevant because of their recent realization in various quantum gas experiments with artificial magnetic fields. Moreover, in contrast to the case of extended two-dimensional systems, the classical simulation of quasi-one-dimensional flux ladders is computationally much more feasible. Matrix-product-state based algorithms are especially well suited for this purpose. Most notably, the density-matrix renormalization-group method [32–35] enables the efficient calculation of ground states, while state-of-the-art time-evolution methods [36] allow for the simulation of quantum many-body dynamics and, with a few adaptations, also for the calculation of finite-temperature states. These methods can provide guidance for future experimental realizations of flux ladders in quantum-gas simulators.

The objective of the remainder of this introductory chapter is to put our work on flux-ladder systems, which will be presented throughout the following chapters, into a broader context. In particular, we focus on the characterization of different quantum states of matter, the concept of quantum simulation, as well as on experimental realizations and open questions which are related to flux-ladder systems.

## 1.1 Quantum states of matter

As opposed to classical thermal states and phases of matter, which, in the broad framework of thermodynamics, are described and controlled by macroscopic parameters at finite temperatures, quantum phases of matter typically refer to classes of fundamentally different ground states of quantum mechanical systems. These ground states are formally attained at zero temperature and the quantum phases are governed by Hamiltonian parameters, which are part of a microscopic description. Finding adiabatic connections represents an effective way for distinguishing between different gapped quantum phases. Two Hamiltonians are considered to correspond to the same gapped quantum phase if and only if they can be adiabatically connected. This means that by smoothly varying a model parameter, the two Hamiltonians can be transformed into each other while maintaining a finite gap in the energetic spectrum between the ground state and the excited states. The latter especially needs to hold in the limit of infinite system sizes, commonly referred to as the thermodynamic limit.

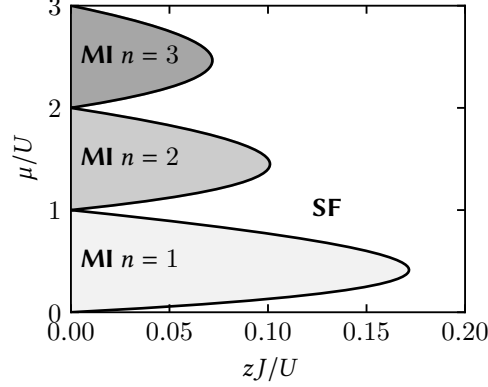


**Figure 1.1: Ground-state phase diagram of the mean-field Bose-Hubbard model.** The phase diagram shows incompressible Mott-insulating lobes (MI) with  $n = 1, 2,$  and 3 particles per lattice site and the compressible superfluid phase (SF). The different phases are indicated by different background shadings. The mean-field analysis predicts a continuous onset of the mean-field order parameter, which might be interpreted as  $\langle a_i \rangle$ , when entering the superfluid phase. Note that  $z$  denotes the coordination number, that is, the number of nearest neighbors around each lattice point. A comprehensive discussion of the mean-field analysis of the Bose-Hubbard model can be found, for instance, in Ref. [37].

### Ground-state phases of the Bose-Hubbard model

As a first example, we discuss the different quantum phases of the Bose-Hubbard model [38], which is the underlying model of the bosonic flux-ladder systems studied in the main part of this thesis. The Bose-Hubbard model accounts for interacting bosons hopping between neighboring sites of a discrete lattice. It is of practical importance because it is a suitable description of ultracold bosonic atoms trapped in laser-induced lattice potentials [16, 39, 40]. In terms of bosonic annihilation (creation) operators  $a_i$  ( $a_i^{(\dagger)}$ ), which act on different lattice sites labeled by  $i$ , the Hamiltonian of the Bose-Hubbard model reads

$$H = -J \sum_{\langle i, j \rangle} (a_i a_j^\dagger + a_j a_i^\dagger) + \frac{U}{2} \sum_i a_i^\dagger a_i (a_i^\dagger a_i - 1) - \mu \sum_i a_i^\dagger a_i. \quad (1.1)$$

The first term of the Hamiltonian accounts for particle hopping between neighboring lattice sites, which are denoted by  $\langle i, j \rangle$ , and  $J$  represents the hopping strength. The second term accounts for repulsive ( $U > 0$ ) interactions between two or more bosonic particles occupying the same lattice site, and  $\mu$  denotes the chemical potential.

The ground states of the Bose-Hubbard model which are attained in the limit of strong interparticle interactions,  $J/U \rightarrow 0$ , and in the limit of weak interactions,  $U/J \rightarrow 0$ , can be readily understood.

For vanishing interparticle interactions,  $U = 0$ , all bosonic particles condense in the zero-quasimomentum state with lowest kinetic energy. For lattices with periodic boundary conditions and a fixed number of  $N$  particles, the fully delocalized ground state is explicitly given by

$$|\psi\rangle = \frac{1}{\sqrt{N!}} \left( \frac{1}{\sqrt{N_L}} \sum_i a_i^\dagger \right)^N |\text{vac}\rangle, \quad (1.2)$$

where  $N_L$  denotes the total number of lattice sites and  $|\text{vac}\rangle$  is the zero-particle vacuum state.

In the limit of strong interparticle interactions,  $J/U \rightarrow 0$ , one finds Mott-insulating ground states. For  $J = 0$  they are of the product form

$$|\psi\rangle = \prod_i \frac{1}{\sqrt{n!}} (a_i^\dagger)^n |\text{vac}\rangle, \quad (1.3)$$

where  $n$  is a positive integer. Hence, for  $J = 0$  each lattice site is occupied by exactly  $n$  particles. Concretely, the overall particle density per lattice site  $\nu (= n)$  is given by

$$\nu = \lfloor 1 + \mu/U \rfloor. \quad (1.4)$$

Here, we stress that the defining property of a Mott-insulating state is that it is incompressible, meaning that  $\partial\nu/\partial\mu = 0$ . Mott-insulating states are gapped with respect to the addition or subtraction of a particle.

Most importantly, for small but finite values of the hopping strength  $J$ , the  $J = 0$  insulators adiabatically extend to stable incompressible regions with integer particle density  $\nu = n$ , referred to as Mott lobes. The Mott lobes are surrounded by a gapless and compressible superfluid phase. For large systems with a fixed average particle density, as in the experiment from Ref. [19], the superfluid state can be well described by a product of local coherent states [16]. An analysis of the Mott insulator-to-superfluid transition on the mean-field level predicts the phase diagram shown in Fig. 1.1 [37]. There, one finds a continuous onset of the mean-field order parameter, which might be interpreted as  $\langle a_i \rangle$ , when entering the superfluid phase. In general, the shape of the Mott lobes depends on the details of the underlying lattice. For a two-dimensional square lattice and for a three-dimensional cubic lattice, the true  $\mu/U$  versus  $J/U$  phase diagrams of the Bose-Hubbard model look very similar to the mean-field result with

only quantitative differences [41]. Except for a single point at the tip of the Mott lobes, the particle density changes when crossing the boundary between a Mott-insulating phase and the superfluid phase. For the case of a one-dimensional lattice, the Mott lobes exhibit a clear cusp indicating the point of constant integer particle density when going from the Mott-insulating phase to the superfluid phase. There, the transition is of the Kosterlitz-Thouless type [42, 43] and the precise localization of the critical point is rendered difficult because of the very slow closing of the energy gap as a function of  $J/U$  [44].

### Topological quantum states

Throughout the last forty years, topological quantum states of matter, which cannot be characterized by local order parameters, have attracted much attention. From a historical perspective [45], topological quantum states first appeared in the early 1980s with the unexpected experimental discovery of the integer [20] and fractional quantum Hall effect [21] in two-dimensional electron gases and with the theoretical studies of integer quantum spin chains [46–48]. Roughly speaking, topological quantum states are defined by means of their global properties. Topological properties give rise to fascinating effects, including the precisely quantized value of the conductance in the integer quantum Hall effect and fractionally charged quasiparticles in the fractional quantum Hall effect [49]. Anyonic quasiparticle excitations of topologically ordered states are at the core of proposals for the realization of inherently fault-tolerant quantum computers [50, 51].

Many topological quantum phases can be understood in the absence of interparticle interactions. An important early result is the one by David Thouless, Mahito Kohmoto, Marcel den Nijs, and Peter Nightingale which is typically referred to as the TKNN equation [22]. For the noninteracting square-lattice Hofstadter model defined on a torus, it directly relates the linear-response conductivity to the Chern number accounting for all occupied bands below the Fermi energy. The Chern number is a bulk topological invariant, defined as an integral in quasimomentum space [23, 24]. Importantly, it takes on integer values and the TKNN equation reflects the physics observed in the integer quantum Hall effect [20]. While the Hofstadter model explicitly accounts for the effect of a uniform magnetic field, in 1988 Haldane put forward his famous honeycomb-lattice model demonstrating that topological quantum states can also be realized in the absence of a magnetic field [52]. It is worth noting that the Haldane model exhibits complex next-nearest-neighbor hopping terms which add up to a zero total magnetic flux per unit cell. But, these terms break time-reversal symmetry and give rise to nonzero Chern

numbers ( $\pm 1$ ) [53]. In 2004, Kane and Mele predicted the quantum spin Hall effect with spin-dependent charge transport in gapless edge states, focusing on a time-reversal symmetric extension of the Haldane model [54, 55]. Three years later, the quantum spin Hall effect was first observed experimentally in HgTe quantum wells by Molenkamp and coworkers [56]. The quantum spin Hall states are classified as symmetry-protected topological insulators [57].

Aside from noninteracting topological insulators, the class of symmetry-protected topological states also includes ground states of interacting integer quantum spin chains [46–48, 58–60]. Here, a prime example is the ground state of the AKLT model, which is an extension of the one-dimensional spin-one Heisenberg model going back to Ian Affleck, Tom Kennedy, Elliott H. Lieb, and Hal Tasaki [61, 62]. Most importantly, the ground state of the AKLT model exhibits a hidden nonlocal string order. While it is gapped for periodic boundary conditions, it features gapless spin-one-half edge states for the case of open boundaries. Due to its entanglement spectrum, the ground state of the AKLT model can be efficiently expressed as a matrix product state with bond dimension 2.

In general, entanglement plays a crucial role for the classification of different topological quantum states. As comprehensively discussed by Chen et al. [63], symmetric versus symmetry-broken states of local Hamiltonians are additionally distinguished by different patterns of short-range versus long-range entanglement. In this framework, ground states corresponding to the same topological phase can be adiabatically connected via local unitary transformations, which need to satisfy the symmetry constraints of the underlying model. Along these lines, topologically trivial short-range entangled states can be connected with unentangled product states. In contrast, fractional quantum Hall states, exhibiting intrinsic topological order, are long-range entangled and cannot be transformed into short-range entangled states by means of local unitary transformations.

In anticipation of the results that will be presented throughout this thesis, we conclude this overview with a few remarks. Topological quantum states of matter represent a vast and active field of research. A comprehensive discussion of this topic is far beyond the scope of this thesis and in the above we merely touched on a few important examples. Most of all, we stress that the notion of topological quantum states is by no means of importance for the understanding of the contents of this thesis. Despite the apparent similarity between the two-dimensional Hofstadter model and the flux ladders studied in the next chapters, the topological properties blur out in the transition to one spatial dimension. Hence, topological properties play no role for the classification of the

different ground-state phases of the few-leg flux ladders considered in the following. Nonetheless, it is worth noting that flux ladders can be extended in order to give rise to topologically nontrivial ground states. This can be achieved, for instance, by increasing the width of the ladders in order to restore the two-dimensional Hofstadter systems and their interacting analogues or by introducing diagonal coupling terms [64].

## 1.2 Quantum simulation

Given the notorious difficulty of simulating quantum systems with classical computers [65], the concept of quantum simulators has intrigued physicists throughout the last decades [15, 66–69]. Currently, reports claiming the practical achievement of the so-called quantum computational advantage are attracting great interest. Achieving the quantum computational advantage means that a controllable quantum device performs a well defined — but not necessarily useful — task which is intractable for classical computers [70, 71]. In the following, we first touch on two recent experiments which have made headline news claiming the demonstration of the quantum computational advantage. These experiments are not related to the contents of this thesis, but, here, they show that quantum simulators are implemented on a wide variety of physical platforms. We then discuss the difficulty of classically simulating quantum lattice systems and introduce digital and analog quantum simulators in more depth. Subsequently, we turn to quantum-gas platforms, in which flux-ladder models have been successfully realized, and touch on the concept of Floquet engineering, which plays a crucial role for the implementation of complex hopping terms.

### The ongoing race for demonstrations of the quantum computational advantage

The recent experiments by Martinis and coworkers using a 53 qubit processor [72] and by Pan, Lu, and coworkers performing Gaussian boson sampling [73] are prime examples of the ongoing efforts aiming at practical demonstrations of the quantum computational advantage. Quantum sampling problems, which are considered in the experiments, are particularly well-suited tasks for such demonstrations [74–76].

In October 2019, the team around John M. Martinis working with Google claimed the first demonstration of the quantum advantage using a processor with 53 superconducting qubits named Sycamore [72]. In the experiment, the qubits were entangled by repeatedly applying single-qubit and two-qubit gates in a circuit of depth 20 and with a predicted overall fidelity of  $2 \times 10^{-3}$ . Sampling the quantum circuit one million times takes the Sycamore processor around 200 seconds. The authors estimate that this task

would take thousands of years to be simulated on a state-of-the-art classical supercomputer. This estimate, however, is challenged by Pednault et al. [77] claiming that with an optimized architecture two days would be sufficient for the corresponding classical simulation. Employing matrix-product states, Zhou et al. [78] argue that realistic quantum computers, which are similar to the Sycamore device and which suffer from decoherence and imprecision, can be simulated using a tiny fraction of the computational resources that would be needed for the classical simulation of a perfect quantum computer.

The 2020 Gaussian boson sampling experiment carried out by Pan, Lu, and coworkers [73] involves a 100-mode interferometer with 50 ingoing single-mode squeezed states. The quantum device named Jiuzhang samples the output with up to 76 photon clicks, extending previous smaller experiments [79–81]. A simulation of the experiment is considered unlikely to be feasible on a classical supercomputer [82]. As compared to the controllable superconducting Sycamore processor, which, in 2020, was also employed for a concrete quantum chemical calculation [83], the photonic platform Jiuzhang is less versatile. We note that these experiments are not related to the results presented in this thesis, but they show the great variety of modern quantum simulators.

### Classical simulation of quantum lattice models

Theoretical studies of quantum lattice models are rendered inherently difficult because of the exponential growth of the Hilbert space with the number of lattice sites. For a system comprising  $L$  lattice sites with  $d$  site-local degrees of freedom, the Hilbert space has dimension  $d^L$ . This corresponds to the number of complex parameters required to represent a quantum state. Thus, the exponential scaling naturally limits exact diagonalization approaches on classical computers because by increasing the system size the state vector quickly becomes too large to be stored in memory.

Here, it is worth noting that most condensed matter toy models exhibit symmetries, whose exploitation is key in numerical studies [84]. It is illustrative to consider a spin-one-half Heisenberg model with  $L$  lattice sites which conserves the net magnetization along a chosen direction [85]. For this particular example, the underlying Hilbert space is spanned by  $2^L$  basis states. However, the Hamiltonian matrix of the Heisenberg model is block-diagonal with respect to the value of the net magnetization. The largest block, corresponding to the sector of zero net magnetization, comprises only  $\binom{L}{L/2}$  states. While an exact diagonalization of the Hamiltonian remains infeasible for large or even moderate system sizes, this example shows that quantum lattice problems can

be approached more efficiently by treating the different quantum symmetry sectors independently.

Numerical approaches applicable to larger systems, which cannot be diagonalized exactly, include, most notably, quantum Monte Carlo techniques [86] and methods which are based on a physically motivated selection of a suitable subspace of the full Hilbert space. Quantum Monte Carlo techniques practically employ a stochastic sampling of the state space. A major difficulty of quantum Monte Carlo methods is the infamous sign problem, which is encountered in various situations. Matrix-product-state methods and, more generally, tensor-network-state approaches, are effectively applicable to quantum states which are found in the corner of Hilbert space which exhibits little entanglement [87]. They are ultimately limited by the growth of the entanglement of the quantum states of interest. Matrix-product states are discussed in detail in Ch. 3.

### **Analog and digital quantum simulators**

Quantum simulators are synthetic devices which simulate and solve specific problems. Importantly, they exploit inherently quantum-mechanical features, such as superposed and entangled quantum states, which do not have a classical analogue. As compared to the simulation by means of classical computers, the resources required for a direct quantum simulation should not scale exponentially with the size of the specific problem at hand. While the state vector of a, say, 72-qubit system cannot be stored on a classical computer it might be processed with a quantum device.

Typically, quantum simulators operate as follows. First, an initial state is prepared. Second, the initial state is transformed during a time evolution. The time evolution might be governed by a time-independent or by an explicitly time-dependent Hamiltonian. Also, it might include quantum quenches and operations resembling the application of quantum logic gates. Third, the transformed final state is probed by means of a projective measurement. Thus, quantum simulators need to be able to effectively prepare a suitable initial state, implement the desired Hamiltonian required for the time evolution, and allow for a direct measurement of the relevant observables for the underlying problem. The latter requirement is underlined by the fact that quantum state tomography is typically not feasible in practice because of the exponential scaling of the resources with the system size [88]. Overall, a major practical challenge for the construction of quantum simulators is their simultaneous need for controllability and scalability. On the one hand they need to be well controllable and eventually allow for measurements and readouts on the level of their individual constituents. On the other

hand they need to be scalable to large system sizes in order to solve problems which become intractable for classical computers.

Quantum simulators find concrete applications in the study of quantum lattice models and their phase diagrams. They have also been successfully employed for the controlled simulation of nonequilibrium dynamics in quantum many-body systems, which, for long simulation times, become intractable in classical numerical simulations [89]. Additionally, quantum simulators have proven useful for the study of quantum transport in multiterminal setups [90], which are reminiscent of conventional solid state systems. Furthermore, they might help answering open questions in the fields of quantum chemistry and quantum biology [83]. For instance, the simulation of vibrationally assisted charge or energy transfer plays an important role in the understanding of light-harvesting complexes [91].

Traditionally, there is a distinction between digital and analog quantum simulators [15]. On the one hand, devices implementing versatile quantum circuits with, in the ideal case, arbitrary single-qubit and two-qubit gates are referred to as digital quantum simulators. If these devices could overcome the practical difficulties of achieving long coherence times and large gate fidelities in order to faithfully realize deep circuits, they might be thought of as universal quantum computers [66]. On the other hand, analog quantum simulators are tailored towards the efficient emulation of specific model Hamiltonians. As compared to digital quantum simulators, analog quantum simulators are less versatile, typically allowing to control a few specific model parameters. However, analog simulators can naturally implement Hamiltonian interactions which are otherwise difficult to realize with elementary quantum gates. In spite of the traditional classification, present simulators are often of a rather hybrid nature, effectively bridging the gap between analog simulators with little tunability and universal digital quantum computers [69].

Quantum simulators have been realized in various physical platforms including the aforementioned superconducting [72] and photonic [73] devices. Different implementations are based on electron or nuclear spins. For instance, single electrons in quantum dots can be controlled by means of a magnetic detuning of their internal spin states, which realize a qubit, and by adjusting the Fermi level of the reservoirs [92]. The corresponding quantum gates can be implemented by means of a resonant magnetic or electric driving of the spin transition, while the readout is enabled by current measurements in nearby charge sensors, which indirectly depend on the presence and on the spin state of an electron in the quantum dot.

### Ultracold atoms in optical lattices

Ultracold atoms in optical lattices represent particularly successful analog quantum simulators, which are very well isolated from their environment [17, 18]. Optical lattices, in which the atoms are confined due to the optical dipole force, are built from the interference patterns of counterpropagating laser beams [93]. Superimposing several standing waves in different directions allows for the realization of various lattice structures, such as cubic-type [94], hexagonal [95], and Kagome lattices [96], as well as superlattice potentials [97]. Aside from the control of the lattice depth and geometry, interparticle interactions can be tuned by means of Feshbach resonances [98]. In 2002, a first milestone was reached by tuning the lattice-hopping strength versus the interparticle interaction strength of ultracold bosonic  $^{87}\text{Rb}$  atoms [19]. There, building up on the advances in the field of laser cooling and trapping ultracold gases [99, 100], Greiner et al. observed the quantum phase transition from a superfluid to a Mott insulator in a three-dimensional cubic lattice.

An appealing feature of ultracold atoms in optical lattices is that they can be probed in various ways. Most notably, a sudden release of the atoms from the optical lattice and subsequent time-of-flight imaging allows for measurements of quasimomentum-distribution functions, while quantum-gas microscopy enables site-resolved measurements of particle-density profiles in real space [16, 101, 102]. Single atoms and their spin can be individually addressed and controlled by means of quantum-gas microscopes in different lattice geometries [103, 104]. Moreover, digital micromirror devices combined with quantum-gas microscopes allow for the creation of almost arbitrary potentials on top of two-dimensional optical lattices [105]. The snapshots taken by quantum gas microscopes in the form of a projective measurement are attracting great interest. In order to study the underlying quantum phases, these snapshots are increasingly analyzed by means of data science tools, such as pattern-search algorithms [106] and artificial neural networks [107–110].

Quantum gases have also been exploited for the study of out-of-equilibrium dynamics in isolated quantum many-body systems [111–113]. The dynamics can be induced by instantaneous quenches, time-dependent ramps, or periodic driving. Typically, the entanglement of a quantum state increases during such a time evolution and quantum-gas simulators have proven to be able to outperform classical algorithms in the controlled simulation of nonequilibrium dynamics of even one-dimensional systems [89]. Of particular fundamental interest are questions concerning the effective thermalization of isolated quantum many-body systems and situations in which an effective thermalization does not occur [114–116]. There, important concepts are the eigenstate thermaliza-

tion hypothesis [117, 118] and the phenomenon of many-body localization [119, 120], in which states do not effectively thermalize.

### Floquet engineering of artificial magnetic fields

The last decade has witnessed tremendous progress in the realization of artificial magnetic fields in quantum engineered systems and the quantum simulation of iconic topological toy models [121–126]. Aside from superconducting circuits [127, 128] and photonic platforms [129–132], strong magnetic fields and spin-orbit coupling have been emulated in ultracold quantum gases [27–29, 133–151]. There, the independent realizations of the two-dimensional bosonic Hofstadter model by Aidelsburger et al. [28] and by Miyake et al. [29] are prime examples [31]. Theoretically, the implementation of the Hofstadter model with charge neutral atoms and laser-assisted tunneling in an energetically tilted optical lattice was first proposed by Jaksch and Zoller [30]. Moreover, the Haldane model [52], whose experimental realization had originally been considered unlikely, was implemented by Jotzu et al. [137] in 2013 and later by Asteria et al. [150], using the periodic modulation of an optical honeycomb lattice. In all of these experiments, time-periodic driving is key for the realization of effective model Hamiltonians with complex hopping terms [152]. A suitable arrangement of the complex hopping terms might account for an effective magnetic field in the sense that hopping particles gain Peierls phases, which add up to a finite magnetic flux when encircling a plaquette of the underlying lattice [25]. We emphasize that the 2017 review article by A. Eckardt [153] provides an overview of previous experimental works employing time-periodic driving in optical lattices and comprehensively discusses the underlying theoretical aspects.

Most importantly, Floquet engineering allows for the realization of models which otherwise cannot be statically implemented in certain physical platforms. The basic idea is to adjust the time-periodic driving of a quantum system in such a way that its stroboscopic dynamics are governed by an effective and time-independent Floquet Hamiltonian [154], representing the desired model. Concretely, a system's time-evolution operator for one driving period  $T$  is considered to be of the form

$$U(t_0 + T, t_0) = \exp\left(-iH_{t_0}^F T\right), \quad (1.5)$$

defining the Floquet Hamiltonian  $H_{t_0}^F$ , which explicitly depends on the initial time  $t_0$ . However, driven systems are different from their static counterparts: Eq. (1.5) does not uniquely determine  $H_{t_0}^F$ . Its eigenenergies are merely defined up to the addition of integer multiples of the driving frequency  $2\pi/T$ . This is reminiscent of the fact that

the energy is not conserved in driven systems. Indeed, heating represents a major problem in Floquet-engineered systems. In recent years, the understanding of heating and dissipation in periodically driven quantum-gas simulators has been at the focus of various experimental and theoretical works, as reported, for instance, in Refs. [155–162] and Refs. [163–165], respectively. Except for the case of many-body localized states, which represent a robust and noteworthy exception [166], the periodic driving of an isolated many-body system is expected to eventually lead to an infinite-temperature state due to the continual absorption of energy. Hence, a particular focus of current efforts, including many of the aforementioned studies, is the temporal delay of this ultimate heat death and the engineering of a long-lived prethermal period, in which a desired model Hamiltonian can be faithfully realized.

In the context of quantum lattice systems, Floquet engineering has not only been employed for the realization of artificial magnetic fields. Different applications include, for instance, the control of the superfluid-to-Mott insulator transition [167, 168] using the dynamical control of tunneling in optical lattices [169], which is related to early theoretical work by Dunlap and Kenkre [170].

In the framework of this thesis we mostly work with static flux-lattice toy-model Hamiltonians. However, it is important to keep in mind that in typical experiments these Hamiltonians actually need to be Floquet-engineered.

### 1.3 Flux ladders

Ladderlike systems are the natural candidates to study the intricate transition from one-dimensional to two-dimensional ground-state physics [171]. Moreover, two-leg ladders constitute minimal lattice models which might incorporate the effect of a magnetic field.

Using ultracold quantum gases, two-leg flux ladders were first realized in 2014 [136]. In the experiment, Atala et al. employed a superlattice potential for the isolation of ladder geometries in an underlying two-dimensional optical Hofstadter lattice. The experiment with weakly interacting  $^{87}\text{Rb}$  atoms enabled measurements of the chiral current, that is, the particle current encircling the flux ladder along its legs. By increasing the coupling strength between the two legs at a fixed value of the magnetic flux, a phase transition from a vortex phase to a Meissner phase, with different particle-current patterns, could be observed. The chiral currents and momentum-distribution functions observed in the experiment were in accordance with the theoretical predictions for a noninteracting model [64].

In addition to the use of superlattice potentials, the exploitation of a so-called synthetic dimension represents a further successful approach for the realization of flux ladders with cold atoms. It was originally proposed by Celi et al. [172], and the key idea is to employ the synthetic dimension spanned by the internal atomic spin degrees of freedom in order to represent the different legs of the ladder. In practice, the atoms are subjected to a one-dimensional periodic real-space potential, which is aligned with the legs of a ladder. Most importantly, the different legs are not spatially separated but correspond to the different internal states of the atoms. A coherent coupling of the internal states constitutes the rungs of the ladder. A great advantage of this approach is the natural realization of discrete sites and sharp boundary conditions along the synthetic dimension [173]. Synthetic flux ladders were first realized with bosonic [139] and with fermionic atoms [140] in 2015. Since then, they have been well established experimentally, using internal spin states [141, 145, 148] or other degrees of freedom [143, 146, 147] to implement the synthetic dimension. It was suggested that Chern numbers can be mapped out in multileg flux ladders with as few as five legs and open boundary conditions [174], which, in 2018, was experimentally demonstrated by Genkina et al. [149]. In another recent experiment performed by Chalopin et al. [151], which did not enforce a lattice potential in the real-space dimension but worked in the continuum, as many as 17 internal atomic states were exploited, putting the future realization of very wide flux ladders into prospect. While synthetic dimension implementations of flux ladders have been restricted to the noninteracting or to the weakly interacting regime, they are also considered promising candidates to access the interacting many-body regime.

Using a different quantum-gas setup, a first step in the direction of realizing many-body flux ladders with interparticle interactions was taken by Tai et al. [144]. In their experiment, employing a quantum-gas microscope combined with a digital micromirror device for the creation of an optical two-leg ladder potential in real-space [105], the dynamics of two repulsively interacting bosons could be observed.

Flux ladders, which are at the heart of this thesis, are very appealing from a theoretical perspective. They were first studied in the context of Josephson junction arrays [175–178]. In a seminal work from 2001, Orignac and Giamarchi show that the minimal bosonic two-leg flux ladder hosts ground-state phases which are reminiscent of a type-II superconductor [179]. A bosonization approach reveals that for weak magnetic fields the system is found to be in a Meissner phase with screening particle currents along the legs of the ladder, whereas vortex-lattice phases with current vortices are stabilized for stronger magnetic fields and weak but finite interparticle interaction strengths. The noninteracting analogues of these phases were realized in the experiment from

Ref. [136], triggering further theoretical studies of the flux-ladder model.

Due to the interplay between effective magnetic fields, interparticle interactions, and lattice effects, bosonic flux-ladder models exhibit rich ground-state phase diagrams. Aside from Meissner and vortex-lattice phases [180–183], which can exist on top of superfluids and Mott insulators, they host vortex-liquid phases [184], biased-ladder phases with a broken leg-inversion symmetry [185], and charge-density-waves with particle-density modulations along the legs [186, 187]. Precursors of fractional quantum Hall states in two-leg ladders have also attracted great interest [188–193]. They can be observed in a small window of parameters with a commensurate ratio between the particle density and the magnetic flux, leaving signatures in the particle currents. Arguably, by now, the ground-state phase diagrams of two-leg flux-ladder models have been discussed in detail and mapped out to a large extent within numerous theoretical studies [194–205]. Matrix-product states are particularly well suited for the numerical investigation of the ground-state physics of ladderlike systems, and in many of the aforementioned studies [195, 197, 200–202, 204, 205] the density-matrix renormalization-group method [32–35] was the numerical method of choice. However, despite the vast amount of theoretical work on flux ladders various questions remain open.

### Open questions

In view of current efforts aiming at the realization of flux ladders in the interacting regime, the investigation of the phase diagrams for the exact parameters that could be accessed in future experiments is particularly relevant. This includes, for instance, to account for the impact of nearest-neighbor rungwise interparticle interactions, which are typically present in synthetic dimension implementations [186]. Moreover, most of the theoretical studies so far have concentrated on ground states which are formally attained at zero temperature, whereas experiments naturally operate at nonzero energy densities. The question if and up to which temperature characteristic features of the ground-state phases persist is relevant in experimental realizations [183, 192, 204, 206]. For this reason, a purification approach for the calculation of finite-temperature states in strongly interacting bosonic flux ladders has been implemented in the framework of this thesis [3]. It is exploited for the study of the vortex-to-Meissner crossover at finite temperatures, which corresponds to the most prominent ground-state phase transition in the two-leg flux-ladder model.

Moreover, the development of optimal state-preparation protocols for the effective realization of the different ground-state phases of flux-ladder models, based, for instance, on the dynamics induced by quantum quenches or ramps, is highly desired [207]. In

general, this requires time-dependent simulations of the many-body systems. Similarly, theoretical proposals addressing how to probe the various ground-state phases of flux-ladder models are of great interest. Recent work in this direction has concentrated on spectroscopic [208, 209] or transport [174, 210–212] measurements. In this thesis, we study the ground-state phases of a synthetic flux-ladder model which is envisioned to be realized by the ultracold quantum gases group at ICFO [2]. Considering realistic model parameters and experimentally feasible initial states, we show that the transient dynamics induced by suitable quantum quenches can be used to probe the equilibrium properties of the relevant ground-state phases.

Flux ladders are the most simple lattice models giving rise to the Hall effect. Nonetheless, the theoretical description and computation of the many-body Hall response in various ground-state phases of these systems remains a tricky problem and an active line of research [213–220]. Observables which are at the core of the definition of the Hall response of flux ladders are the longitudinal particle current and the transverse density polarization. Importantly, they have already been measured in weakly interacting quantum gases [136, 139, 140, 149, 151], putting the quantum simulation of the Hall response in the strongly correlated regime into prospect. There, numerical calculations remain challenging. From the theoretical perspective, an appealing approach to introduce a static longitudinal current and study the induced Hall response is to consider ring-shaped flux ladders with twisted boundary conditions [213, 214]. However, despite their theoretical appeal, ring ladders are hardly accessible in typical experiments [173], and matrix-product-state based ground-state calculations are rendered inherently difficult by the presence of periodic boundary conditions. Building up on and extending previous work of Greschner et al. [219], in this thesis, we propose a complementary method for the computation of Hall response [1]. It is based on the simulation of ramp protocols in ladders with open boundary conditions, which are feasible in current quantum gas experiments [136, 139, 140, 149, 151]. We report on characteristic zero crossings and a remarkable robustness of the Hall response with respect to interparticle interaction strengths, particle fillings, and ladder geometries in different quantum phases.

## 1.4 Outline of this thesis

This thesis is organized as follows.

Chapter 2 introduces the flux-ladder model. In particular, we review important features of the noninteracting model and discuss common observables of interest. More-

over, we give an overview of the ground-state phases that are especially relevant in the framework of this thesis.

Chapter 3 is devoted to the numerical methods employed in this thesis. There, we discuss key aspects of matrix-product states [35] and review the most successful workhorse for the numerical calculation of ground states in one-dimensional quantum lattice systems: the density-matrix renormalization-group method [32, 35]. Moreover, we present a purification approach for the calculation of finite-temperature states and touch on state-of-the-art time-evolution methods [36]. Readers primarily interested in the physics might skip this chapter.

Chapter 4 deals with flux-ladder model parameters that are envisioned to be realized in a synthetic dimension implementation by the quantum gases group at ICFO. First, we map out the ground-state phase diagram of the synthetic flux-ladder model using extensive density-matrix renormalization-group simulations. Second, we discuss how the equilibrium properties of the most prominent Meissner phase and biased-ladder phase can be probed in the transient dynamics induced by suitably chosen quantum quenches.

Chapter 5 presents work on the effect of finite temperatures in flux ladders. There, our main results, which have been obtained by means of the matrix-product-state based purification approach, concern the vortex-liquid-to-Meissner crossover of strongly repulsive bosons.

Chapter 6 is devoted to the Hall response in flux ladders. Employing ground-state calculations in ring ladders, time-dependent quench simulations, and a semiclassical approach, we present consistent results for the Hall voltage in different many-body ground-state phases. Moreover, we argue that the Hall voltage exhibits characteristic zero crossings and a generic robustness in Meissner and vortex-lattice phases.

Chapter 7 presents a brief summary of our work and touches on possible follow-up studies which are directly related to the contents of this thesis.

## Flux-ladder model

The purpose of this chapter is to introduce the flux-ladder model which will be studied throughout this thesis. Concretely, in Sec. 2.1, we define the model Hamiltonian and review key aspects of the system in the absence of interparticle interactions. There, we also introduce the key observables of interest. In Sec. 2.2, we provide an overview of the ground-state phases of the interacting model that are especially relevant in the framework of this thesis.

### 2.1 Model Hamiltonian

The Hamiltonian of the paradigmatic two-leg flux-ladder model reads

$$\begin{aligned}
 H = & -J \sum_{r=0}^{L-2} \sum_{l=0}^1 \left( a_{r,l}^\dagger a_{r+1,l} + \text{H.c.} \right) - J_\perp \sum_{r=0}^{L-1} e^{-ir\phi} \left( a_{r,0}^\dagger a_{r,1} + \text{H.c.} \right) \\
 & + \sum_{l=0}^1 \frac{U_l}{2} \sum_{r=0}^{L-1} n_{r,l} (n_{r,l} - 1) + V \sum_{r=0}^{L-1} n_{r,0} n_{r,1}. \quad (2.1)
 \end{aligned}$$

Here, the parameters  $J$  and  $J_\perp$  correspond to nearest-neighbor hopping along the legs, labeled by  $l = 0$  and  $1$ , and the rungs, labeled by  $r = 0, 1, \dots, L-1$ , of the ladder. The site-local operator  $a_{r,l}^{(\dagger)}$  annihilates (creates) a particle on site  $(r, l)$ . Further,  $n_{r,l} = a_{r,l}^\dagger a_{r,l}$  accounts for the occupation of the individual lattice sites. It is worth noting that in Eq. (2.1) we consider the so-called rung gauge [186], in which the Peierls phase factors are aligned along the rungs of the ladder. They are chosen in such a way that whenever a particle encircles a single plaquette of the ladder, its wave function gains an overall phase factor  $e^{\pm i\phi}$ , with the sign depending on the direction of the circulation. The

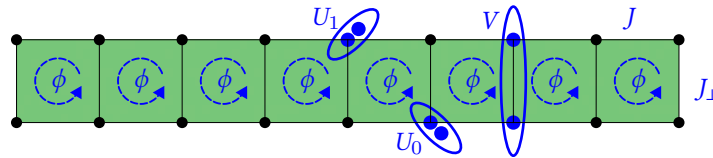


**Figure 2.1: Sketch of the two-leg flux-ladder model.** The Hamiltonian parameters  $J$ ,  $J_\perp$ ,  $V$ ,  $U_0$ ,  $U_1$ , and  $\phi$  are introduced in the context of Eq. (2.1). In experimental realizations exploiting a synthetic dimension, the legs of the ladder correspond to different internal atomic states. This is discussed in more detail in Ch. 4.

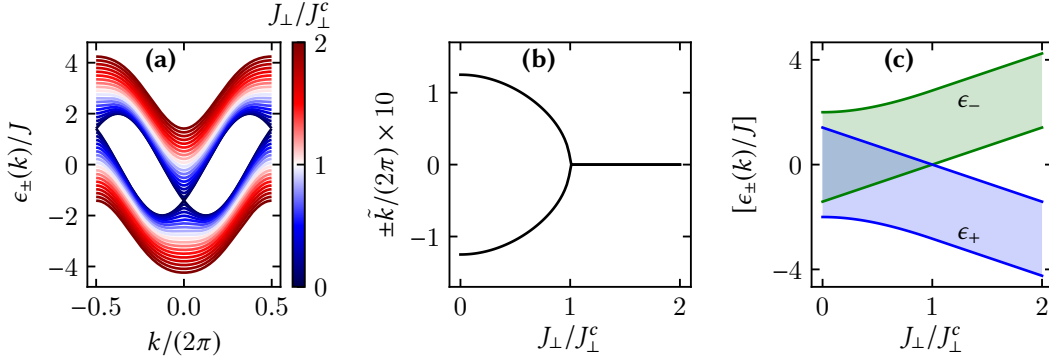


**Figure 2.2: Band structure of the noninteracting two-leg flux-ladder model.** Considering a magnetic flux per plaquette  $\phi = \pi/2$  and  $U_0 = U_1 = V = 0$ . (a) The two bands  $\epsilon_{\pm}$  of the model are shown for different values of the interleg hopping strength  $J_{\perp}/J_{\perp}^c$ , as indicated by the colorbar. In the Meissner phase ( $J_{\perp} > J_{\perp}^c$ ), the lower band exhibits a single minimum at zero momentum. In the vortex phase ( $J_{\perp} < J_{\perp}^c$ ), the lower band exhibits two degenerate minima at finite momenta. The lower band and the upper band are separated by a finite energy gap for nonvanishing values of  $J_{\perp}$ . Note that the critical value  $J_{\perp}^c$  is given in Eq. (2.8). (b) The characteristic momenta  $\pm\tilde{k}$  of the ground states clearly indicate the vortex-to-Meissner transition. (c) The shaded regions represent the ranges  $[\epsilon_{\pm}(k)] = [\min_k \epsilon_{\pm}(k), \max_k \epsilon_{\pm}(k)]$  of the lower and the upper band. A comprehensive analysis of the noninteracting problem can be found in Refs. [64, 196].

parameters  $U_0$  and  $U_1$  determine the site-local interparticle interaction strength on the  $l = 0$  leg and on the  $l = 1$  leg, respectively. Rungwise interparticle interactions are parametrized by  $V$ . We emphasize that in Eq. (2.1) and throughout this thesis, we set  $\hbar = 1$  and  $k_B = 1$ . Typically, we employ the leg-hopping parameter  $J$  as an energetic unit of reference. The two-leg flux-ladder Hamiltonian is sketched in Fig. 2.1.

### 2.1.1 Noninteracting model with periodic boundary conditions

Let us recap some of the key features of the flux-ladder model in the absence of interparticle interactions ( $U_0 = 0$ ,  $U_1 = 0$ ,  $V = 0$ ), noting that a comprehensive overview of the noninteracting system can be found, for instance, in Refs. [64, 196]. In the following, we consider periodic boundary conditions along the legs, which allow for an analytic study of the model.

In order to diagonalize the noninteracting model Hamiltonian, it is first rewritten in terms of leg-gauge operators denoted by an overhead tilde and defined by

$$\tilde{a}_{r,0} = e^{ir\frac{\phi}{2}} a_{r,0}, \quad \tilde{a}_{r,1} = e^{-ir\frac{\phi}{2}} a_{r,1}, \quad (2.2)$$

which moves the complex hopping terms from the rungs to the legs of the ladder. Second, leg-gauge momentum operators  $\tilde{a}_{k_m,l}^{(\dagger)}$  are introduced by means of Fourier transforming site-local operators  $\tilde{a}_{r,l}^{(\dagger)}$  along the legs of the ladder,

$$\tilde{a}_{k_m,l} = \frac{1}{\sqrt{L}} \sum_{r=0}^{L-1} e^{ik_m r} \tilde{a}_{r,l}, \quad (2.3)$$

with  $m = 0, 1, \dots, L-1$  and quasimomenta  $k_m = 2\pi m/L$ . In terms of these leg-gauge momentum operators, the noninteracting Hamiltonian with periodic boundary conditions takes the form

$$H = \sum_{m=0}^{L-1} \begin{pmatrix} \tilde{a}_{k_m,0}^\dagger & \tilde{a}_{k_m,1}^\dagger \end{pmatrix} \begin{pmatrix} -2J \cos\left(\frac{\phi}{2} + k\right) & -J_\perp \\ -J_\perp & -2J \cos\left(\frac{\phi}{2} - k\right) \end{pmatrix} \begin{pmatrix} \tilde{a}_{k_m,0} \\ \tilde{a}_{k_m,1} \end{pmatrix}. \quad (2.4)$$

Finally, the operators  $d_{k_m,\pm}^{(\dagger)}$  diagonalizing the noninteracting Hamiltonian are given by

$$d_{k_m,\pm} = \frac{(A_{k_m} \mp B_{k_m}) \tilde{b}_{0,k_m} \pm \xi \tilde{b}_{1,k_m}}{\sqrt{(A_{k_m} \mp B_{k_m})^2 + \xi^2}}, \quad (2.5)$$

with  $\xi = J_\perp/(2J)$ ,  $B_k = \sin(k) \sin(\phi/2)$ , and  $A_k = \sqrt{\xi^2 + B_k^2}$ . Thus, the Hamiltonian takes the form

$$H = \sum_{m=0}^{L-1} \sum_{\sigma=+,-} \epsilon_\sigma(k_m) d_{k_m,\sigma}^\dagger d_{k_m,\sigma}, \quad (2.6)$$

where the eigenvalues corresponding to the lower and upper band,  $\epsilon_+(k_m)$  and  $\epsilon_-(k_m)$ , are given by  $\epsilon_\pm(k_m) = -2J (\cos(k) \cos(\phi/2) \pm A_{k_m})$ .

For a nonvanishing interleg coupling strength,  $J_\perp \neq 0$ , the two bands are separated by a finite energy gap. Depending on the magnetic flux  $\phi$  and the interleg hopping strength  $J_\perp$ , the lower band has either a single global minimum at momentum  $k = 0$  or two degenerate minima at  $k = \pm\tilde{k}$  with

$$\tilde{k} = \arccos\left(\frac{\sqrt{\xi^2 + \sin(\phi/2)^2}}{\tan(\phi/2)}\right). \quad (2.7)$$

For  $k = 0$  a bosonic or a single-particle system is referred to be in a Meissner phase, while for  $k = \pm\tilde{k}$  it is in a vortex phase [136]. These names reflect the characteristic current patterns observed in the ground-state phases. On the one hand, the Meissner

phase exhibits strong and uniform particle currents encircling the ladder along its legs in opposite directions, while there are vanishing rung currents. On the other hand, there are current vortices with finite rung currents in the vortex phase for open boundary conditions. As a function of the magnetic flux  $\phi$ , the critical value of the interleg hopping strength separating the two phases is given by

$$J_{\perp}^c = 2J \sin(\phi/2) \tan(\phi/2). \quad (2.8)$$

The two-band structure of the noninteracting ladder model is shown for different values of  $J_{\perp}$  in Fig. 2.2(a). Figure 2.2(b) shows the characteristic momenta  $\pm\tilde{k}$  of the ground states as a function of  $J_{\perp}$ , which clearly indicate the vortex-to-Meissner transition.

In anticipation of the discussion of noninteracting fermions at finite temperatures in Ch. 5, Fig. 2.2(c) shows the range  $[\epsilon_{\pm}(k)] = [\min_k \epsilon_{\pm}(k), \max_k \epsilon_{\pm}(k)]$  of the lower band and of the upper band. From this, a transition-point for the fermionic system can be determined from

$$\min_k \epsilon_{-}(k) < \max_k \epsilon_{+}(k) \quad (\text{vortex phase}), \quad (2.9)$$

$$\min_k \epsilon_{-}(k) > \max_k \epsilon_{+}(k) \quad (\text{Meissner phase}). \quad (2.10)$$

Note that we use the same terminology — Meissner phase and vortex phase — as for bosons because the local current patterns show the same characteristics.

### 2.1.2 Observables of interest

For the flux-ladder model introduced above, common observables of interest include momentum distribution functions, the leg-population imbalance, and locally resolved particle currents. They are introduced in the following.

#### Momentum-distribution functions

Momentum-distribution functions exhibit characteristics specific to certain ground-state phases of the flux-ladder Hamiltonian (2.1) [64, 186]. Moreover, in ultracold quantum gases they can be obtained from time-of-flight measurements [16]. For the rung gauge employed in Eq. (2.1), leg-resolved momentum-distribution functions  $\bar{n}_l(k_m)$  are given by means of momentum operators  $\bar{a}_{k_m,l}$  denoted by an overhead bar and obtained from Fourier transforming site-local rung-gauge operators  $a_{r,l}$  along the legs of the system,

$$\bar{n}_l(k_m) = \left\langle \bar{a}_{k_m,l}^{\dagger} \bar{a}_{k_m,l} \right\rangle, \quad \bar{a}_{k_m,l} = \frac{1}{\sqrt{L}} \sum_{r=0}^{L-1} e^{ik_m r} a_{r,l}. \quad (2.11)$$

The quasimomenta are given by  $k_m = 2\pi m/L$  with  $m = 0, 1, \dots, L-1$ . We stress that throughout this thesis, angled brackets denote expectation values. The corresponding leg-integrated momentum-distribution function is given by

$$\bar{n}(k_m) = \bar{n}_0(k_m) + \bar{n}_1(k_m). \quad (2.12)$$

Analogously, leg-resolved leg-gauge momentum-distribution functions are defined by means of leg-gauge operators, introduced in Eq. (2.3) and denoted by an overhead tilde,

$$\tilde{n}_l(k_m) = \left\langle \tilde{a}_{k_m,l}^\dagger \tilde{a}_{k_m,l} \right\rangle. \quad (2.13)$$

The leg-integrated leg-gauge momentum-distribution function is given by  $\tilde{n}(k_m) = \tilde{n}_0(k_m) + \tilde{n}_1(k_m)$ . Note that leg-resolved leg-gauge and leg-resolved rung-gauge momentum-distribution functions are related as follows:

$$\tilde{n}_0(k) = \bar{n}_0\left(k + \frac{\phi}{2}\right), \quad \tilde{n}_1(k) = \bar{n}_1\left(k - \frac{\phi}{2}\right). \quad (2.14)$$

We compare all four types of momentum-distribution functions — leg gauge versus rung gauge and leg-integrated versus leg-resolved — in Fig. 2.3. In general, the number of possible maxima is doubled by going from the leg gauge to the rung gauge. Note that in the experiment performed by Atala et al. [136] the rung gauge was realized, which leads to the momentum-distribution function  $\bar{n}(k)$ .

### Local particle currents and chiral current

Various ground-state phases found in the interacting flux-ladder model have been successfully distinguished by means of their characteristic particle-current patterns [186]. Local particle currents  $j_r^\perp$  and  $j_{r,l}^\parallel$  from site  $(r, 0)$  to site  $(r, 1)$  and from site  $(r, l)$  to site  $(r+1, l)$ , respectively, are derived from the continuity equation for the occupation of the local lattice sites,

$$\begin{aligned} -\frac{d}{dt} \langle n_{r,l} \rangle &= i \left\langle \left[ a_{r,l}^\dagger a_{r,l}, H \right] \right\rangle \\ &= j_{r,l}^\parallel - j_{r-1,l}^\parallel \pm j_r^\perp, \end{aligned} \quad (2.15)$$

with  $+$  and  $-$  for  $l = 0$  and  $l = 1$ , respectively. Explicitly, the corresponding operators are defined by means of

$$j_{r,l}^\parallel = \left\langle i J a_{r,l}^\dagger a_{r+1,l} + \text{H.c.} \right\rangle, \quad j_r^\perp = \left\langle i J_\perp e^{-ir\phi} a_{r,0}^\dagger a_{r,1} + \text{H.c.} \right\rangle. \quad (2.16)$$

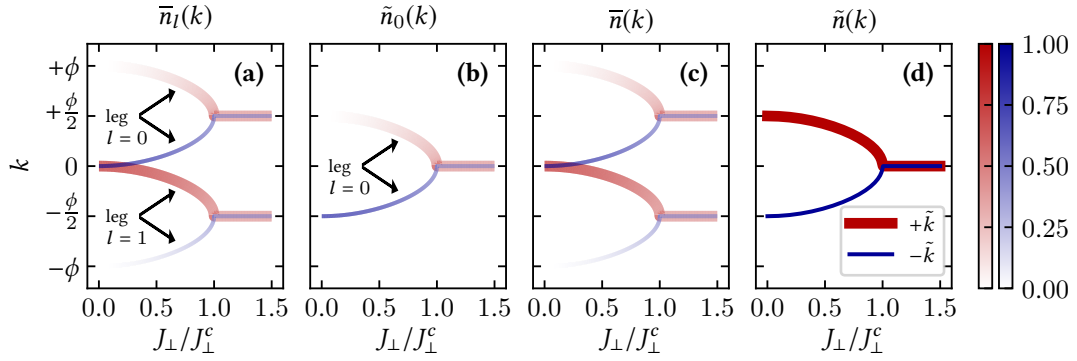


**Figure 2.3: Comparison of momentum-distribution functions in the single-particle ground states.** The figure shows the position of the maxima in various momentum-distribution functions that are (a), (b) leg-resolved ( $l = 0, 1$ ) or (c), (d) integrated over  $l$ . The values of momentum-distribution functions for each of the single-particle ground states are indicated by the colorbars. Note that red and blue correspond to the  $+\tilde{k}$  state and  $-\tilde{k}$  state, respectively, as described in the context of Eq. (2.7). Panels (a) and (c) depict the behavior in the rung gauge, while (b) and (d) are for the leg gauge.

Here, it is worth noting that the chiral current

$$j_c = \frac{1}{L-1} \sum_{r=0}^{L-2} (j_{r,1}^{\parallel} - j_{r,0}^{\parallel}), \quad (2.17)$$

which represents the global particle transport along the legs of the system in opposite directions, is an important observable. It is indicative of the most prominent vortex-to-Meissner transition in the flux-ladder model [136, 179, 184].

### Leg-population imbalance

The total particle number, which is conserved by the flux-ladder Hamiltonian (2.1), is denoted by

$$N = \sum_{r=0}^{L-1} \sum_{l=0}^1 \langle n_{r,l} \rangle. \quad (2.18)$$

We define the particle filling per lattice site as

$$\nu = N/(2L). \quad (2.19)$$

Furthermore, we employ the abbreviation

$$N_l = \sum_{r=0}^{L-1} \langle n_{r,l} \rangle \quad (2.20)$$

for the total particle number in the  $l = 0$  leg or  $l = 1$  leg. The leg-population imbalance is defined as

$$\Delta_l = \frac{|N_0 - N_1|}{N_0 + N_1}. \quad (2.21)$$

In the course of this thesis, we exemplify the observables introduced above in various ground-state phases of the interacting flux-ladder model. In Sec. 4.1 we comment on how they can be accessed in an experimental setup exploiting a synthetic dimension.

## 2.2 Ground-state phases in the presence of interactions

In the presence of interparticle interactions, bosonic flux ladders host a panoply of emergent quantum phases [186]. In the following, without claiming completeness, we give an account of important ground-state phases of the two-leg model defined in Eq. (2.1). An overview of the different ground-state phases can be found in Fig. 2.4.

In 2001, Orignac and Giamarchi showed in a seminal study based on a bosonization approach that the minimal two-leg flux-ladder model exhibits Meissner and vortex-lattice phases, which are reminiscent of a type-II superconductor [179]. The Meissner phase can be seen in Fig. 2.4(a). It exhibits a homogeneous particle-density profile and uniform particle currents encircling the ladder along its legs. The expected absolute value of the rung current vanishes in the thermodynamic limit,  $\lim_{L \rightarrow \infty} \langle |j_r^\perp| \rangle_r = 0$ , where  $\langle \bullet \rangle_r$  denotes the average over all rungs. In the Meissner phase the ground-state unit cell comprises a single plaquette of the ladder,  $q = 1$ . It is worth noting that the Meissner phase can exist on top of Mott insulators [182, 197] as well as on top of superfluids [184]. Typically, the Mott-insulating Meissner phase emerges at a commensurate particle filling per rung. The central charge, counting the number of gapless modes, is zero in the Mott-insulating Meissner phase,  $c = 0$  [186]. In the superfluid Meissner phase, the charge gap vanishes and the central charge is  $c = 1$ . Note that the table in Fig. 2.4(f) lists the size of the effective ground-state unit cell  $q$ , the leg-population imbalance  $\Delta_l$ , the average rung current  $\langle |j_r^\perp| \rangle_r$ , and the central charge  $c$  for various ground-state phases.

Vortex-lattice phases are regular crystals of localized vortices [180, 181, 183]. More specifically, vortex-lattice $_{p/q}$  phases exhibit  $p$  vortices per  $q$ -plaquette unit cell. In the limit of vanishing rung hopping,  $J_\perp/J \rightarrow 0$ , and for a homogeneous particle density, a complete devil's staircase of vortex-lattice $_{p/q}$  phases at each commensurate vortex density  $p/q$  is predicted [179]. Finite values of  $J_\perp/J$  and increasing interparticle interaction strengths gradually destabilize the vortex-lattice $_{p/q}$  phases with largest  $q$ . Vortex-lattice $_{1/q}$  phases, which are shown for  $q = 2$  and  $q = 3$  in Fig. 2.4(b) and in Fig. 2.4(c),

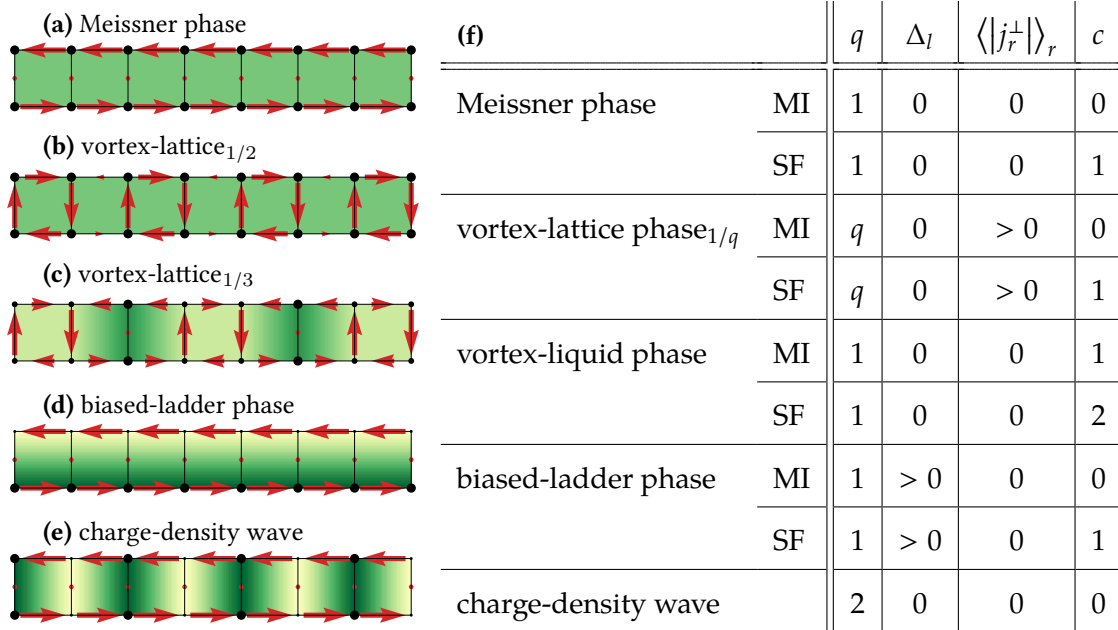


**Figure 2.4: Ground-state phases in the interacting bosonic two-leg flux-ladder model.** (a)-(e) Various ground-state phases of the interacting bosonic flux-ladder Hamiltonian (2.1). The size of the dots and the background shading indicate the local particle density. The red arrows show the local current patterns. (f) Overview of the ground-state phases considered in this thesis, listing characteristic values of the effective size of the ground-state unit cell  $q$  (in plaquettes), the leg-population imbalance  $\Delta_l$ , the average absolute value of the rung current  $\langle |j_r^\pm| \rangle_r$  in the thermodynamic limit  $L \rightarrow \infty$ , and the central charge  $c$ . Note that MI refers to a Mott-insulating phase and SF denotes a superfluid phase. Different ground-states in the two-leg flux-ladder model are comprehensively discussed in Ref. [186], which also provides an extended tabular overview.

respectively, exhibit finite rung currents in the thermodynamic limit,  $\lim_{L \rightarrow \infty} \langle |j_r^\pm| \rangle_r > 0$ . For  $q > 2$  they also feature particle density modulations following the underlying current structure. Interestingly, the breaking of the translational symmetry of the underlying lattice model in the vortex-lattice phases can lead to a reversal of the chiral current [183]. Like Meissner phases, vortex-lattice phases can exist on top of superfluids and Mott insulators [186]. However, in general, they are elusive in the strongly interacting regime, requiring weak but finite interaction strengths. In Ch. 6, we study the Hall response in different vortex-lattice phases, which can be well described by means of a semiclassical ansatz [175–178]. In contrast to vortex-lattice phases, vortex-liquid phases do not exhibit pinned vortices and rung-current correlations. They show irregular leg-current patterns and can exist for any value of the interparticle interaction strength [184].

Moreover, the flux-ladder Hamiltonian (2.1) hosts a biased-ladder phase, which is shown in Fig. 2.4(d). It was first discussed by Wei and Mueller in 2014 [185]. The main characteristic of the biased-ladder phase is a finite leg-population imbalance, which is usually stabilized by the presence of rungwise interactions. Note that the biased-ladder phase exhibits Meissner-like currents along the legs and vanishing rung currents. In Ch. 4, we show that the biased-ladder phase can exist on top of superfluids and Mott insulators. Furthermore, we demonstrate how the finite leg-population imbalance can be probed in quench experiments.

The charge-density wave shown in Fig. 2.4(e) can be observed in the strongly-interacting regime for a magnetic flux  $\phi \lesssim \pi$  and a particle filling  $\nu = 1/4$  [184, 197]. Its key features are particle-density modulations along the legs, while it exhibits homogeneous Meissner-like currents. The charge-density wave shown in Fig. 2.4(e) exhibits a two-plaquette ground-state unit cell. Note that for different values of the particle filling  $\nu$  one might encounter further gapped charge-density waves with enlarged unit cells, such as a three-plaquette variant at  $\nu = 1/3$  [186].

Finally, we conclude this overview with two remarks. First, there are further interesting ground-state phases to be expected in extensions of the two-leg flux-ladder model, such as, for instance, the staggered-current phase in strongly interacting three-leg ladders [221] or relatives of Meissner phases and vortex-lattice phases in Haldane ladders [222]. Second, the existence of precursors of fractional quantum Hall states in bosonic flux ladders has attracted great interest [187–193, 223]. In general, these states require a fine-tuned ratio between the magnetic flux and the particle filling. Considering a magnetic flux  $\phi = \pi/4$  and twisted boundary conditions in the short direction of a two-leg ladder, it is shown by Grusdt and Höning that a charge-density-wave ground state at particle filling  $\nu = 1/8$  can be related to the  $1/2$ -Laughlin state [188]. In the two-leg flux-ladder model discussed in Sec. 2.1, fractional quantum Hall-like states leave clear signatures in the entanglement entropy and in the chiral current [191, 192]. For instance, it is shown by Strinati et al. [192] that a discontinuity in the chiral current indicates a  $1/2$ -Laughlin-like state for finite rungwise interactions  $V$ , small rung hoppings  $J_{\perp}/J \ll 1$ , and a site-local hard-core constraint, meaning that there can be at most one boson per lattice site ( $U_0/J = U_1/J \rightarrow \infty$ ). Interestingly, we could reproduce these results and found that a characteristic kink in the chiral current also survives beyond the site-local hard-core constraint, such as for  $U_0 = U_1 = V = 15J$ . This might be interesting for quantum gas experiments exploiting a synthetic dimension, as the one discussed in Ch. 4. However, precursors of fractional quantum Hall states are beyond the scope of this thesis and they are left for future studies.



## Numerical methods

This chapter introduces the numerical matrix-product-state based methods employed in this thesis. The reader primarily interested in the physics might skip this part and jump directly to Ch. 4, where we present our results concerning the synthetic dimension implementation of a bosonic flux ladder.

This chapter is organized as follows. In Sec. 3.1, we recapitulate the concept of entanglement in bipartite quantum systems, Schmidt decompositions, and singular value decompositions, which play a crucial role in practical matrix-product-state approaches. In Sec. 3.2, we introduce matrix-product states following a constructive approach. The purpose of Sec. 3.3 is to introduce the most successful workhorse for the numerical calculation of ground states in one-dimensional quantum lattice systems: the density-matrix renormalization-group method. In Sec. 3.4, we introduce a purification approach for the calculation of finite-temperature states in flux ladders, which has been implemented in the framework of this thesis. Finally, state-of-the-art time-evolution methods for matrix-product states are discussed in Sec. 3.5.

Here, we follow the seminal review article on the density-matrix renormalization-group method and matrix-product states by U. Schollwöck [35].

### 3.1 Quantum states and entanglement

Let us start off by recapitulating the concept of quantum entanglement, which also allows us to fix some of the notation employed later on. For this, we consider two-state systems, which are commonly referred to as qubits.

#### Entangled qubits

In general, the state of a one-qubit system, referred to as  $A$ , reads  $|\psi\rangle_A = \alpha |0\rangle_A + \beta |1\rangle_A$ , with complex numbers  $\alpha$  and  $\beta$  satisfying  $|\alpha|^2 + |\beta|^2 = 1$  and basis states  $|0\rangle_A$  and  $|1\rangle_A$ . The simplest model which might yet host entangled quantum states is a composite two-qubit system  $AB$ , comprised of two qubits  $A$  and  $B$ . For this system, a typical example of an entangled state is the Bell state

$$|+\rangle_{AB} = \frac{1}{\sqrt{2}} (|0\rangle_A |0\rangle_B + |1\rangle_A |1\rangle_B) . \quad (3.1)$$

The Bell state  $|+\rangle_{AB}$  cannot be rewritten as a simple product state of the form  $|\phi\rangle_A |\chi\rangle_B$ .

Moreover, the reduced state of system A, which is obtained by tracing out system B, is a mixed state,

$$\rho_A = \text{tr}_B (|+\rangle_{AB} \langle +|_{AB}) = \frac{1}{2} (|0\rangle_A \langle 0|_A + |1\rangle_A \langle 1|_A) . \quad (3.2)$$

Indeed,  $\rho_A$  is maximally mixed, meaning that the von Neumann or entanglement entropy, which is defined as

$$S(\rho_A) = -\text{tr}(\rho_A \log_2 \rho_A) , \quad (3.3)$$

takes on the maximum possible value for a two-state system,  $S(\rho_A) = 1$ . Note that we employ the binary logarithm ( $\log_2$ ) for the definition of the entanglement entropy. In the following, we consider more general systems AB, which are composed of subsystems A and B that are not necessarily two-state systems but might exhibit more degrees of freedom and thus larger Hilbert spaces.

### Schmidt decompositions and singular value decompositions

The Schmidt decomposition is a useful tool for the systematic analysis of quantum states of bipartite systems because it allows for a very convenient representation of such states [88]. Basically, it ensures that any pure state  $|\psi\rangle_{AB}$  of a bipartite quantum system AB can be decomposed by means of orthonormal states  $|a_k\rangle_A$  and  $|b_k\rangle_B$  for system A and system B, respectively,

$$|\psi\rangle_{AB} = \sum_{k=1}^{\chi} s_k |a_k\rangle_A |b_k\rangle_B , \quad (3.4)$$

where the Schmidt coefficients  $s_k$  are nonnegative real numbers. For a normalized state  $|\psi\rangle_{AB}$  the Schmidt coefficients satisfy  $\sum_{k=1}^{\chi} s_k^2 = 1$ . Most importantly, the number of required basis states  $\chi$  in Eq. (3.4) provides information about the nature of  $\psi_{AB}$ . While  $\chi = 1$  corresponds to a simple product state,  $\chi \geq 2$  is indicative of an entangled quantum state. The maximum possible value of  $\chi$  is given by the Hilbert space dimension of the smaller subsystem,  $\chi \leq \min(d_A, d_B)$ . Moreover, from the Schmidt-decomposed representation of  $|\psi\rangle_{AB}$  given in Eq. (3.4), the reduced states for system A and system B can be immediately read off. Employing the orthonormality of the states  $|b_k\rangle_B$ , meaning that they can be extended in order to form a complete basis for B, we find

$$\rho_A = \sum_{k=1}^{\chi} s_k^2 |a_k\rangle_A \langle a_k|_A . \quad (3.5)$$

Analogously, the reduced state of system B is given by  $\rho_B = \sum_{k=1}^{\chi} s_k^2 |b_k\rangle_B \langle b_k|_B$ . Note that the von Neumann entropy of the reduced states is  $S(\rho_A) = S(\rho_B) = -\sum_{k=1}^{\chi} s_k^2 \log_2 s_k^2$ .

The Schmidt decomposition (3.4) is closely related to a singular value decomposition of a complex rectangular matrix, which plays a crucial role in practical matrix-product-state algorithms. Thus, it might be instructive to elaborate on this relation. We recap that by means of a singular value decomposition, any complex  $(d_A \times d_B)$  matrix  $\psi$  can be decomposed into a matrix product involving three matrices  $U, D$ , and  $V^\dagger$ ,

$$\psi = UDV^\dagger, \quad (3.6)$$

with the following properties,

$$U^\dagger U = I_{\chi, \chi}, \quad D = \text{diag}(s_1, \dots, s_\chi), \quad V^\dagger V = I_{\chi, \chi}. \quad (3.7)$$

Note that  $I_{\chi, \chi}$  is the  $(\chi \times \chi)$  identity matrix and  $\chi = \min(d_A, d_B)$ . Further,  $U$  is a complex  $(d_A \times \chi)$  matrix with orthonormal columns, while  $D$  is a diagonal matrix with nonnegative entries  $s_k \geq 0$ , which are referred to as singular values. Similarly,  $V^\dagger$  is a complex  $(\chi \times d_B)$  matrix with orthonormal rows. Indeed, Eq. (3.4) can be understood as a singular value decomposition (3.6). For this,  $|\psi\rangle_{AB}$  is rewritten by means of a coefficient matrix  $\psi$ ,

$$|\psi\rangle_{AB} = \sum_{i=1}^{d_A} \sum_{j=1}^{d_B} \psi_{ij} |e_i\rangle_A |e_j\rangle_B, \quad (3.8)$$

considering basis states  $|e_i\rangle_A$  and  $|e_j\rangle_B$  for system A and B, respectively. The state coefficients  $\psi_{ij}$  are interpreted as the entries of the  $(d_A \times d_B)$  matrix  $\psi$ . Subjecting this matrix to a singular value decomposition  $\psi = UDV^\dagger$  leads to (using the notation from Eq. (3.6))

$$\begin{aligned} |\psi\rangle_{AB} &= \sum_{k=1}^{\chi} \sum_{i=1}^{d_A} \sum_{j=1}^{d_B} U_{i,k} D_{k,k} V_{k,j}^\dagger |e_i\rangle_A |e_j\rangle_B \\ &= \sum_{k=1}^{\chi} s_k \left( \sum_{i=1}^{d_A} U_{i,k} |e_i\rangle_A \right) \left( \sum_{j=1}^{d_B} V_{k,j}^\dagger |e_j\rangle_B \right). \end{aligned} \quad (3.9)$$

The Schmidt decomposition (3.4) is recovered from the singular value decomposition (3.9) by identifying the singular values with the Schmidt coefficients and

$$\sum_{i=1}^{d_A} U_{i,k} |e_i\rangle_A \rightarrow |a_k\rangle_A, \quad \sum_{j=1}^{d_B} V_{k,j}^\dagger |e_j\rangle_B \rightarrow |b_k\rangle_B. \quad (3.10)$$

Note that in Eq. (3.9) the sum running over  $k$  can be restricted to nonvanishing singular values, which leads to Eq. (3.4).

Having shown how the Schmidt decomposition (3.4) can be computed by means of a singular value decomposition (3.9), we emphasize that the Schmidt decomposition also allows for the systematic approximation of quantum states  $|\psi\rangle_{AB}$ . As  $\chi \leq \min(d_A, d_B)$  might become huge in practice, in Eq. (3.4) one might want to keep only basis vectors corresponding to a fixed number  $\chi' < \chi$  of the largest singular values  $s_k$ , while trying to maintain a maximum amount of entanglement entropy. Thus,  $|\psi\rangle_{AB}$  is approximated by means of

$$\begin{aligned} |\psi\rangle_{AB} &= \sum_{k=1}^{\chi} s_k |a_k\rangle_A |b_k\rangle_B \\ &\approx \sum_{k=1}^{\chi'} \frac{s_k}{\sqrt{\sum_{k'=1}^{\chi'} s_{k'}^2}} |a_k\rangle_A |b_k\rangle_B. \end{aligned} \quad (3.11)$$

Here, the singular values are assumed to be in descending order,  $s_1 \geq s_2 \geq \dots \geq s_{\chi}$ , and the normalization of the approximated state is ensured by rescaling the kept singular values. It turns out that this approximation is at the heart of practical matrix-product-state approaches.

## 3.2 Matrix-product states

Matrix-product states are convenient representations of quantum lattice states. Specifically, they are comprised of rank-three tensors representing physical lattice sites. These tensors are aligned side by side in order to form a simple yet very useful tensor network. Here, we remind the reader that the brief introduction of the matrix-product-state framework presented in this thesis follows the seminal review article [35], adopting some of the notation employed therein.

Let us start off with a constructive approach and demonstrate how a generic quantum lattice state can be expressed as a matrix-product state.

### Rewriting a quantum lattice state as a matrix-product state

Quantum lattice models are comprised of physical sites with quantum degrees of freedom. Typically, these models are governed by a Hamiltonian made up of terms that can be directly related to the vertices and edges of the underlying lattice. Here, for simplicity, we consider all physical sites in the lattice to be of the same kind, with a

site-local basis given by  $(|e_1\rangle_i, |e_2\rangle_i, \dots, |e_d\rangle_i)$ . Note that the different sites are labeled by  $i$  and exhibit a  $d$ -dimensional state space. Thus, for a lattice with a total number of  $L$  sites, the generic quantum state that we aim to be represent as a matrix-product state is given by  $d^L$  coefficients  $c_{j_1, j_2, \dots, j_L}$ . Explicitly, it reads

$$|\psi\rangle = \sum_{j_1=1}^d \sum_{j_2=1}^d \cdots \sum_{j_L=1}^d c_{j_1, j_2, \dots, j_L} |j_1, j_2, \dots, j_L\rangle, \quad (3.12)$$

where we employ the shorthand notation  $|j_1, j_2, \dots, j_L\rangle = |e_{j_1}\rangle_1 |e_{j_2}\rangle_2 \cdots |e_{j_L}\rangle_L$ .

In order to represent  $|\psi\rangle$  as a matrix-product state, the coefficients  $c_{j_1, j_2, \dots, j_L}$  are shaped into a  $(d \times d^{L-1})$  matrix  $\psi_1$  such that the rows of  $\psi_1$  correspond to different  $j_1$  while the columns of  $\psi_1$  represent different values of the tuple  $(j_2, j_3, \dots, j_L)$ ,

$$c_{j_1, j_2, \dots, j_L} = \psi_{1; j_1, (j_2, \dots, j_L)}. \quad (3.13)$$

Next,  $\psi_1$  is subjected to a singular value decomposition, as discussed in the context of Eq. (3.6),  $\psi_1 = UDV^\dagger$ . Introducing  $A_{1; k_1}^{j_1} = U_{j_1, k_1}$  and reshaping

$$DV^\dagger = \text{diag}(s_1, \dots, s_d) V^\dagger \quad (3.14)$$

into a  $(d^2 \times d^{L-2})$  matrix  $\psi_2$ ,

$$\psi_{2; (k_1, j_2), (j_3, \dots, j_L)} = s_{k_1} V_{k_1, (j_2, \dots, j_L)}^\dagger, \quad (3.15)$$

the coefficients  $c_{j_1, j_2, \dots, j_L}$  can be expressed as

$$c_{j_1, j_2, \dots, j_L} = \sum_{k_1=1}^d A_{1; k_1}^{j_1} \psi_{2; (k_1, j_2), (j_3, \dots, j_L)}. \quad (3.16)$$

By employing a second singular value decomposition,  $\psi_2 = U \text{diag}(s_1, \dots, s_{d^2}) V^\dagger$ , further introducing  $A_{2; k_1, k_2}^{j_2} = U_{(k_1, j_2), k_2}$ , and reshaping  $\text{diag}(s_1, \dots, s_{d^2}) V^\dagger$  into  $\psi_3$ , Eq. (3.13) is rewritten as

$$c_{j_1, j_2, \dots, j_L} = \sum_{k_1=1}^d \sum_{k_2=1}^{d^2} A_{1; k_1}^{j_1} A_{2; k_1, k_2}^{j_2} \psi_{3; (k_2, j_3), (j_4, \dots, j_L)}. \quad (3.17)$$

From Eq. (3.16) and Eq. (3.17) it becomes apparent that by means of successive singular value decompositions and repeated matrix reshaping, the coefficients  $c_{j_1, j_2, \dots, j_L}$  can be brought into the following form

$$c_{j_1, j_2, \dots, j_L} = \sum_{k_1=1}^d \sum_{k_2=1}^{d^2} \cdots \sum_{k_{L-2}=1}^{d^2} \sum_{k_{L-1}=1}^d A_{1; k_1}^{j_1} A_{2; k_1, k_2}^{j_2} \cdots A_{L-1; k_{L-2}, k_{L-1}}^{j_{L-1}} A_{L; k_{L-1}}^{j_L}. \quad (3.18)$$

The right-hand side of the equation above represents a product of a total number of  $L$  matrices  $A_i^{j_i}$  of dimension  $(d^{\min(i,L-i+1)} \times d^{\min(i,L-i)})$ , where  $A_1^{j_1}$  and  $A_L^{j_L}$  can be understood as a row vector and a column vector, respectively. This immediately gives rise to the matrix-product-state representation of  $|\psi\rangle$ ,

$$|\psi\rangle = \sum_{j_1=1}^d \sum_{j_2=1}^d \cdots \sum_{j_{L-1}=1}^d \sum_{j_L=1}^d A_1^{j_1} A_2^{j_2} \cdots A_{L-1}^{j_{L-1}} A_L^{j_L} |j_1, j_2, \dots, j_L\rangle, \quad (3.19)$$

with a matrix  $A_i^{j_i}$  for each lattice site  $i$  and site-local basis state  $|e_{j_i}\rangle_i$ .

Actually, matrix-product states, as the one in Eq. (3.19), exhibit a gauge degree of freedom. Since matrix products  $A_i^{j_i} A_{i+1}^{j_{i+1}} = A_i^{j_i} M M^{-1} A_{i+1}^{j_{i+1}}$  remain unchanged by inserting the identity  $I = M M^{-1}$ , one is free to rewrite

$$A_i^{j_i} \rightarrow A_i^{j_i} M \quad A_{i+1}^{j_{i+1}} \rightarrow M^{-1} A_{i+1}^{j_{i+1}}, \quad (3.20)$$

using any invertible matrix  $M$  of suitable size. Also, by accounting for all site-local basis states  $|e_{j_i}\rangle_i$ , the  $A_i$  in Eq. (3.19) can be understood as rank-three tensors, which are the central building blocks of a matrix-product state. From this perspective, matrix-product states reveal themselves as simple yet very useful tensor networks: one-dimensional chains of rank-three tensors. Instructive graphical representations thereof can be found, for instance, in Ref. [35] and in Fig. 3.1. We note that while for one-dimensional lattice models it is quite natural to label the sites by going from one end of the system to the other, two-dimensional systems are typically approached by snaking through the underlying lattice.

Due to the exponential growth of the size of the matrices  $A_i^{j_i}$ , the formal construction presented above as well as the efficient handling of the corresponding matrix-product state is typically not feasible in practice. This already applies to moderate values of  $L$  and  $d$ . However, matrix-product states exhibit a key control parameter which renders numerical approaches feasible: the maximum bond dimension. The maximum bond dimension is related to the amount of entanglement entropy captured by a matrix-product state and, thus, it allows for the systematic approximation of quantum states. In the following, we recap the canonical representations of matrix-product states and discuss how the latter can be efficiently truncated.

### Canonical forms

It immediately follows from the construction by means of singular value decompositions that the  $A_i^{j_i}$  matrices in Eq. (3.19) satisfy

$$\sum_{j_i=1}^d A_i^{j_i \dagger} A_i^{j_i} = I, \quad (3.21)$$

where  $I$  denotes an identity matrix of suitable size. Matrix-product states that are constructed from  $A_i^{j_i}$  matrices satisfying Eq. (3.21) for  $i = 1, 2, \dots, L$  are referred to as being of left-canonical form.

By means of successive singular value decompositions, any matrix-product state

$$|\psi\rangle = \sum_{j_1=1}^d \sum_{j_2=1}^d \cdots \sum_{j_L=1}^d M_1^{j_1} M_2^{j_2} \cdots M_L^{j_L} |j_1, j_2, \dots, j_L\rangle \quad (3.22)$$

can be brought into left-canonical form. For this, by going through the tensors from left to right, that is,  $i = 1, 2, \dots, L$ , one decomposes

$$M_{i;k_{i-1},k_i}^{j_i} = \sum_{k'=1}^{\chi} U_{(j_i,k_{i-1}),k'} D_{k',k'} V_{k',k_i}^\dagger, \quad (3.23)$$

where  $U$ ,  $D$ , and  $V^\dagger$  are matrices with properties as discussed in the context of Eq. (3.6). Further, one replaces  $M_i$  by  $A_i$ , where  $A_{i;k_{i-1},k_i}^{j_i} = U_{(j_i,k_{i-1}),k'}$  satisfying Eq. (3.21), while  $M_{i+1}$  is replaced by means of

$$M_{i+1;k_i,k_{i+1}}^{j_{i+1}} \rightarrow \sum_{k'=1}^{\chi} D_{k_i,k_i} V_{k_i,k'}^\dagger M_{i+1;k',k_{i+1}}^{j_{i+1}}, \quad (3.24)$$

absorbing  $DV^\dagger$ .

Analogously, by going through the tensors from right to left, that is,  $i = L, L-1, \dots, 1$ , any matrix-product state can be brought into the following right-canonical form,

$$|\psi\rangle = \sum_{j_1=1}^d \sum_{j_2=1}^d \cdots \sum_{j_L=1}^d B_1^{j_1} B_2^{j_2} \cdots B_L^{j_L} |j_1, j_2, \dots, j_L\rangle, \quad (3.25)$$

with tensors  $B_i$  corresponding to the  $V^\dagger$  matrix of the singular value decomposition (3.6) and satisfying

$$\sum_{j_i=1}^d B_i^{j_i} B_i^{j_i \dagger} = I. \quad (3.26)$$

Having the left-canonical form of a matrix-product state at hand, its norm can be straightforwardly calculated from the rightmost tensor  $A_L$  as follows,

$$\begin{aligned} \langle \psi | \psi \rangle &= \sum_{j_1=1}^d \sum_{j_2=1}^d \cdots \sum_{j_L=1}^d \left( A_1^{j_1} A_2^{j_2} \cdots A_L^{j_L} \right)^\dagger \left( A_1^{j_1} A_2^{j_2} \cdots A_L^{j_L} \right) \langle j_1, j_2, \dots, j_L | j_1, j_2, \dots, j_L \rangle \\ &= \sum_{j_1=1}^d \sum_{j_2=1}^d \cdots \sum_{j_L=1}^d A_L^{j_L \dagger} \cdots A_2^{j_2 \dagger} A_1^{j_1 \dagger} A_1^{j_1} A_2^{j_2} \cdots A_L^{j_L} = \sum_{j_L=1}^d A_L^{j_L \dagger} A_L^{j_L} = 1. \end{aligned} \quad (3.27)$$

Note that the last equality in Eq. (3.27) holds only for the case of a normalized state  $|\psi\rangle$ . Analogously, using the right-canonical form of a matrix-product state, one finds that its norm is given by means of the leftmost tensor  $B_1$  via

$$\langle \psi | \psi \rangle = \sum_{j_1=1}^d B_1^{j_1} B_1^{j_1 \dagger}. \quad (3.28)$$

Most importantly, the mixed-canonical representation of a matrix-product state allows for a systematic truncation of the bond dimension. The mixed-canonical representation can be straightforwardly obtained by right-normalizing a left-canonical state. In doing so, after  $L - n + 1$  singular value decompositions one finds

$$|\psi\rangle = \sum_{j_1=1}^d \sum_{j_2=1}^d \cdots \sum_{j_L=1}^d A_1^{j_1} \cdots A_{n-1}^{j_{n-1}} D B_n^{j_n} \cdots B_L^{j_L} |j_1, j_2, \dots, j_L\rangle, \quad (3.29)$$

where  $A_n$  has been decomposed as  $A_{n;k_{n-1},k_n}^{j_n} = \sum_{k'} U_{k_{n-1},k'} D_{k',k'} V_{k',(j_n,k_n)}^\dagger$ , while the  $V^\dagger$  matrix has been reshaped into  $B_n$  and the  $U$  matrix has been absorbed into  $A_{n-1}$ , which still satisfies Eq. (3.21). It is worth noting that Eq. (3.29) can be understood as a Schmidt decomposition for a bipartition of the system into a part A comprising sites  $i = 1, 2, \dots, n-1$  and a part B comprising sites  $i = n, n+1, \dots, L$ . Indeed, using  $D = \text{diag}(s_1, \dots, s_\chi)$ ,  $|\psi\rangle$  can be rewritten as

$$|\psi\rangle = \sum_{k=1}^{\chi} s_k |\phi_k\rangle_A |\chi_k\rangle_B, \quad (3.30)$$

with two sets of orthonormal states ( $k = 1, 2, \dots, \chi$ )

$$|\phi_k\rangle_A = \sum_{j_1=1}^d \cdots \sum_{j_{n-1}=1}^d \left( A_1^{j_1} \cdots A_{n-1}^{j_{n-1}} \right)_{1,k} |j_1, \dots, j_{n-1}\rangle, \quad (3.31)$$

$$|\chi_k\rangle_B = \sum_{j_n=1}^d \cdots \sum_{j_L=1}^d \left( B_n^{j_n} \cdots B_L^{j_L} \right)_{k,1} |j_n, \dots, j_L\rangle. \quad (3.32)$$

Thus, by going through the matrix-product state from left to right, or, vice versa, from right to left, the entanglement entropy corresponding to the different bipartitions can be immediately accessed and the maximum bond dimension of each tensor might be truncated as discussed in the context of Eq. (3.11).

### Area laws of entanglement

By construction, matrix-product states obey a so-called area law of entanglement [224]. For any bipartition AB of the underlying lattice, with A comprising sites  $i = 1, \dots, n$  and B comprising sites  $i = n + 1, \dots, L$ , the entanglement entropy of a matrix-product state is bounded from above by

$$S(\rho_A) = S(\rho_B) \leq \log_2(\chi) , \quad (3.33)$$

where  $\chi$  denotes the bond dimension. In general, an area law of entanglement means that  $S(\rho_A)$  scales at most proportional to the boundary between the subsystem A and the subsystem B, which is constant for the bipartition of the one-dimensional matrix-product state described above.

As the bond dimension  $\chi$  cannot be increased arbitrarily in practical calculations, Eq. (3.33) puts a constraint on the set of quantum states that can be effectively represented as matrix-product states. Here, it is interesting to consider the expected entanglement entropy  $\mathbb{E}(S(\tilde{\rho}_A))$  for a random state  $\tilde{\psi}_{AB}$  of a  $(d^n \times d^{L-n})$ -dimensional system AB, with  $\tilde{\rho}_A = \text{tr}_B(|\tilde{\psi}_{AB}\rangle\langle\tilde{\psi}_{AB}|)$ . For large values of  $L$ , and in contrast to a matrix-product state, the random state  $\tilde{\psi}_{AB}$  obeys a volume law in the sense that the expected entanglement entropy scales linearly with the number of sites in A,  $\mathbb{E}(S(\tilde{\rho}_A)) \propto n$  [224]. Explicitly, for a  $(d^n \times d^{L-n})$ -dimensional random state  $\tilde{\psi}_{AB}$ , the expected entanglement entropy  $\mathbb{E}(S(\tilde{\rho}_A))$  was conjectured [225] and proven [226, 227] to be given by

$$\mathbb{E}(S(\tilde{\rho}_A)) = \frac{1}{\log(2)} \left( \frac{1 - d^n}{2d^{L-n}} + \sum_{k=d^{L-n}+1}^{d^L} \frac{1}{k} \right) , \quad (3.34)$$

considering  $n \leq L/2$  without loss of generality. Hence, one does not expect an effective matrix-product-state representation of a random state.

Luckily, the entanglement properties of the ground states of one-dimensional quantum systems are very favorable. This is directly related to the success of matrix-product-state approaches in simulating these systems [228, 229]. Indeed, it was proven that one-dimensional gapped Hamiltonians with short-ranged interactions satisfy an area law [230], while at criticality one expects a logarithmic scaling with the system size [231],

$S \propto \log_2(L)$ . However, in two-dimensional lattice systems, matrix-product-state based simulations are rendered inherently challenging by a given area law  $S \propto L$ , or possible logarithmic corrections thereof, which might arise close to criticality [232].

### Matrix-product operators and matrix-product-operator arithmetic

Practical calculations with matrix-product states, such as ground-state optimizations, time evolutions, or the mere computation of expectation values, require suitable representations of quantum lattice operators. Such matrix-product operators are very similar to the matrix-product states discussed above. The basic building blocks are tensors, which are here denoted by  $W_i$ , representing physical lattice sites  $i = 1, 2, \dots, L$ . The  $W_i$  tensors are lined up forming a chain of length  $L$ . However, in contrast to matrix-product states, the  $W_i$  tensors employed in matrix-product operators need to account for every possible combination of local basis states  $|j_i\rangle \langle j'_i|$  and, thus, they are of rank four. Two indices represent  $|j_i\rangle$  and  $\langle j'_i|$ , while the other two indices allow for a connection of the tensor  $W_i$  to its neighbors  $W_{i-1}$  and  $W_{i+1}$ . Explicitly, a matrix-product operator is of the form

$$O = \sum_{j_1=1}^d \sum_{j'_1=1}^d \sum_{j_2=1}^d \sum_{j'_2=1}^d \cdots \sum_{j_L=1}^d \sum_{j'_L=1}^d W_1^{j_1, j'_1} W_2^{j_2, j'_2} \cdots W_L^{j_L, j'_L} |j'_1, j'_2, \dots, j'_L\rangle \langle j_1, j_2, \dots, j_L|, \quad (3.35)$$

where  $W_i^{j_i, j'_i} W_{i+1}^{j_{i+1}, j'_{i+1}}$  needs to be understood as a matrix product. Applying a matrix-product operator with bond dimension  $\chi_1$  to a matrix-product state with bond dimension  $\chi_2$ , which is built from  $M_i$  tensors, means to contract tensors as

$$\sum_{j_i=1}^d W_{i; w_{i-1}, w_i}^{j_i, j'_i} M_{i, k_{i-1}, k_i}^{j_i} = \tilde{M}_{i; (k_{i-1}, w_{i-q}), (k_i, w_i)}^{j'_i}. \quad (3.36)$$

Hence, the resulting matrix-product state is constructed from  $\tilde{M}_i$  tensors, with bond dimension  $\chi = \chi_1 \chi_2$ . It is typically subjected to a truncation routine.

Actually, for simple quantum lattice operators, such as iconic spin-chain Hamiltonians or single-site operators, matrix-product-operator representations can be derived by means of pen and paper calculations, analyzing lattice-ordered operator strings [35, 233]. Elaborate generalizations of this basic idea have led to the automated construction of matrix-product operators using finite-state machines [234–240]. In the framework of this thesis, we follow a complementary approach, constructing generic matrix-product operators from the trivial representations of single-site operators, which might be summed

up and multiplied, as comprehensively discussed by Hubig et al. in Ref. [241]. Here, it is worth noting that the naive addition and multiplication of two matrix-product operators is typically not optimal as it drastically increases the bond dimension. At worst, the sum and the product of two matrix-product operators exhibit bond dimensions  $\chi = \chi_1 + \chi_2$  and  $\chi = \chi_1\chi_2$ , respectively, assuming  $\chi_1$  and  $\chi_2$  to be the bond dimensions of the addends or multiplicands. Hence, these operations should be equipped with an efficient truncation scheme. Matrix-product operators can in principle be truncated like matrix-product states, as described above. However, there is a subtle difference. Usually, matrix-product states are normalized and, thus, the squared singular values, or squared Schmidt coefficients, in Eq. (3.30) sum up to one. This does not apply to matrix-product operators, for which one often encounters extremely large singular values. Moreover, the overall norm of a matrix-product operator might be unevenly distributed among its tensors. Throughout this thesis, matrix-product operators are truncated using efficient rescaling singular value decompositions. This approach is comprehensively discussed in Ref. [241] and it usually leads to a uniform distribution of the operator's norm among its tensors.

### Exploiting symmetries in matrix-product states

The exploitation of the symmetries of a quantum lattice Hamiltonian, such as, for instance, a  $U(1)$  symmetry corresponding to the particle number conservation or a  $SU(2)$  spin symmetry, is common practice in modern matrix-product-state approaches [242–245]. In general, splitting the Hilbert space into different quantum symmetry sectors might drastically speed up numerical calculations or render them possible at all [84]. Furthermore, access to the individual symmetry sectors allows for canonical calculations at a fixed number of particles and for detailed studies of the spontaneous symmetry breaking of ground states [246].

Throughout this thesis we exploit the particle number conservation of the flux-ladder Hamiltonian, which was introduced in Eq. (2.1). As opposed to the case of non-abelian symmetries [233, 247–249], the implementation of the corresponding  $U(1)$  symmetry in the matrix-product-state formalism is fairly straightforward. It is discussed in detail in Sec. 3.4, where we also introduce the canonical finite-temperature method which has been implemented in the framework of this thesis.

### 3.3 Density-matrix renormalization-group method

Since its invention by Steven R. White in 1992 [32], the density-matrix renormalization-group method has indeed become the leading method for the numerical study of one-dimensional quantum lattice systems and it has become useful for higher dimensions as well.

The objective of the method is to find the ground state of a given lattice Hamiltonian  $H$ . Concretely, this means to minimize the energy,

$$\min_{|\psi\rangle} \langle \psi | H | \psi \rangle , \quad (3.37)$$

while paying attention to the normalization of the matrix-product state  $|\psi\rangle$ . At the core of the variational algorithm, ground-state optimization is achieved by iterative updates of the individual matrix-product-state tensors representing local lattice sites. Specifically, the tensors are improved one after the other by repeatedly sweeping through the matrix-product state from left to right and, vice versa, from right to left. Comprehensive and detailed descriptions of the algorithm can be found in the existing literature [35]. In the framework of this thesis, we typically employ the single-site variant using subspace expansion [250], which exhibits remarkable convergence properties. Key aspects of the method are discussed in the following.

Let us start off diving right into the core of the algorithm considering a mixed-canonical matrix-product state

$$|\psi\rangle = \sum_{j_1=1}^d \sum_{j_2=1}^d \cdots \sum_{j_L=1}^d A_1^{j_1} \cdots A_{i-1}^{j_{i-1}} M_i^{j_i} B_{i+1}^{j_{i+1}} \cdots B_L^{j_L} |j_1, j_2, \dots, j_L\rangle , \quad (3.38)$$

with a tensor  $M_i$  at the center of orthogonality, that is enclosed between  $A_h$  tensors (for  $h < i$ ) and  $B_j$  tensors (for  $j > i$ ) satisfying Eq. (3.21) and Eq. (3.26), respectively. Further, we assume a matrix-product-operator representation of the Hamiltonian  $H$ , which is given by means of  $W_i$  tensors, as discussed in the context of Eq. (3.35). In order to update the central tensor  $M_i$ , one evaluates the derivative of the Lagrangian function  $\langle \psi | H | \psi \rangle - \lambda \langle \psi | \psi \rangle$  with respect to  $M_i^*$ , that is,

$$\frac{\partial}{\partial M_{i;k'_{i-1},k'_i}^{*j'_i}} (\langle \psi | H | \psi \rangle - \lambda \langle \psi | \psi \rangle) = 0 \quad (3.39)$$

for  $j'_i = 1, 2, \dots, d$ ,  $k'_{i-1} = 1, 2, \dots, \chi$ , and  $k'_i = 1, 2, \dots, \chi$ . Assuming the mixed-canonical representation of  $|\psi\rangle$  and reshaping  $M_i$  into a vector, Eq. (3.39) can be under-

stood as an eigenvalue problem for a Hermitian ( $d\chi^2 \times d\chi^2$ ) matrix, given by

$$\sum_{k_{i-1}=1}^{\chi} \sum_{j_i=1}^d \sum_{k_i=1}^{\chi} \sum_{w_{i-1}=1}^{\chi'} \sum_{w_i=1}^{\chi'} L_{i-1;k_{i-1},w_{i-1},k'_{i-1}} W_{i;w_{i-1},w_i}^{j_i,j'_i} R_{i+1;k_i,w_i,k'_i} M_{i;k_{i-1},k_i}^{j_i} = \lambda M_{i;k'_{i-1},k'_i}^{j'_i}, \quad (3.40)$$

where  $\chi'$  denotes the bond dimension of the matrix-product operator  $H$ , while  $L_i$  and  $R_i$  represent contractions of  $\langle \psi | H | \psi \rangle$  up to site  $i$  from the left and from the right, respectively. Explicitly,  $L_i$  and  $R_i$  are recursively defined by means of

$$\begin{aligned} L_{i;k_i,w_i,k'_i} &= \sum_{k_{i-1}=1}^{\chi} \sum_{w_{i-1}=1}^{\chi'} \sum_{k'_{i-1}=1}^{\chi} L_{i-1;k_{i-1},w_{i-1},k'_{i-1}} \sum_{j_i=1}^d \sum_{j'_i=1}^d A_{i;k_{i-1},k_i}^{j_i} W_{i;w_{i-1},w_i}^{j_i,j'_i} A_{i;k'_{i-1},k'_i}^{*j'_i}, \\ R_{i;k_{i-1},w_{i-1},k'_{i-1}} &= \sum_{k_i=1}^{\chi} \sum_{w_i=1}^{\chi'} \sum_{k'_i=1}^{\chi} R_{i+1;k_i,w_i,k'_i} \sum_{j_i=1}^d \sum_{j'_i=1}^d B_{i;k_{i-1},k_i}^{j_i} W_{i;w_{i-1},w_i}^{j_i,j'_i} B_{i;k'_{i-1},k'_i}^{*j'_i}, \end{aligned} \quad (3.41)$$

where  $L_0$  and  $R_{L+1}$  are the trivial ( $1 \times 1 \times 1$ ) identity tensor. Hence, Eq. (3.40) is solved for the smallest eigenvalue  $\lambda$ , which corresponds to the energy of the optimized state. The corresponding eigenvector represents the optimized tensor  $M_i$ . It is worth noting that a complete diagonalization of the ( $d\chi^2 \times d\chi^2$ ) matrix is not necessary because one is only interested in the smallest eigenvalue. Iterative Lanczos [251] or Jacobi-Davidson [252, 253] methods allow for an efficient solution of the problem at hand. In these routines, the current tensor  $M_i$ , which was optimized in a previous sweep, is a good starting point.

Having optimized the tensor  $M_i$ , a left-to-right (right-to-left) sweep proceeds as follows. First,  $M_i$  is subjected to a singular value decomposition. In doing so, the center of orthogonality of the mixed-canonical representation of  $|\psi\rangle$  is shifted to site  $i+1$  ( $i-1$ ). Second, the contraction  $L_i$  ( $R_i$ ), as defined in Eq. (3.41), is computed using the newly optimized  $A_i$  ( $B_i$ ) and stored in memory. Finally, one starts over with the optimization of  $M_{i+1}$  ( $M_{i-1}$ ). Typically, the overall ground-state optimization involves multiple sweeps at different values of the maximum bond dimension  $\chi$ . Despite the general complexity of finding ground states [254], the overall convergence of the algorithm can in practice be ensured by tracking the decay of the optimized energy  $\langle H \rangle$  and the decay of the variance  $\langle H^2 \rangle - \langle H \rangle^2$ , noting that the latter can be effectively approximated with little computational effort [255].

We conclude this section with a few comments. Originally, the density-matrix renormalization-group method [32, 33] was not formulated in the matrix-product-state framework. The connection between the original algorithm [34] and variants of matrix-product states [61, 62, 256–258] was drawn in Refs. [259–261] and is comprehensively

discussed in Ref. [35]. Modern implementations of the algorithm are based on matrix-product states. While the ground-state optimization described above scales linearly with the system size  $L$ , it should be stressed that there are also algorithms for translationally invariant states which directly work in the thermodynamic limit [262].

### 3.4 Finite-temperature calculations with matrix-product states

In order to explore the effect of finite-temperatures in bosonic flux ladders, a matrix-product-state based purification approach has been implemented in the framework of this thesis. Here, we provide details of the method, putting a particular focus on canonical simulations, which preserve a fixed number of particles. Note that the finite-temperature results are presented in Ch. 5.

The core concept of purification is that a mixed state in a physical space can be represented as the partial trace of a pure state in an artificially extended space [88]. Thus, by incorporating an auxiliary counterpart for each physical site, thermal states can be represented as matrix-product states and propagated in imaginary time using well-developed techniques [233, 263–276]. Here, suitable initial infinite-temperature states need to be chosen.

For grand-canonical calculations these states are straightforward to generate [35]. They exhibit maximum entanglement between each physical site and its auxiliary counterpart but are otherwise of product form. Here, an illustrative example is the Bell state of two qubits A and B, which was discussed in the context of Eq. (3.1). We recap that by tracing out system B, which might be understood as the auxiliary site accompanying the physical site A, one is left with the maximally mixed infinite-temperature state of system A, as given in Eq. (3.2).

On the other hand, the required initial states for canonical simulations, which are for a fixed number of particles, exhibit nontrivial long-range correlations. They have been successfully obtained as the ground states of specifically chosen Hamiltonians using the density-matrix renormalization-group method [277–279].

In this thesis, we generate matrix-product-state representations of canonical infinite-temperature states by employing a bookkeeping mechanism that explicitly accounts for the occupation of physical sites on the level of the matrix-product state. We emphasize that the purification approach employed here is similar to the one discussed by T. Barthel in Ref. [266]. Importantly, it renders the generation of canonical infinite-temperature states straightforward.

Our purification approach can be subdivided into three steps. First, a matrix-product-state representation of the canonical or grand-canonical infinite-temperature state is constructed. Second, a suitable matrix-product-operator representation of the propagator  $\exp(-\beta H)$  is constructed, where  $\beta = 1/T$  is the inverse temperature. A third step involves the imaginary-time propagation, including the control of errors, to obtain a thermal state corresponding to a finite temperature. In the remainder of this section, we describe all steps in greater detail.

### Matrix-product-state structure

The matrix-product states employed during canonical and grand-canonical purification simulations are comprised of tensors representing physical sites and their auxiliary counterparts. These tensors are aligned side by side following a zigzag pattern through the two-leg flux ladder with  $L$  rungs, forming a chain of length  $4L$ . The structure of the corresponding matrix-product state is sketched in Fig. 3.1.

Since canonical calculations are at a fixed number of particles, which is conserved by the flux-ladder Hamiltonian (2.1), we need the matrix-product state to account for the corresponding symmetry. In practice, this means that on the level of each tensor a bookkeeping mechanism needs to be implemented. This mechanism keeps track of the total occupation number of the physical sites when going through the matrix-product state from left to right. At this point, we recap that the conventional building blocks of a matrix-product state are rank-three — also referred to as three-legged — tensors, which are, in analogy to the discussion in Sec. 3.2, denoted by  $M_{j;i,o}^p$  for site  $j$ . In general the tensor legs are directed, meaning that they are considered to be either incoming or outgoing. The incoming leg  $p$ , which is usually referred to as physical leg, corresponds to local basis states of the lattice site represented by the tensor. The incoming leg  $i$  and the outgoing leg  $o$  enable a connection between the tensor and its neighbors within the matrix-product state. Against this background, the employed bookkeeping mechanism can be understood as a subdivision of the vector spaces associated with each of the conventional legs into sectors corresponding to different occupation numbers. More precisely, for each tensor, the sectors  $\{n_i\}$  of its incoming leg  $i$  correspond to occupation numbers of the physical sites that are represented by the tensors to its left. Analogously, for each tensor, the sectors  $\{n_o\}$  of its outgoing leg  $o$  correspond to occupation numbers of the physical sites that are represented by the tensor itself and by the tensors to its left. Moreover, the sectors  $\{n_p\}$  subdividing an incoming leg  $p$  refer to the local occupation numbers of the basis states. Hence, the outgoing leg  $o$  of the leftmost tensor of the

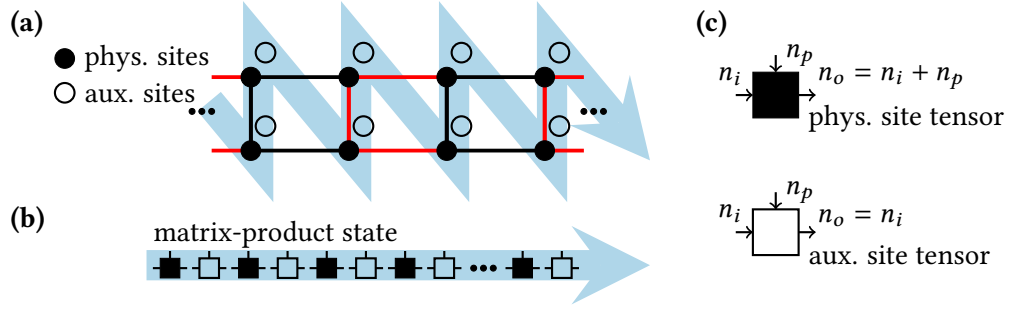


**Figure 3.1: Sketch of the matrix-product-state structure employed in the canonical purification approach.** (a) Sketch of the two-leg ladder Hamiltonian. The bonds (black and red solid lines) represent the Hamiltonian terms and filled circles represent the physical lattice sites. In the purification approach, each physical site is accompanied by an auxiliary counterpart represented by an empty circle. (b) The matrix-product state is comprised of tensors representing physical sites (filled squares) and of tensors representing auxiliary sites (empty squares). These tensors are aligned side by side following a zigzag pattern through the ladder as indicated by the blue arrows in (a) and (b). (c) The canonical purification approach requires the bookkeeping of the total occupation of all physical sites. Therefore, the incoming left leg  $i$  of each tensor is split into blocks  $\{n_i\}$  referring to different occupations of the physical sites to the left of the specific tensor. Similarly, the incoming leg  $p$  entering each tensor from above is split into blocks  $\{n_p\}$  referring to the occupation of the specific site represented by the tensor, and the outgoing leg  $o$  to the right of each tensor is split into blocks  $\{n_o\}$  referring to the occupation of all physical sites to the left of the specific tensor including the tensor itself.

matrix-product state contains information about the total occupation of all physical sites. This bookkeeping mechanism is illustrated in Fig. 3.1(c).

### Canonical infinite-temperature state

Matrix-product operators are required for the preparation of the canonical or grand-canonical infinite-temperature state as well as for the subsequent propagation in imaginary time. Note that in the framework of this thesis they are consistently constructed from single-site operators following the generic approach put forward by Hubig et al. [241] and discussed in Sec. 3.2. Considering a ladder with hard-core bosons, a possible grand-canonical infinite-temperature state  $|\beta = 0\rangle_{\text{g.c.}}$  can be readily constructed using particle-creation operators  $a_{i,\text{phys.}}^\dagger$  and  $a_{i,\text{aux.}}^\dagger$  acting on physical sites  $i$  and their auxiliary counterparts, respectively. This state spreads over all possible sectors corresponding to total occupation numbers of the physical sites ranging from zero to  $2L$ .

Explicitly, it is given by the following product involving all physical lattice sites  $i$

$$|\beta = 0\rangle_{\text{g.c.}} = \prod_i \frac{1}{\sqrt{2}} \left( a_{i,\text{phys.}}^\dagger + a_{i,\text{aux.}}^\dagger \right) |\text{vac}\rangle, \quad (3.42)$$

with  $|\text{vac}\rangle$  being the vacuum state with zero particles.

We emphasize that a suitable canonical infinite-temperature state with a fixed total occupation number can be obtained from  $|\beta = 0\rangle_{\text{g.c.}}$  by means of a projection onto the corresponding particle number sector and subsequent normalization. Moreover, the matrix-product-state structure introduced above renders this projection straightforward: all but the symmetry sector of interest are set to zero at the very right end of the matrix-product state. Finally, the canonical infinite-temperature state with a fixed total occupation number of  $N$  particles is given by

$$|\beta = 0\rangle_{\text{c}} = \mathcal{P}_N |\beta = 0\rangle_{\text{g.c.}}, \quad (3.43)$$

where  $\mathcal{P}_N$  denotes a projection onto the  $N$ -particle subspace and subsequent normalization of the matrix-product state.

### Propagation in imaginary time

The imaginary-time evolution requires a matrix-product-operator representation of the propagator  $e^{-\beta H} = (e^{-\tau H})^{\beta/\tau}$ . For this, we subdivide the ladder Hamiltonian into two parts,  $H = H_0 + H_1$ , corresponding to the black and red bonds in the sketch in Fig. 3.1, and approximate the time-evolution operator by means of a second-order Trotter decomposition [280],

$$e^{-\tau H} = e^{-\tau H_0/2} e^{-\tau H_1} e^{-\tau H_0/2} + \mathcal{O}(\tau^3). \quad (3.44)$$

Note that the Hamiltonian parts  $H_0$  and  $H_1$  can be diagonalized numerically because they are composed of commuting contributions which are associated with every second plaquette of the ladder. Hence, the matrix-product operators representing the exponentials in Eq. (3.44) can be constructed automatically from single-site operators using common matrix-product-operator arithmetic [241]. In terms of the employed matrix-product-state structure, the Hamiltonian  $H$  exhibits at most fourth-nearest-neighbor interactions, while the propagators  $e^{-\tau H_0}$  and  $e^{-\tau H_1}$  exhibit at most sixth-nearest-neighbor interactions.

The imaginary-time propagation is based on the sequential application of matrix-product operators representing the propagators on the right-hand side of Eq. (3.44).

Choosing a suitable step width  $\tau$ , the operators are repeatedly applied to the initial canonical or grand-canonical infinite-temperature state  $|\beta = 0\rangle_c$  or  $|\beta = 0\rangle_{g.c.}$ , which decreases the temperature of the so-evolved thermal state. Between these applications, the bond dimension of the evolved matrix-product state needs to be truncated and, due to the fact that the imaginary-time propagators are not unitary, the matrix-product state also needs to be repeatedly normalized. During the imaginary-time propagation, errors arise due to the Trotter decomposition of the propagator and due to the repeated truncation of the evolved state. Regarding the numerical results presented in this thesis, these errors are controlled independently by comparing results obtained for different truncation thresholds at fixed Trotter-step widths and vice versa. We note that the error control can in principle be based on the monitoring of state overlaps. However, it is usually sufficient to focus on the values obtained for the actual observables of interest.

### 3.5 Time-propagation of matrix-product states

The time evolution of a quantum state is formally given by  $|\psi(t)\rangle = \exp(-iHt)|\psi(0)\rangle$ , where  $H$  is the underlying time-independent Hamiltonian and  $|\psi(0)\rangle$  is the initial state at time  $t = 0$ . In this section, we touch on well established time-evolution methods in the matrix-product-state framework. They are comprehensively discussed by Paeckel et al. in Ref. [36]. Some of these methods, as implemented in the SyTen toolkit [245], are employed for the simulation of quantum quench dynamics in Ch. 4 and in Ch. 6.

In general, matrix-product-state based time-evolution methods fall into two categories. They are either based on approximations of the propagator  $\exp(-iHt)$  by means of suitable matrix-product operators or they directly approximate the time-evolved state  $|\psi(t)\rangle$ , avoiding the explicit construction of a propagator and using a matrix-product-operator representation of the Hamiltonian  $H$  only.

The most prominent approximation of the propagator is based on a second-order Trotter decomposition [280] and the surrounding method is often referred to as time-evolving block-decimation [231, 263, 281]. Note that we have already introduced the Trotter decomposition in the context of Eq. (3.44) for the purpose of an imaginary-time propagation. We recap that in this scheme, the Hamiltonian  $H$  is split into two parts,  $H = H_0 + H_1$ , which are composed of small commuting contributions, such that  $\exp(-iH_0t)$  and  $\exp(-iH_1t)$  can be constructed explicitly and employed for the approximation of  $\exp(-iHt)$ . Hence, this scheme is very efficient for Hamiltonians with nearest-neighbor interactions. In this case the method exhibits a constant error per lattice site. It is not directly applicable to Hamiltonians with long-range interactions.

However, extending the method by means of swap gates allows to also address long-range interactions [272]. Furthermore, improved Euler integration steppers with feasible matrix-product-operator representations allow to efficiently approach Hamiltonians with long-range interaction terms, introducing only a constant error per lattice site [267].

Methods which overcome the explicit construction of the propagator include global and local Krylov subspace methods [36, 238, 282, 283] and the time-dependent variational-principle algorithm [284, 285]. The global Krylov method represents a very generic approach and does not rely on the specifics of the matrix-product-state formalism. It is based on the construction of an orthonormal basis for the Krylov subspace. Explicitly, the Krylov subspace is the span of  $\{|\psi(0)\rangle, H|\psi(0)\rangle, \dots, H^{n-1}|\psi(0)\rangle\}$  and  $n$  denotes its dimension. In practical applications, one typically considers the subspace dimension to be  $n \lesssim 10$ . In the global Krylov method, the time-evolved state  $|\psi(t)\rangle$  is approximated by means of a formal projection of the propagator  $\exp(-iHt)$  onto the subspace introduced above. The method allows for a cheap interpolation on very fine time grids. For the purpose of a further propagation, it might be worth checking if parts of the Krylov subspace can be recycled [36]. A major practical difficulty of the method is the required orthonormalization of the Krylov basis states, which can be much more entangled than the time-evolved state itself. A practical maximum bond dimension in the matrix-product-state framework requires the truncation of these states, which introduces additional errors.

In contrast to the global Krylov method, the local Krylov method and the time-dependent variational-principle algorithm are tailored towards the matrix-product-state formalism and bear similarities to the density-matrix renormalization-group method. At their core, working with a mixed-canonical representation of  $|\psi(t)\rangle$ , both methods time-evolve local matrix-product-state tensors at the center of orthogonality using a Krylov procedure. In both cases, the global state  $|\psi(t)\rangle$  is evolved in time by sweeping through the matrix product state. While the time-dependent variational-principle algorithm enforces that the propagated state lies within the manifold of matrix-product states with a particular bond dimension, the local Krylov method is based on a decomposition of the Hamiltonian  $H$  into local subspaces. The detailed derivation of both methods is rather technical and extensively discussed in Ref. [36]. It is worth noting that there are well-established single-site variants [284, 286] and two-site variants [285] of the time-dependent variational-principle algorithm.

Finally, we note that in practice, the errors introduced by the methods discussed above can be well controlled. The simulation of time evolutions is ultimately limited by

the growth of the entanglement entropy, which can be linear in time for one-dimensional systems [287].

## Interacting bosonic flux ladders with a synthetic dimension

In this chapter, we study ground-state phases and quench dynamics in a synthetic flux-ladder model. Putting the emphasis on model parameters which can be experimentally realized in an ultracold quantum-gas platform exploiting two internal states of the potassium isotope  $^{41}\text{K}$  as a synthetic dimension, we map out the ground-state phase diagram using extensive density-matrix renormalization-group simulations. The focus is on accessible observables such as the chiral current and the leg-population imbalance. Considering a particle filling of one boson per rung, we report on the existence of a Mott-insulating Meissner phase as well as biased-ladder phases on top of superfluids and Mott insulators. Moreover, for suitably chosen initial states, we demonstrate that quantum quenches can be used to probe the equilibrium properties in the transient dynamics. Concretely, we consider the instantaneous turning on of rung hopping or leg hopping in the synthetic flux-ladder model, with different initial particle distributions. We show that clear signatures of the biased-ladder phase might be observed in the transient dynamics. Furthermore, the behavior of the chiral current in the transient dynamics is discussed.

This chapter is organized as follows. In Sec. 4.1, we discuss the envisioned experimental realization of a bosonic flux ladder in the interacting regime. The prospect of this future experiment motivates our choice of the model parameters. We map out the corresponding ground-state phase diagram in Sec. 4.2. Quantum quenches in the synthetic flux-ladder model are discussed in Sec. 4.3. Finally, we summarize our work on the synthetic flux-ladder model in Sec. 4.4.

### 4.1 Specifics of the experimental implementation

Using  $^{41}\text{K}$  atoms, interacting bosonic flux ladders with a synthetic dimension are envisioned to be realized by the ultracold quantum gases group led by Leticia Tarruell at ICFO. Here, we touch on the experimental proposal, which justifies our choice of model parameters and which has been put forward in Ref. [2].

In order to implement the synthetic flux-ladder model, which was introduced in

Ch. 2 and is recapped here for the sake of completeness,

$$\begin{aligned}
H = & -J \sum_{r=0}^{L-2} \sum_{l=0}^1 \left( a_{r,l}^\dagger a_{r+1,l} + \text{H.c.} \right) - J_\perp \sum_{r=0}^{L-1} e^{-ir\phi} \left( a_{r,0}^\dagger a_{r,1} + \text{H.c.} \right) \\
& + \sum_{l=0}^1 \frac{U_l}{2} \sum_{r=0}^{L-1} n_{r,l} (n_{r,l} - 1) + V \sum_{r=0}^{L-1} n_{r,0} n_{r,1} , \tag{4.1}
\end{aligned}$$

first, the atoms are trapped and their motion is confined to nearest-neighbor hopping in an array of parallel and effectively one-dimensional lattices. More specifically, this array is realized by counter-propagating lattice laser beams, which exhibit a wavelength  $\lambda_L = 1064$  nm, and each of the one-dimensional lattices in the array represents a copy of the flux-ladder model.

Second, in setups exploiting a synthetic dimension, the legs of the ladder are represented by different internal states of the atoms. Explicitly, in the envisioned experiment, the Zeeman sublevels  $m_F = -1$  and  $m_F = 0$  of the  $F = 1$  hyperfine manifold of the  $^{41}\text{K}$  atoms are identified with the  $l = 0$  leg and the  $l = 1$  leg of the flux-ladder Hamiltonian introduced in detail in the context of Eq. (2.1) and also given above in Eq. (4.1). A coherent coupling of the spin states via two-photon Raman transitions implements complex nearest-neighbor rung hopping along the synthetic spin dimension. This is achieved by additional counter-propagating laser beams which exhibit a wavelength  $\lambda_R = 769$  nm. Most importantly, this naturally leads to effective Peierls phases in the rung gauge, as described in Sec. 2.1. The overall rung hopping strength  $J_\perp$  can be controlled by means of the intensity of the Raman lasers. In the situation that is most easily realized in the future experiment, the Raman lasers are aligned in parallel with the longitudinal lattice lasers. In this setting, the effective magnetic flux per plaquette is given by

$$\phi/(2\pi) = 1064/769 , \tag{4.2}$$

defining the magic value of  $\phi$  considered throughout this chapter.

At this point, we recap that the exploitation of synthetic dimensions for the realization of flux ladders was originally proposed by Celi et al. in 2014 [172]. Subsequently, the first synthetic flux ladders were realized with bosonic  $^{87}\text{Rb}$  atoms [139] as well as with fermionic  $^{173}\text{Yb}$  atoms [140] in the noninteracting regime in 2015. So far, implementations of interacting flux ladders have remained elusive in various platforms due to the detrimental heating processes accompanying the experimental methods employed for the emulation of strong magnetic fields [153]. The study of the dynamics of two repulsively interacting bosons on a real-space flux ladder by Tai et al. [144] represents noteworthy step towards the many-body case.

A major objective of the future experiment at ICFO is to access the interacting regime. For this purpose, the considered setup with a synthetic dimension is particularly promising because the driving frequency corresponds to the Zeeman splitting between atomic sublevels, which is several orders of magnitude larger than in other Floquet-based schemes, and, therefore, one expects negligible heating due to the coupling to the atomic motion. In ultracold quantum gases, interparticle interactions are typically described by their scattering lengths. For the considered internal atomic states, the  $(m_F = -1)$ – $(m_F = -1)$  collisions exhibit very similar and positive scattering lengths as the  $(m_F = 0)$ – $(m_F = 0)$  collisions, which practically realizes symmetric on-site interactions  $U_0 = U_1$  in the flux-ladder model introduced in Eq. (2.1). Moreover, the interparticle-interaction-to-hopping ratio  $U/J$  can be adjusted by controlling the longitudinal lattice depth. Also, the scattering length of the  $(m_F = 0)$ – $(m_F = 1)$  collisions can in principle be controlled by varying an external magnetic field and exploiting a Feshbach resonance [98, 288, 289]. However, the first experimental effort will most likely concentrate on the large external magnetic field limit, where the two-photon Raman transitions are insensitive to magnetic field fluctuations. In this limit, the scattering lengths of all three types of collisions,  $(m_F = -1)$ – $(m_F = -1)$ ,  $(m_F = 0)$ – $(m_F = 0)$ , and  $(m_F = -1)$ – $(m_F = 0)$ , are essentially the same, which corresponds to the case of SU(2) symmetric rungwise interactions,

$$U = U_0 = U_1 = V, \quad (4.3)$$

that we will focus on in this chapter. It is stressed that for the case of SU(2) symmetric interactions and the specific value of the magnetic flux given in Eq. (4.2), the large parameter regime spanned by  $U/J \in [2.5, 20]$  and  $J_\perp/J \in [0.2, 30]$ , which is considered in the numerical simulations presented in this chapter, is expected to be within experimental reach. Throughout this chapter, in all simulations we consider a particle filling of one boson per rung,  $\nu = N/(2L) = 1/2$ . This situation might be realized by starting with a Mott-insulating state occupying a single leg of the ladder with one particle per lattice site, that is, a single spin state, vanishing rung hopping  $J_\perp = 0$ , and negligible leg hopping  $J$ . Subsequent turning on of the coupling between the two spin states, or rung hopping  $J_\perp$ , initializes the flux ladder with one particle per rung. This preparation scheme allows to realize the initial states considered in the quench protocols discussed in Sec. 4.3.

Accessible observables in the proposed setup include the leg-population imbalance, leg-resolved momentum-distribution functions, and the chiral current. Specifically, the occupation of the individual legs,  $N_0$  and  $N_1$ , can be determined using Stern-Gerlach

separation because the legs correspond to different spin states. Here, we recap that a finite leg-population imbalance  $\Delta_l = |N_0 - N_1| / (N_0 + N_1)$ , as introduced in the context of Eq. (2.21), is the key feature of the biased-ladder phase. Similarly, Stern-Gerlach separation during time-of-flight expansion allows for the measurements of leg-resolved momentum-distribution functions and chiral currents, which were discussed in detail Sec. 2.1.2 [139, 140, 172].

Finally, concerning our numerical work on the synthetic flux-ladder model, we note the ground-state phase diagrams of very similar models have been discussed in detail and mapped out to a large extent within previous studies [194–205]. However, exploring the exact parameter regimes that could be accessed in future experiments, including the impact of rungwise interactions, which are typically present in synthetic dimension implementations, investigating the role of finite energy densities and temperatures [183, 192, 204, 206] on the ground-state phase diagrams [186], and developing optimal state-preparation schemes [207] and detection protocols [174, 208–212], which might be based on the dynamics induced by feasible quantum quenches, remain important open questions, which are partially addressed in this chapter.

## 4.2 Zero-temperature phase diagram

In the following, we map out the ground-state phase diagram of the synthetic flux-ladder model at particle filling one-half,  $\nu = N/(2L) = 1/2$ , considering SU(2) symmetric rungwise interactions,  $U_0 = U_1 = V = U$ . We report on a superfluid as well as a Mott-insulating biased-ladder phase and a Mott-insulating Meissner phase.

### Overview

Let us start with Fig. 4.1, which shows the phase diagram as a function of the inter-leg hopping strength  $J_\perp$  and the interaction strength  $U$ . Within the parameter region spanned by  $U/J \in [2, 8]$  and  $J_\perp/J \in [0.2, 0.7]$ , extensive density-matrix renormalization-group simulations clearly reveal three kinds of phases: (i) The ground states in the Mott-insulating Meissner phase exhibit uniform particle-density profiles and uniform local current patterns with an effective unit cell comprising one plaquette of the ladder. Moreover, as shown in Fig. 4.2(d), the central charge  $c = 0$  of the Mott-insulating Meissner phase can be well reproduced from the entanglement entropy in the ground state. (ii) The Mott-insulating biased-ladder phase has a central charge of  $c = 0$ , and, most importantly, it features a finite leg-population imbalance,  $\Delta_l > 0$ . (iii) The superfluid biased-ladder phase exhibits a finite leg-population imbalance and a central charge

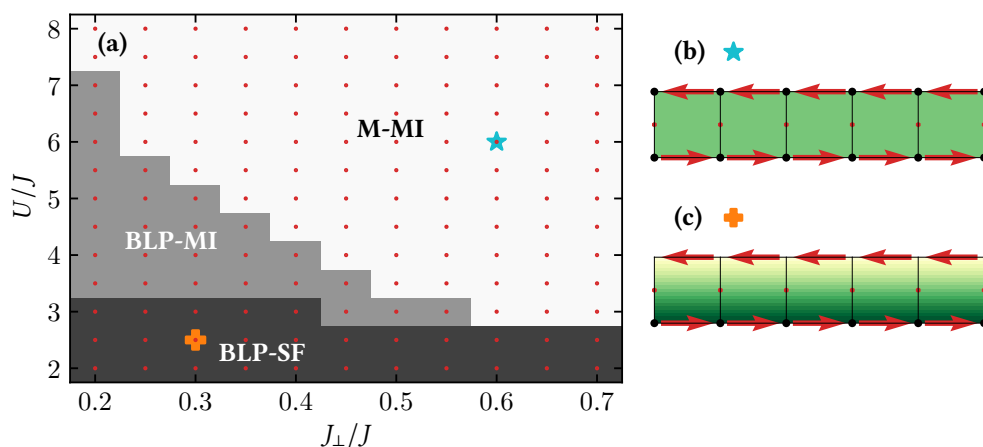


**Figure 4.1:** Ground-state phase diagram with superfluid biased-ladder (BLP-SF), Mott-insulating biased-ladder (BLP-MI), and Mott-insulating Meissner (M-MI) phases. Considering a particle filling  $\nu = 1/2$ ,  $SU(2)$  symmetric interactions  $U_0 = U_1 = V = U$ , and a magnetic flux  $\phi/(2\pi) = 1064/769$ . (a) Dark gray shading indicates the BLP-SF. Light gray shading indicates the BLP-MI. Bright regions indicate the M-MI. Actual ground states have been computed for the values of  $J_{\perp}$  and  $U$  indicated by the red dots, considering ladders with  $L = 40, 60$ , and  $80$  rungs. Note that for noninteracting bosons ( $U = 0$ ), the critical value of  $J_{\perp}$  corresponding to the vortex-to-Meissner transition is given by  $J_{\perp}^c/J = 4.88$  [64, 196]. The panels (b) and (c) show local density profiles and current patterns in the M-MI ( $J_{\perp}/J = 0.6$ ,  $U/J = 6$ ) and BLP-SF ( $J_{\perp}/J = 0.3$ ,  $U/J = 2.5$ ), respectively. The size of the dots and the background shading indicate the local particle density. The red arrows show the local current patterns. The data shown in (b) and (c) are for the six most central rungs of a ladder comprising a total number of  $L = 80$  rungs.

$c = 1$ , which can also be reproduced from the numerical data. Note that local particle currents and particle-density profiles in the Mott-insulating Meissner phase and in the superfluid biased-ladder phase are exemplified in Fig. 4.1(b) and Fig. 4.1(c), respectively.

### Charge gap and entanglement entropy

For the purpose of distinguishing between the Mott-insulating and the superfluid phases, we analyze the charge gap

$$\Delta\mu = \epsilon_{N+1} + \epsilon_{N-1} - 2\epsilon_N. \quad (4.4)$$

Here,  $\epsilon_N$  denotes the ground-state energy of a setup with  $N$  particles and particle filling  $\nu = N/(2L)$ . A vanishing charge gap,  $\Delta\mu = 0$ , indicates a superfluid phase, while a finite charge gap in the thermodynamic limit,  $\lim_{L \rightarrow \infty} \Delta\mu > 0$ , reveals a Mott

insulator. It is worth noting that the limit value  $\lim_{L \rightarrow \infty} \Delta\mu$  is estimated by means of a linear extrapolation of finite-size data in  $1/L$ . Concretely, for this purpose, we consider ladders with  $L = 40, 60,$  and  $80$  rungs.

We emphasize that the presence of rungwise interactions,  $V > 0$ , generally enhances the stability of the biased-ladder phase. Interestingly, it has been shown in Refs. [290, 291] that a finite leg-population imbalance,  $\Delta_l > 0$ , can be found even in the absence of a magnetic field, if the strength of the rungwise interactions exceeds the site-local interaction strength. However, one does not expect this — and we have not found any evidence — for a finite population imbalance at zero flux and close-to  $SU(2)$  symmetric interactions.

Figure 4.2 provides details about the ground-state phases shown in Fig. 4.1. Specifically, Fig. 4.2(a), Fig. 4.2(b), and Fig. 4.2(c) show the particle number  $N$  in the grand-canonical ground state as a function of the chemical potential  $\mu$  for  $U/J = 2.5, U/J = 4.5,$  and  $U/J = 7$ , respectively, considering  $J_\perp/J = 0.3$ . Note that these parameters are also considered in Fig. 4.1. The plateaus at  $N = L$  in the  $N$  versus  $\mu$  curves shown in Fig. 4.2(b) and Fig. 4.2(c) are indicative for the Mott-insulating phases. Figure 4.2(d) shows the entanglement entropy  $S(r)$  as obtained for bipartitions corresponding to cuts between rung  $(r - 1)$  and rung  $r$ , for different interaction strengths  $U/J = 2.5$  (biased-ladder superfluid,  $c = 1$ ),  $U/J = 4.5$  (biased-ladder Mott-insulator,  $c = 0$ ), and  $U/J = 7$  (Mott-insulating Meissner phase,  $c = 0$ ), considering a particle filling  $\nu = 1/2$ . In this connection, we note that the ground-state entanglement entropy is predicted to scale as [231, 292]

$$S(r) = \frac{c}{6} \log \left( \frac{L}{\pi} \sin \left( \frac{\pi r}{L} \right) \right) + g, \quad (4.5)$$

with  $c$  being the central charge and  $g$  a nonuniversal constant. The red line in Fig. 4.2 is obtained by least-square fitting the offset  $g$  in the expression above to the  $U/J = 2.5$  data, considering a central charge  $c = 1$ , which is expected for the superfluid biased-ladder phase and shows excellent agreement with the numerical results.

### Momentum-distribution functions

In Fig. 4.3, we exemplify leg-resolved ( $l = 0, 1$ ) momentum-distribution functions  $\bar{n}_l(k)$ , as defined in Eq. (2.11), in the biased-ladder superfluid phase and in the Mott-insulating Meissner phase. Figure 4.3(a) and Fig. 4.3(b) show  $\bar{n}_1(k)$  and  $\bar{n}_0(k)$  in the superfluid biased-ladder phase, for  $J_\perp = 0.3J$  and  $U = 2.5J$ . Note that for the considered parameters, the particle numbers in the two legs,  $N_0$  and  $N_1$ , as well as the maximum values

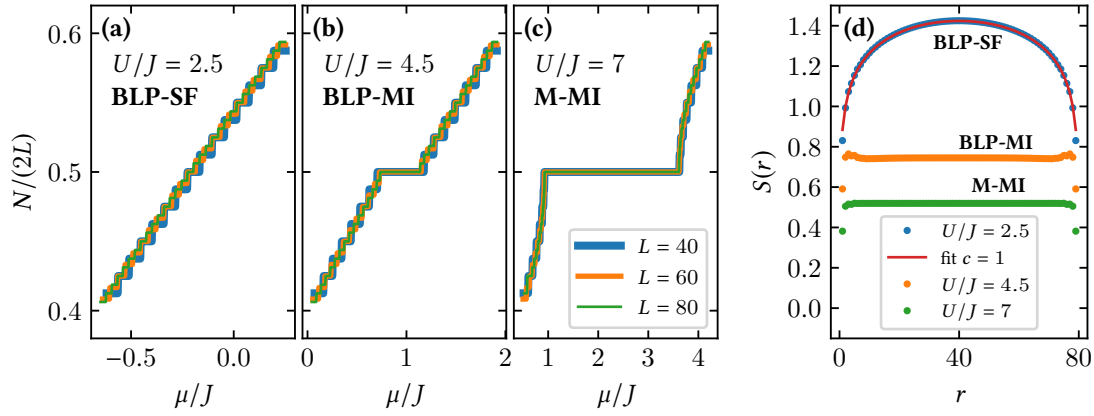


**Figure 4.2: Mott plateaus and entanglement spectra.** Particle number  $N$  in the grand-canonical ground state versus chemical potential  $\mu$  and entanglement spectra, for  $J_{\perp}/J = 0.3$ , different values of  $U_0 = U_1 = V = U$ , and a magnetic flux  $\phi/(2\pi) = 1064/769$ . The interaction strength  $U/J = 2.5$  corresponds to the superfluid biased-ladder phase (BLP-SF),  $U/J = 4.5$  corresponds to the Mott-insulating biased-ladder phase (BLP-MI), and  $U/J = 7$  corresponds to the Mott-insulating Meissner phase (M-MI). (a)  $N$  versus  $\mu$ ,  $U/J = 2.5$ , BLP-SF. Note that data corresponding to ladders with  $L = 40$ ,  $60$ , and  $80$  rungs are on top of each other. (b)  $U/J = 4.5$ , BLP-MI. (c)  $U/J = 7$ , M-MI. The plateaus in (b) and (c) indicate the appearance of Mott-insulators at filling  $\nu = 1/2$ ; see also Fig. 4.1. (d) Entanglement entropy  $S(r)$  obtained for bipartitions corresponding to cuts between rung  $(r - 1)$  and rung  $r$  for  $U/J = 2.5$  (BLP-SF,  $c = 1$ ),  $U/J = 4.5$  (BLP-MI,  $c = 0$ ), and  $U/J = 7$  (M-MI,  $c = 1$ ); considering a particle filling  $\nu = 1/2$ . The red line is obtained by fitting the offset parameter  $g$  in Eq. (4.5) to the  $U/J = 2.5$  data, considering  $c = 1$ .

of  $\bar{n}_0(k)$  and  $\bar{n}_1(k)$  differ by two orders of magnitude. Also,  $\bar{n}_1(k)$  is sharply peaked around zero quasimomentum. Figure 4.3(c) focuses on the Mott-insulating Meissner phase and shows  $\bar{n}_l(k)$  as obtained for  $J_{\perp}/J = 0.6$  and  $U/J = 6$ . Note that in the Meissner phase, the leg-resolved momentum-distribution functions fulfill the symmetry relation  $\bar{n}_0(k) = \bar{n}_1(-k)$ . Moreover, both momentum-distribution functions,  $\bar{n}_0(k)$  and  $\bar{n}_1(k)$ , exhibit peaks in the immediate proximity to  $k = 0$ . Note that the current patterns and density profiles for the parameters considered in Fig. 4.3 are presented in Fig. 4.1(b) and Fig. 4.1(c).

### Tuning the rung hopping strength

Next, we concentrate on a horizontal cut through the phase diagram introduced in Fig. 4.1 at  $U/J = 4.5$  and elucidate the biased-ladder-Mott-insulator-to-Mott-insulating

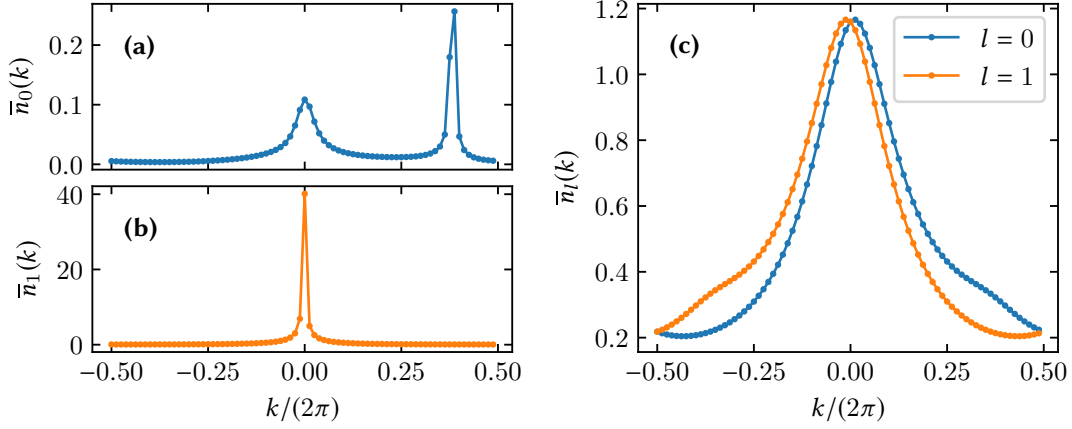


**Figure 4.3: Leg-resolved momentum-distribution functions.** Considering a particle filling  $\nu = 1/2$ , a magnetic flux  $\phi/(2\pi) = 1064/769$ , and  $L = 80$  rungs. The panels (a) and (b) show leg-resolved momentum-distribution functions  $\bar{n}_l(k)$  for the  $l = 0$  and  $l = 1$  leg, respectively, considering  $J_{\perp}/J = 0.3$  and  $U = U_0 = U_1 = V = 2.5J$ , corresponding to the biased-ladder superfluid phase. (c)  $J_{\perp}/J = 0.6$  and  $U = U_0 = U_1 = V = 6J$ , Mott-insulating Meissner phase. Note that in the Meissner phase one finds  $\bar{n}_0(k) = \bar{n}_1(-k)$ , which does not apply to the biased-ladder phase. The current patterns and density profiles for the parameters considered in this figure are shown in Fig. 4.1(b) and Fig. 4.1(c).

Meissner phase transition in Fig. 4.4. Figure 4.4(a) shows the ground-state leg-population imbalance  $\Delta_l$  as a function of  $J_{\perp}$  for systems with  $L = 40, 60$ , and  $80$  rungs. The difference between the  $L = 60$  and  $L = 80$  data is almost negligible on the scale of the figure and the abrupt change of  $\Delta_l$  clearly reveals the locus of the phase transition, which is also indicated by the vertical gray line. The half-cut entanglement entropy  $S(L/2)$ , which corresponds to a bipartition between the two most central rungs of the ladder, indicates the biased-ladder to Meissner phase transition; see Fig. 4.4(b). It is recalled that the chiral current  $j_c$  measures the global particle transport along the legs of the ladder in opposite directions, as defined in the context of Eq. (2.17). Within the considered region  $J_{\perp}/J \in [0.2, 0.6]$ ,  $j_c$  increases monotonically with the interleg coupling strength  $J_{\perp}$ , which can also be seen in Fig. 4.4(c). However, a kink in  $j_c$  marks the point of the biased-ladder-to-Meissner phase transition, which is evident in the derivative  $\partial_{J_{\perp}} j_c$  shown in Fig. 4.4(c).

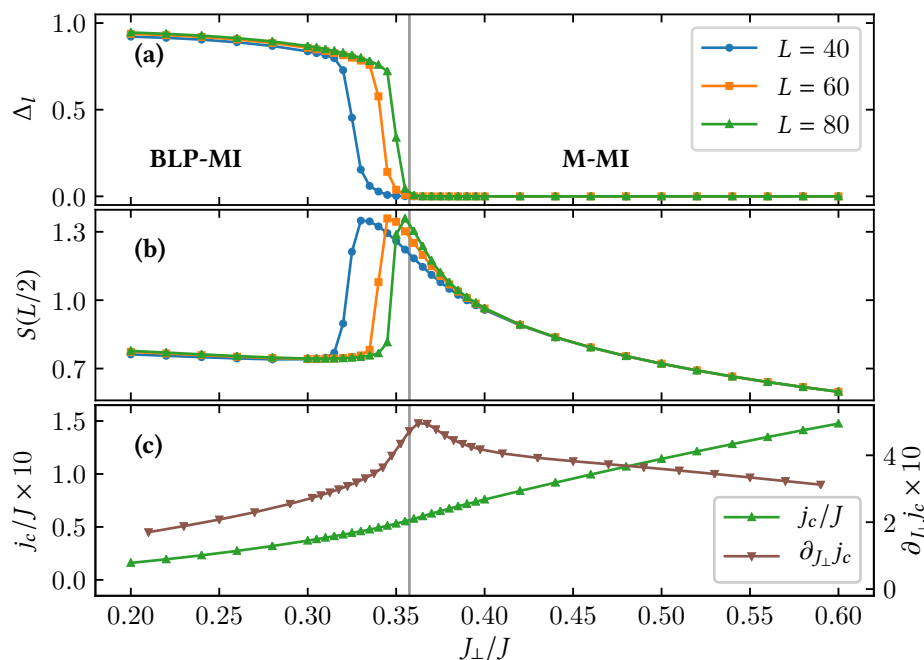


**Figure 4.4: Biased-ladder Mott insulator (BLP-MI) and Mott-insulating Meissner phase (M-MI).** Considering a particle filling  $\nu = 1/2$ ,  $SU(2)$  symmetric interactions  $U_0 = U_1 = V = 4.5J$ , and a magnetic flux  $\phi/(2\pi) = 1064/769$ . (a) Leg-population imbalance  $\Delta_l$  versus  $J_\perp$  for  $L = 40, 60$ , and  $80$  rungs. (b) Entanglement entropy  $S(L/2)$  for a bipartition corresponding to a cut between the two most central rungs of the ladder. Note that the legend from panel (a) also applies to panel (b). (c) Chiral current  $j_c$  and slope of the chiral current  $\partial_{J_\perp} j_c$  versus  $J_\perp$  for  $L = 80$  rungs.

### Tuning the interparticle interaction strength

Figure 4.5 focuses on a vertical cut through the phase diagram presented in Fig. 4.1 at  $J_\perp/J = 0.3$ . The abrupt change of the population imbalance  $\Delta_l$  when increasing  $U$  above approximately  $5J$ , shown in Fig. 4.5(a), pinpoints the transition from the Mott-insulating biased-ladder phase to the Mott-insulating Meissner phase. Note that finite-size effects in the population imbalance for systems with more than  $L = 60$  rungs are negligible on the scale of the figure. Most interestingly, the system undergoes a superfluid-to-Mott-insulator transition within the biased-ladder region when increasing  $U$  above approximately  $3.2J$ . This is revealed by the opening of a charge gap  $\Delta\mu$ , as shown in Fig. 4.5(b). In particular, in Fig. 4.5(b), we plot  $\Delta\mu$  for systems with  $L = 40, 60$ , and  $80$  rungs (colored lines) as well as  $\lim_{L \rightarrow \infty} \Delta\mu$  (black line), which has been obtained using a linear extrapolation of the finite-size data in  $(1/L)$ , as discussed above. The inset Fig. 4.5(c) shows the extrapolated charge gap  $\lim_{L \rightarrow \infty} \Delta\mu$  for  $U/J \in [2, 10]$ .

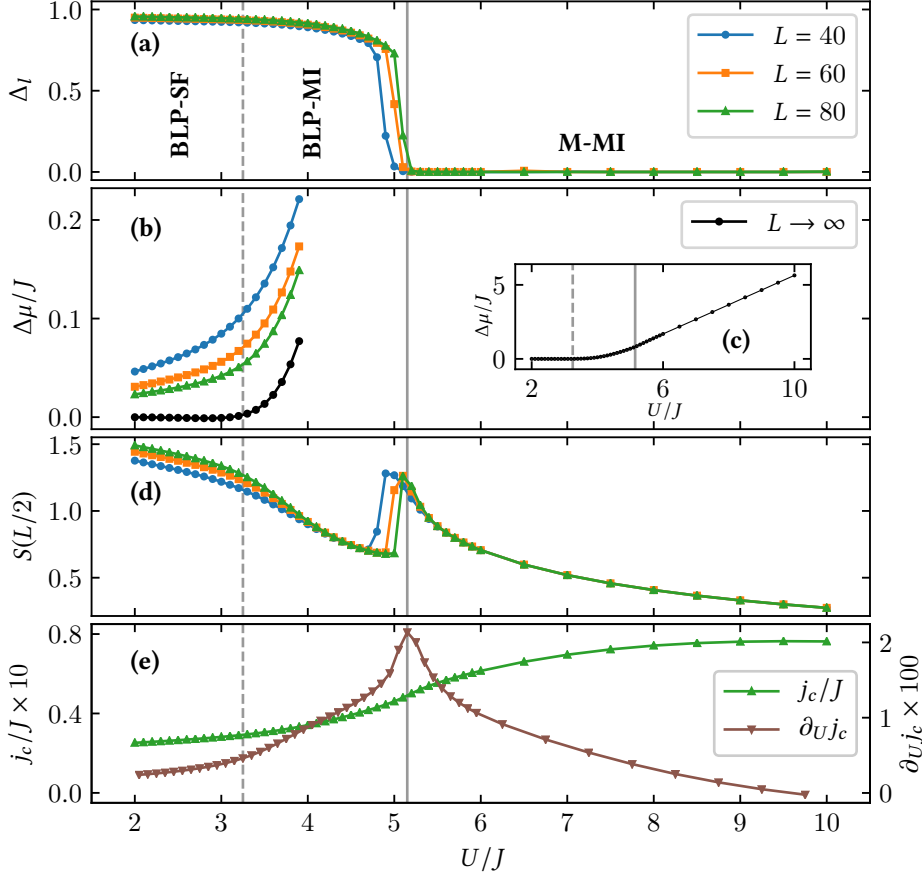


**Figure 4.5: Biased-ladder superfluid phase (BLP-SF), biased-ladder Mott insulator (BLP-MI), and Mott-insulating Meissner phase (M-MI).** Considering a particle filling  $\nu = 1/2$ ,  $SU(2)$  symmetric interactions  $U = U_0 = U_1 = V$ , a rung-hopping  $J_{\perp}/J = 0.3$ , and a magnetic flux  $\phi/(2\pi) = 1064/769$ . (a) Leg-population imbalance  $\Delta_l$  versus  $U$  for  $L = 40, 60$ , and  $80$  rungs. The vertical gray lines indicate the estimated locus of the quantum phase transitions. (b) Charge gap  $\Delta\mu$  versus  $U$ . The black solid line shows the extrapolated value of  $\Delta\mu$  in the thermodynamic limit,  $\lim_{L \rightarrow \infty} \Delta\mu$ . The inset (c) shows the charge gap in the thermodynamic limit for  $U/J \in [2, 10]$ . (d) Entanglement entropy  $S(L/2)$  for a bipartition corresponding to a cut between the two most central rungs of the ladder. Note that the legend from panel (a) also applies to panel (b) and (d). (e) Chiral current  $j_c$  and slope of the chiral current  $\partial_U j_c$  versus  $U$  for  $L = 80$  rungs.

The half-cut entanglement entropy  $S(L/2)$  shown in Fig. 4.5(d) exhibits a discontinuity at the transition from the Mott-insulating biased-ladder phase to the Mott-insulating Meissner phase. Moreover,  $S(L/2)$  is independent of the system size  $L$  in the Mott-insulating phases, while it shows a dependence on  $L$  in the superfluid biased-ladder phase [186, 224]. The chiral current  $j_c$  is shown in Fig. 4.5(e) as a function of  $U$ . In analogy to results presented in Fig. 4.4(c), a maximum in its slope  $\partial_U j_c$  indicates the biased-ladder to Meissner phase transition. Note that the vertical gray lines show the estimated points of the quantum-phase transitions.

### Effect of an additional trapping potential

In the experimental implementation of the flux-ladder model proposed in Ch. 4.1, the atoms are captured by a harmonic trapping potential. Hence, in Fig. 4.6 we show particle-density and leg-current profiles for ground states of the flux-ladder Hamiltonian (4.1) in the presence of an additional quadratic potential given by

$$V_t = \mu_t \sum_{l=0}^1 \sum_{r=0}^{L-1} \frac{(r - (L-1)/2)^2}{((L-1)/2)^2} n_{r,l}. \quad (4.6)$$

Concretely, we consider a ladder with  $L = 160$  rungs,  $N = 40$  bosons, and  $\mu_t/J = 60$ . Due to the effect of the quadratic potential, the particles localize in the center of the system. For  $U/J = 6$  and  $J_\perp/J = 0.6$ , one finds a Mott region in the central one-quarter of the ladder with a homogeneous particle density  $\langle n_{r,l} \rangle = 0.5$  and homogeneous leg currents  $j_{r,l}^\parallel$ , as can be seen by the triangle symbols in Fig. 4.6(a) and Fig. 4.6(b). It is worth noting that in the absence of the trapping potential and for a particle filling  $\nu = 1/2$ , the considered values of  $J_\perp$  and  $U$  correspond to the Mott-insulating Meissner phase. Also, Fig. 4.6(b) shows that the local leg currents in the Mott region are in accordance with the leg currents observed in the absence of a trapping potential for  $\nu = 1/2$ , which are indicated by the dashed lines. For  $U/J = 2.5$  and  $J_\perp/J = 0.3$ , one observes a finite population imbalance in the center of the system, where the particles accumulate, see Fig. 4.6(c). This is in accordance with the superfluid biased-ladder phase, which is found for the considered values of  $J_\perp$  and  $U$  in the absence of a trapping potential and for a particle filling  $\nu = 1/2$ . Figure 4.6(d) shows that for  $U/J = 2.5$  and  $J_\perp/J = 0.3$ , one finds symmetric Meissner-like leg currents in the center of the system. The leg currents observed in the superfluid biased-ladder ground state at  $\nu = 1/2$  and in the absence of a trapping potential are indicated by the dashed lines and shown for comparison. We conclude that the relevant ground-state phases can be observed in the presence of a strong trapping potential.

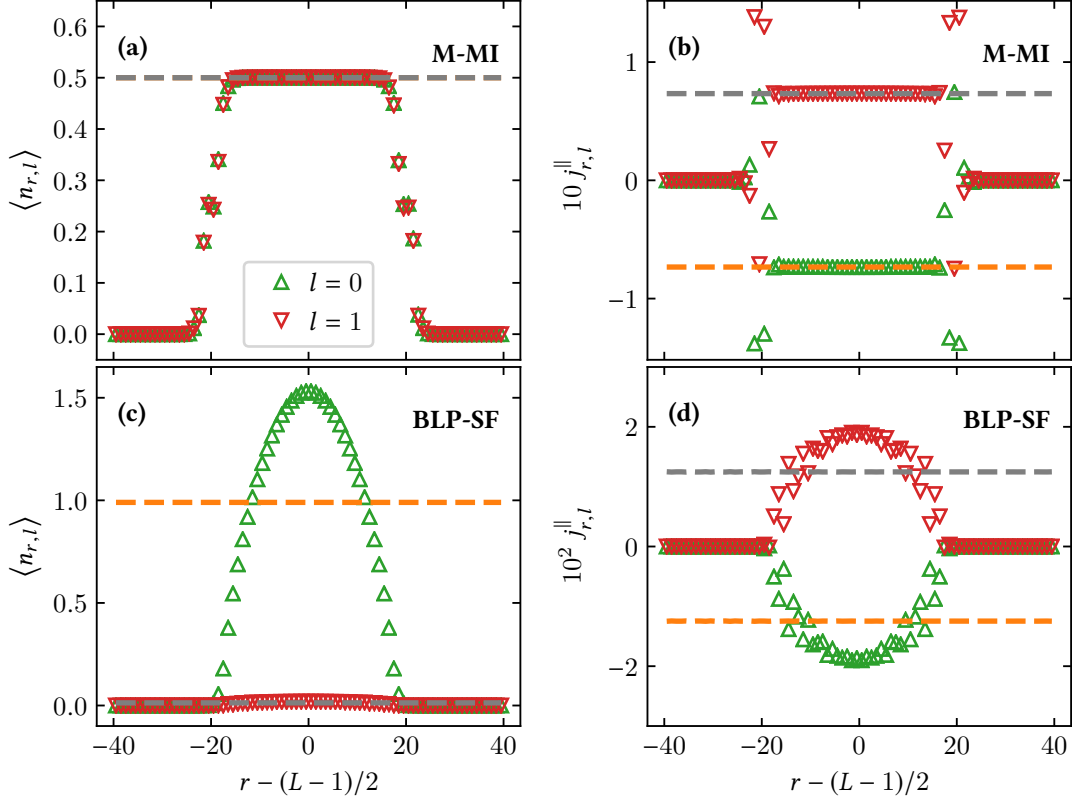


**Figure 4.6: Effect of a quadratic trapping potential.** The figure shows ground-state particle-density profiles  $\langle n_{r,l} \rangle$  [(a), (c)] and local leg currents  $j_{r,l}^{\parallel}$  [(b), (d)] in the central one-half of the ladder. We consider a harmonic trapping potential as given in Eq. (4.6) with  $\mu_t/J = 60$ ,  $L = 160$ ,  $N = 40$  bosons, and  $U = U_0 = U_1 = V$ . (a) and (b) are for  $U/J = 6$  and  $J_{\perp}/J = 0.6$ , which corresponds to the Mott-insulating Meissner phase (M-MI) in the absence of the trapping potential and for a particle filling  $\nu = 1/2$ ; see Fig. 4.1. (c) and (d) are for  $U/J = 2.5$  and  $J_{\perp}/J = 0.3$ , corresponding to the superfluid biased-ladder phase (BLP-SF). In all panels, the green upper triangles and the red lower triangles are for the  $l = 0$  leg and the  $l = 1$  leg, respectively. The dashed orange ( $l = 0$ ) and gray ( $l = 1$ ) lines show results in the absence of the harmonic potential and for a particle filling  $\nu = 1/2$ . Note that in panel (a), the data for  $l = 0$  and  $l = 1$  are on top of each other.

### Numerical approach

Here, we briefly comment on the numerical simulations which were employed in order to obtain the results presented in Sec. 4.2, acknowledging that they were performed using the SyTen toolkit [245, 249].

For all of the results presented in Sec. 4.2, the U(1) symmetry associated with the particle-number conservation of the flux-ladder Hamiltonian (2.1) was exploited on the level of the matrix-product states. In particular, for the calculation of ground states, we employed the single-site variant of the density-matrix renormalization-group method [32, 34, 35], using subspace expansion [250]. Convergence of the variationally optimized states was ensured by comparing energy expectation values  $\langle H \rangle$ , variances  $\langle H^2 \rangle - \langle H \rangle^2$ , as well as all relevant observables, for different values of the site-local bosonic cutoff and for different bond dimensions up to typically 3000. It is worth noting that for the Hamiltonian model parameters considered in Sec. 4.2, a truncation at at most six bosons per lattice site is sufficient.

### 4.3 Quench dynamics

Preparing the flux-ladder system close to its ground state experimentally can be notoriously difficult. Therefore, it is highly desirable to develop practical schemes to explore the various phases existing in the interacting flux-ladder model [186]. This is underlined by recent experimental advances in noninteracting ladders, where elaborate loading procedures enabled the observation of chiral edge states [139, 140] and the estimation of Chern numbers [149, 174].

Here, we present feasible quench protocols which might allow one to probe the chiral current in the interacting Meissner phase and to detect signatures of an underlying biased-ladder phase in the transient dynamics of the leg-population imbalance. In Sec. 4.3.1, our focus is on the chiral current in the Meissner phase. There, we study the instantaneous turning on of leg hopping in the synthetic flux-ladder model, considering a rung-localized initial state, which is here denoted by  $|R\rangle$ . Explicitly, for a vanishing leg hopping,  $J = 0$ ,  $|R\rangle$  is the one-particle-per-rung ground state of the Hamiltonian  $H$  introduced in Eq. (2.1). It is sketched in Fig. 4.7 and given by

$$|R\rangle = \frac{1}{2^{L/2}} \prod_{r=0}^{L-1} \left( e^{-ir\phi/2} a_{r,0}^\dagger + e^{ir\phi/2} a_{r,1}^\dagger \right) |\text{vac}\rangle, \quad (4.7)$$

where  $|\text{vac}\rangle$  denotes the vacuum state with zero particles,  $N = 0$ . In Sec. 4.3.2, we concentrate on the leg-population imbalance and investigate the instantaneous turning



**Figure 4.7: Sketch of the initial states considered in quantum quenches.**  $|R\rangle$  represents the one-particle-per-rung ground state of the ladder Hamiltonian  $H$ , introduced in Eq. (2.1), for vanishing leg hopping,  $J = 0$ . Note that each rung is occupied by exactly one particle.  $|L\rangle$  represents the  $L$ -particles-on-one-leg ground state of  $H$  for vanishing rung hopping,  $J_{\perp} = 0$ .

on of interleg hopping considering a leg-localized initial state  $|L\rangle$ . Here,  $|L\rangle$  represents the  $L$ -particles-on-one-leg ground state of  $H$ , as obtained for vanishing interleg hopping,  $J_{\perp} = 0$ . We stress that both initial states are experimentally accessible and the considered quench schemes are realistic in current quantum-gas platforms, as discussed in Sec. 4.1.

### 4.3.1 Probing the chiral current

Let us start with the presentation of quench results in the presence of site-local interactions but without rungwise interactions,  $U_0 = U_1 = U$  and  $V = 0$ . Figure 4.8(a) shows the transient dynamics in the chiral current  $j_c$ , which are induced by the instantaneous turning on of leg hopping in the rung-localized initial state  $|R\rangle$ . Explicitly, time evolutions of  $j_c$  are shown for hard-core bosons (HCB), considering  $J_{\perp}/J = 4, 3, 2$ , as well as for finite interaction strengths,  $U/J = 20$  and  $U/J = 10$ , considering  $J_{\perp}/J = 4$ . For the purpose of a clear presentation, the data corresponding to different values of  $U$  and  $J_{\perp}$  are vertically offset by  $m \times 0.25$ , with  $m = 0, 1, 2, 3, 4$ . In order to neglect boundary effects,  $j_c$  is computed in the central one-third of the ladder. A comparison of the  $L = 61$  data (solid colored lines) and the  $L = 41$  data (black dotted lines) reveals that finite-size effects are negligible within the considered time interval  $tJ \in [0, 10]$ . Most interestingly, Fig. 4.8(a) shows that after the instantaneous turning on of leg hopping,  $j_c$  oscillates around a finite value. The colored filled symbols represent the time averages of  $j_c$ , which are computed in the interval  $tJ \in [4, 10]$ . Remarkably, for strong interactions, these time averages exhibit a very similar dependence on the model parameters as  $j_c$  in the ground state of the post-quench Hamiltonian, which is indicated by the black empty symbols. Figure 4.8(b) gives an overview of the  $J_{\perp}$ -dependence of the chiral

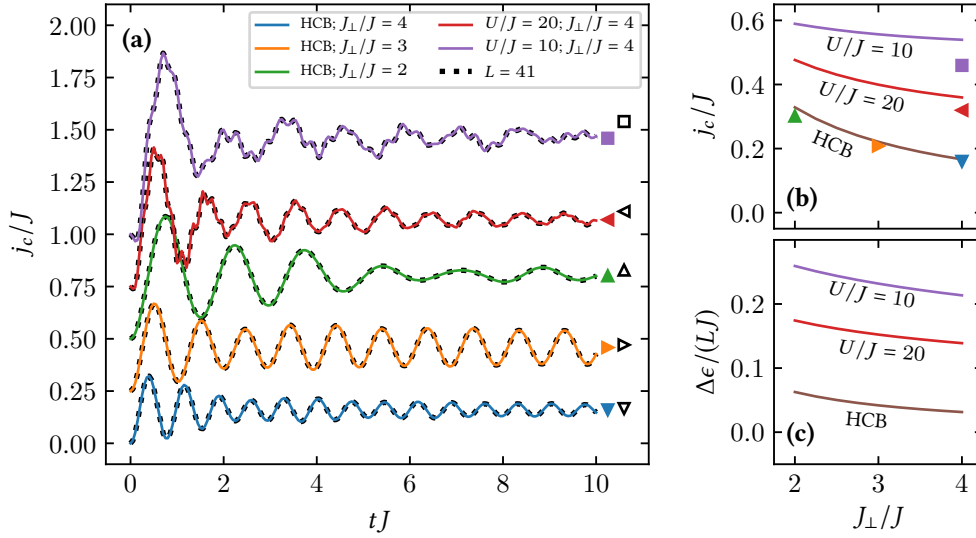


**Figure 4.8: Transient dynamics in the chiral current and quench energy after the instantaneous turning on of leg hopping.** Considering the initial state  $|R\rangle$  (introduced in the context of Fig. 4.7), symmetric on-site interactions  $U_0 = U_1 = U$ , vanishing rungwise interactions  $V = 0$ ,  $L = 61$  rungs, and a magnetic flux  $\phi/(2\pi) = 1064/769$ . (a) Chiral current  $j_c$  versus time after quench  $t$ . HCB refers to hard-core bosons and the data corresponding to different parameters ( $J_\perp$  and  $U$ ) are vertically offset by 0.25, 0.5, 0.75, and 1, for the purpose of a clear presentation. The black dotted lines are for  $L = 41$  rungs, showing the negligible role of finite-size effects. In order to neglect boundary effects,  $j_c$  is computed in the central one-third of the ladder. Colored filled symbols show the time-averaged value of  $j_c$  for  $tJ \in [4, 10]$ . Black empty symbols show  $j_c$  in the ground state of the post-quench Hamiltonian. (b) Overview of the  $J_\perp$ -dependence of  $j_c$  in the ground state of the post-quench Hamiltonian (colored solid lines). Colored symbols depict the time-averaged values of  $j_c$ , which are also shown in (a). (c) Quench energy  $\Delta\epsilon$  versus  $J_\perp$ .

current  $j_c$  in the ground state for  $U/J = 10, 20$  and hard-core bosons, including the time averages from Fig. 4.8(a). For  $U/J = 10$ ,  $U/J = 20$ , and for hard-core bosons, the vortex-to-Meissner transition appears for values of  $J_\perp/J < 2$  [184]. Thus, all of the parameters considered in Fig. 4.8 correspond to the Meissner phase.

The quench energy  $\Delta\epsilon$  measures the difference between the energy in the flux ladder after turning on the hopping elements and the ground-state energy of the post-quench Hamiltonian  $H$  introduced in Eq. (2.1). Explicitly, it is given by

$$\Delta\epsilon = \langle \psi | H | \psi \rangle - \epsilon, \quad (4.8)$$

where  $\epsilon$  is the ground-state energy and  $|\psi\rangle = |R\rangle, |L\rangle$  is the considered initial state. Figure 4.8(c) elucidates that  $\Delta\epsilon$  decreases with increasing interaction strength and increasing interleg coupling strength  $J_\perp$ . This is in accordance with our observation that the quench protocol discussed here reproduces the chiral current in the ground state especially well in the strongly-interacting and large- $J_\perp$  regime, which is deep in the Meissner phase. Lastly, we note that even though the case of vanishing rungwise interactions ( $V = 0$ ) is not particularly relevant in synthetic dimension implementations, it is still of general interest as it represents a variant of the flux-ladder model which has been extensively studied in previous works; see, for instance, Refs. [179, 184, 186].

Next, we concentrate on  $SU(2)$  symmetric interactions, which are especially relevant in ladders realized by means of a synthetic dimension, such as the  $^{41}\text{K}$  system discussed in Sec. 4.1. In Fig. 4.9, we consider the instantaneous turning on of leg hopping for  $U_0 = U_1 = V = 8J$  in a system with  $L = 61$  rungs and for model parameters corresponding to the Meissner phase. Figure 4.9(a) shows the transient dynamics in the chiral current  $j_c$ , which are computed in the central one-third of the ladder, for different values of the interleg coupling strength  $J_\perp/J = 3, 6, 12, 30$  (solid colored lines). In analogy to Fig. 4.8, it can be seen that after an initial transient regime up to time  $tJ \approx 3$ ,  $j_c$  oscillates around a finite value. Moreover, the black dashed lines, which are for  $L = 41$  and on top of the  $L = 61$  results, suggest a negligible influence of boundary effects for  $tJ \in [0, 6]$ . We emphasize that the time-averaged values of  $j_c$  in the interval  $tJ \in [3, 6]$  provide a good estimate for the chiral current in the ground state of the post-quench Hamiltonian, capturing the  $J_\perp$ -dependence of the latter. This is also shown in Fig. 4.9(b) for various values of  $J_\perp/J \in [3, 30]$ , where the solid black line corresponds to the ground state and the gray symbols depict the time averages. Note that time-averaged chiral currents for which the transient dynamics are shown in Fig. 4.9(a) are highlighted by the corresponding colors in Fig. 4.9(b). Additionally, Fig. 4.9(c) reveals that the quench energy  $\Delta\epsilon$  decreases with increasing  $J_\perp$ , suggesting that the quench protocol is especially useful in the regime of strongly coupled legs, which is deep in the Meissner phase. Finally, we conclude that after the instantaneous turning on of leg hopping in the Meissner phase, the chiral current in the short-time dynamics exhibits a similar dependence on  $J_\perp$  as the chiral current in the corresponding ground state.

### 4.3.2 Signatures of the biased-ladder phase

In Fig. 4.10, we focus on the instantaneous turning on of rung hopping in the leg-localized initial state  $|L\rangle$ . It is shown that signatures of an underlying biased-ladder phase of the post-quench Hamiltonian can be observed in the transient dynamics of

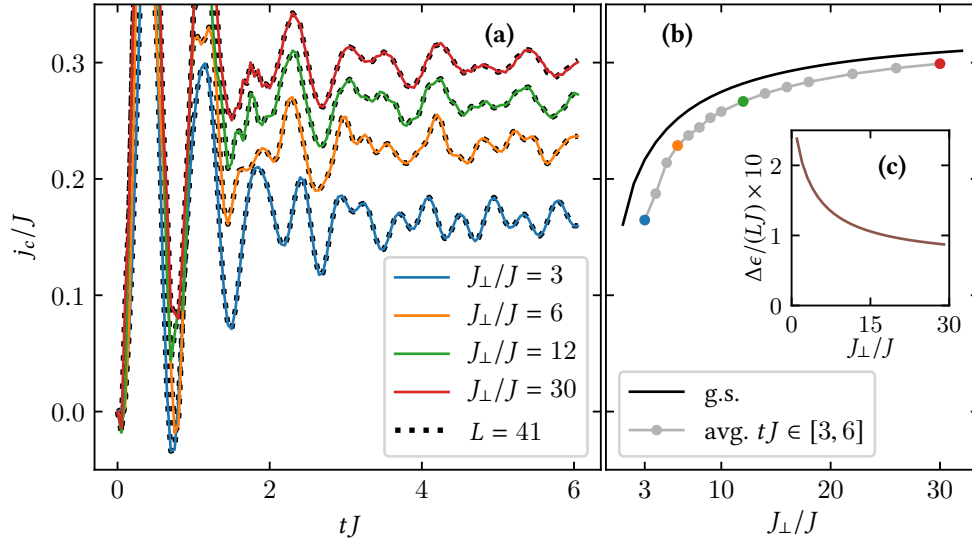


**Figure 4.9: Transient dynamics in the chiral current and quench energy for SU(2) symmetric interparticle interactions.** Considering the instantaneous turning on of leg hopping in the initial state  $|R\rangle$  (introduced in the context of Fig. 4.7), for various values of the interleg hopping strength  $J_\perp$ , SU(2) symmetric interactions  $U_0 = U_1 = V = 8J$ ,  $L = 61$  rungs, and a magnetic flux  $\phi/(2\pi) = 1064/769$ . (a) Chiral current  $j_c$  versus time after quench  $t$  for  $J_\perp/J = 3, 6, 12, 30$ . The black dotted lines are for  $L = 41$  rungs, showing the negligible role of finite-size effects. (b) The black solid line depicts  $j_c$  versus  $J_\perp$  in the ground state of the post-quench Hamiltonian. Gray symbols indicate the time-averaged values of  $j_c$  considering the time interval  $tJ \in [5, 10]$ . Note that the values of  $j_c$  for which the transient dynamics are shown in panel (a) are highlighted by the corresponding colors. The inset (c) shows the quench energy  $\Delta\epsilon$  versus  $J_\perp$ . In order to neglect boundary effects,  $j_c$  is computed in the central one-third of the ladder.

the density imbalance between the legs of the ladder. Here, the considered model parameters are  $U_0 = U_1 = V = 3.5J$  and  $J_\perp/J \in [0.3, 0.7]$ . We stress that for  $J_\perp/J < 0.5$ , the ground state of the post-quench Hamiltonian is in the biased-ladder phase, while  $J_\perp/J > 0.5$  corresponds to the Meissner phase; see Fig. 4.1 for the corresponding phase diagram. Figure 4.10(a) shows the average particle number  $N_0/L$  in the  $l = 0$  leg versus the time after the quench  $t$ . Most interestingly, for parameters which clearly correspond to the biased-ladder phase, namely  $J_\perp/J = 0.3$ ,  $J_\perp/J = 0.35$ , and  $J_\perp/J = 0.4$ , a very stable density imbalance is maintained throughout the considered time interval  $tJ \in [0, 40]$ . On the other hand, for the parameters corresponding to the Meissner phase,  $J_\perp/J = 0.60$ ,  $J_\perp/J = 0.65$ , and  $J_\perp/J = 0.70$ ,  $N_0$  quickly starts to decay and to oscillate around  $L/2$ , which corresponds to a vanishing leg-population imbalance characteristic of the Meissner phase. For values of  $J_\perp$  which are in the immediate proximity to

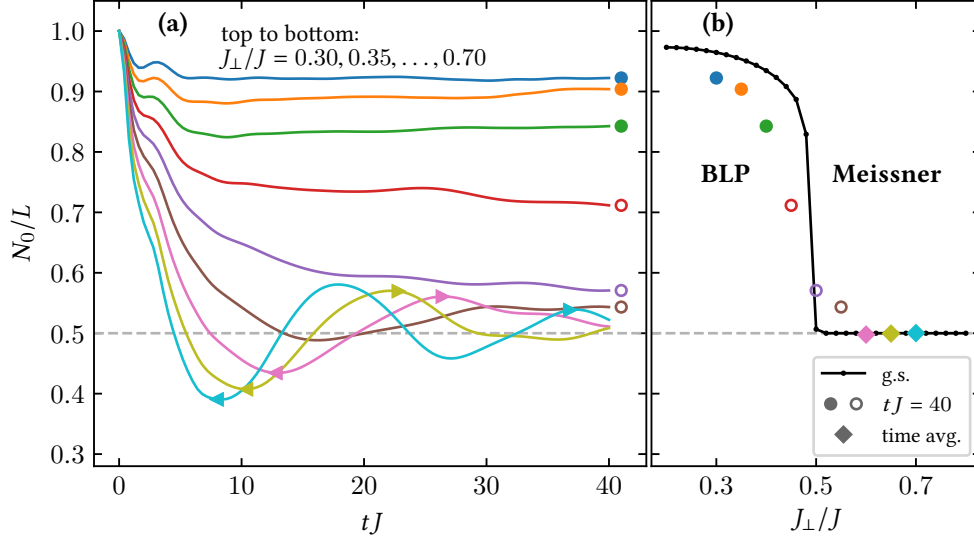


**Figure 4.10: Transient dynamics in the leg-population imbalance after the instantaneous turning on of interleg hopping.** Considering the initial state  $|L\rangle$  (introduced in the context of Fig. 4.7),  $SU(2)$  symmetric interactions  $U_0 = U_1 = V = 3.5J$ ,  $L = 61$ , and  $J_\perp/J \in [0.3, 0.7]$ . (a) Particle number  $N_0/L$  in the  $l = 0$  leg versus time after quench  $t$ . The gray dashed line indicates a vanishing leg-population imbalance, corresponding to  $N_0/L = 0.5$  (note that there is a total number of  $N = L$  particles). For values of  $J_\perp$  that show oscillations of  $N_0$  in  $tJ \in [0, 40]$ , left and right triangles indicate the time intervals for which the time-averaged data (diamonds) shown in (b) are computed. Concerning parameters, for which  $N_0$  does not show clear oscillations in the considered time interval, we consider the values attained at  $tJ = 40$  (filled and empty circles). (b)  $N_0/L$  versus  $J_\perp$  in the ground state of the post-quench Hamiltonian (black line), indicating the biased-ladder phase (BLP) and the Meissner phase. Symbols depict the time-averaged values of  $N_0$  (diamonds) or  $N_0$  at  $tJ = 40$  (filled and empty circles).

the biased-ladder-to-Meissner phase transition, namely  $J_\perp/J = 0.45$ ,  $J_\perp/J = 0.5$ , and  $J_\perp/J = 0.55$ ,  $N_0$  does not exhibit decaying oscillations in the considered time interval  $tJ \in [0, 40]$  but suggests a possible decay towards  $L/2$  on an intermediate time scale. Figure 4.10(b) shows  $N_0$  in the ground state of the post-quench Hamiltonian (black line), which unambiguously indicates the biased-ladder phase for  $J_\perp/J < 0.5$ . The diamond-shaped symbols depict time-averages of  $N_0$ , considering intervals as indicated by the left and right triangles in Fig. 4.10(a). They reveal that for model parameters corresponding to the Meissner phase, the density imbalance between the legs quickly vanishes after the turning on of interleg hopping. However, for values of  $J_\perp$  corresponding to the biased-ladder phase, the values of  $N_0$  attained at  $tJ = 40$ , which are indicated by the filled circles, reveal a finite density imbalance between the legs. Moreover, there is

a dependence on the interleg hopping strength  $J_{\perp}$  that is in accordance with the one of the ground state in the post-quench Hamiltonian. Similarly, for values of  $J_{\perp}$  in the immediate proximity to the biased-ladder-to-Meissner phase transition, the values of  $N_0$  attained at  $tJ = 40$  are indicated by the empty circles. We conclude that the underlying biased-ladder phase leaves signatures in the short-time dynamics following the instantaneous turning on of interleg hopping in the leg-localized initial state  $|L\rangle$ .

### Numerical approach

At this point, we note that the quench dynamics presented in Sec. 4.3 were simulated using the two-site variant of the time-dependent variational principle algorithm [36, 284], as implemented in the SyTen toolkit [245, 249]. We typically employed bond dimensions up to 500 and the convergence of all relevant observables was ensured by increasing the bond dimension and decreasing the size of the time steps independently. In both quench scenarios, corresponding to the different initial states  $|R\rangle$  and  $|L\rangle$ , the conservation of the particle number  $N = L$  was enforced on the level of the matrix-product states during the time-dependent simulations.

## 4.4 Summary

In Ch. 4, we studied the ground-state phases and quench dynamics in an interacting synthetic flux-ladder model. The focus was on model parameters and specifics that are realistic in a  $^{41}\text{K}$  setup which exploits two internal atomic states as a synthetic dimension. Explicitly, we concentrated on rungwise  $\text{SU}(2)$  symmetric interactions  $U_0 = U_1 = V = U$ , a particle filling of one boson per rung  $\nu = 1/2$ , and a value of the magnetic flux  $\phi/(2\pi) = 1064/769$ .

Employing extensive density-matrix renormalization-group method simulations, we mapped out the ground-state phase diagram of the synthetic flux-ladder model as a function of the interaction strength  $U$  and the interleg hopping strength  $J_{\perp}$ . For large values of  $U$  and  $J_{\perp}$ , the model is typically found to be in a Meissner phase. Moreover, for intermediate values of  $U$  and  $J_{\perp}$ , the model hosts biased-ladder phases, which are typically stabilized by the presence of rungwise interactions and can exist on top of superfluids as well as Mott insulators.

By time evolving matrix-product states, we studied how the chiral current  $j_c$  and the leg-population imbalance  $\Delta_l$ , which are key observables in the Meissner phase and in the biased-ladder phase, can be probed in feasible quantum-quench protocols. In particular, for the Meissner phase, the instantaneous turning on of leg hopping  $J$  in

the rung-localized initial state  $|R\rangle$  induces a transient chiral current. Interestingly, this current exhibits a similar dependence on the model parameters as the chiral current in the ground state of the corresponding post-quench Hamiltonian. We showed that this protocol is especially promising for large values of the interparticle interaction strength  $U$  and the interleg hopping strength  $J_{\perp}$ , which is deep in the Meissner phase. Concentrating on the leg-population imbalance, we showed that an underlying biased-ladder phase leaves signatures in the short-time dynamics that are induced by the instantaneous turning on of the interleg hopping  $J_{\perp}$  in an accessible leg-localized initial state  $|L\rangle$ .

The results presented in this chapter were originally put forward in Ref. [2] and they might provide useful guidance to future experimental implementations of flux ladders exploiting synthetic dimensions.

## Vortex-to-Meissner crossover at finite temperatures

In this chapter, we study the effect of finite temperatures in flux ladders. Flux ladders host rich quantum-phase diagrams that have attracted great interest. However, so far, most of the work on these systems has concentrated on zero-temperature phases while the corresponding finite-temperature regime remains largely unexplored. The question if and up to which temperature characteristic features of the zero-temperature phases persist is relevant in experimental realizations. In this chapter, we concentrate on chiral currents and momentum-distribution functions, which are key observables in quantum-gas experiments. These quantities are computed for strongly interacting bosons as well as for noninteracting bosons and spinless fermions at zero and finite temperatures. For the simulation of strongly interacting bosons at finite temperatures we employ the matrix-product-state based purification approach, which was introduced in Ch. 3.

Specifically, our main results concern the vortex-liquid-to-Meissner crossover of strongly repulsive bosons. We demonstrate that signatures of the vortex-liquid phase can still be detected at elevated temperatures from characteristic finite-momentum maxima in the momentum-distribution functions, while the vortex-liquid phase leaves weaker fingerprints in the local rung currents and in the chiral current. In order to determine the range of temperatures over which these signatures can be observed, we introduce a suitable measure for the contrast of these maxima. The results are condensed into a finite-temperature crossover diagram.

This chapter is organized as follows. In Sec. 5.1, we consider the grand-canonical statistics of noninteracting bosons. Focusing on momentum-distribution functions, the presence of clearly detectable characteristics of the vortex phase at finite temperatures is examined. In Sec. 5.2, we concentrate on the grand-canonical statistics of noninteracting spinless fermions and elucidate the differences between the bosonic and fermionic vortex-to-Meissner transition. Our main results addressing the vortex-liquid-to-Meissner crossover of canonical and grand-canonical thermal states of strongly interacting bosons are presented in Sec. 5.3. Finally, we summarize our work on the effect of finite temperatures in flux ladders in Sec. 5.4.

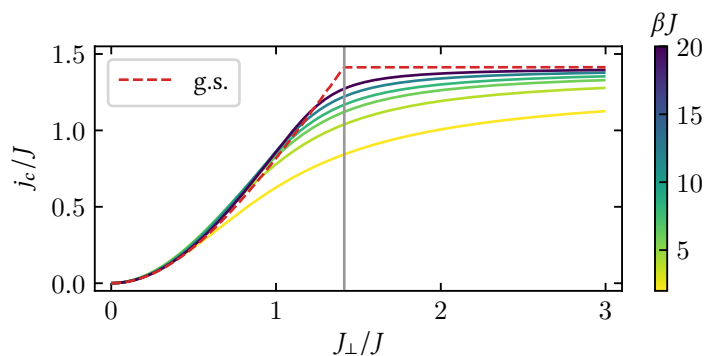


**Figure 5.1: Chiral current at zero and finite temperatures for noninteracting bosons.** Chiral current  $j_c$  as a function of the interleg coupling strength  $J_\perp$ . Considering a ladder with  $L = 128$  rungs, open boundary conditions, and a magnetic flux  $\phi = \pi/2$ . Data are shown for grand-canonical thermal states corresponding to different inverse temperatures  $\beta J = 2, 4, 6, 8, 12,$  and  $20$  (also indicated by the colorbar) and an average particle filling one-half. The chiral current corresponding to the ground state (g.s.) at particle filling  $\nu = 1/2$  is shown for comparison. The vertical gray line indicates the critical value of  $J_\perp/J$  at zero temperature.

## 5.1 Noninteracting bosons

We recap that the noninteracting bosonic flux-ladder model with periodic boundary conditions exhibits two degenerate ground states in the vortex phase, corresponding to finite characteristic momenta  $k = \pm \tilde{k}$ , as discussed in the context of Eq. (2.7) in Sec. 2.1. At the vortex-to-Meissner transition, this degeneracy is lifted and the system exhibits a unique ground state corresponding to  $k = 0$  in the Meissner phase.

### Chiral current

For flux ladders with periodic boundary conditions, the chiral current  $j_c$  corresponding to the unique bosonic ground state in the Meissner phase does not vary with increasing interleg coupling strength and shows zero fluctuations. This does not apply to the degenerate ground states found in the vortex phase. Moreover, in the vortex phase, each of the degenerate ground states exhibits a population imbalance between the legs of the ladder.

The red dashed line in Fig. 5.1 shows the chiral current  $j_c$  corresponding to the ground state of noninteracting bosons in a ladder with  $L = 128$  rungs and open boundaries at particle filling one-half,  $\nu = 1/2$ . Here, we remind that the particle filling  $\nu$  denotes the number of particles  $N$  divided by  $2L$ , which is the number of lattice sites.

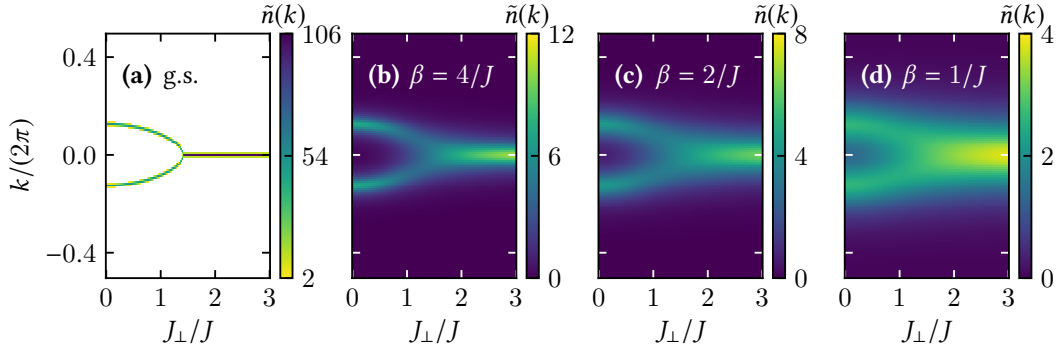


**Figure 5.2: Bosonic momentum-distribution functions at zero and finite temperatures.** Integrated leg-gauge momentum-distribution function  $\tilde{n}(k)$ , as defined in the context of Eq. (2.13), versus interleg coupling strength  $J_{\perp}$ . Considering noninteracting bosons in a ladder with  $L = 128$  rungs, open boundary conditions, and a magnetic flux  $\phi = \pi/2$ . (a) Ground-state (g.s.) momentum-distribution functions at particle filling  $\nu = 1/2$ . (b) - (d) Momentum-distribution functions computed in grand-canonical thermal states at average particle filling one-half and different inverse temperatures (b)  $\beta = 4/J$ , (c)  $\beta = 2/J$ , and (d)  $\beta = 1/J$ .

The chiral current increases gradually with increasing interleg coupling strength in the vortex phase and remains constant in the Meissner phase. A kink in the chiral current reveals the critical interleg coupling strength of the vortex-to-Meissner transition. By comparison to results obtained for larger system sizes, which are not shown here, we note that boundary and finite-size effects are negligible on the scale of the figure. Solid lines show the chiral current in grand-canonical thermal states corresponding to different inverse temperatures  $\beta J = 2, 4, 6, 8, 12$ , and  $20$ , considering an average particle filling of one boson per rung. The kink is quickly washed out and thus there is no clear signature of the crossover in the finite-temperature chiral currents. We note that the chiral current can be slightly enhanced due to the effect of finite temperatures in the vortex phase.

### Integrated leg-gauge momentum-distribution functions

Results for the integrated leg-gauge momentum-distribution function  $\tilde{n}(k)$ , as introduced in the context of Eq. (2.13), of noninteracting bosons are shown in Fig. 5.2. Here, the ground-state vortex-to-Meissner transition manifests itself in the transition from two distinct maxima at finite momenta to a single maximum at zero momentum, as shown in Fig. 5.2(a). The integrated leg-gauge momentum-distribution function calculated in grand-canonical thermal states at different temperatures  $J/4$ ,  $J/2$ , and  $J$ , which are

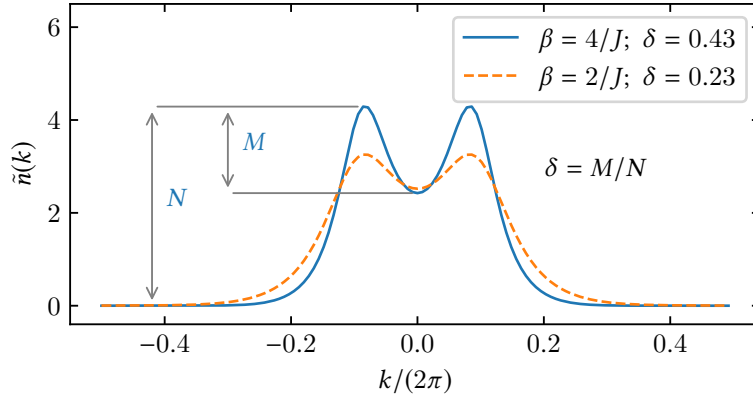


**Figure 5.3: Definition of contrast in leg-gauge momentum-distribution functions.** Considering noninteracting bosons,  $L = 128$  rungs,  $J_{\perp} = J$ , and a magnetic flux  $\phi = \pi/2$ , the figure shows grand-canonical integrated leg-gauge momentum-distribution functions  $\tilde{n}(k)$  at average particle filling one-half corresponding to inverse temperatures  $\beta = 4/J$  and  $\beta = 2/J$ . The two characteristic peaks indicating the vortex phase are more distinctive at lower temperatures. The contrast  $\delta$  as defined in Eq. (5.1) serves as an indicator for the vortex phase.

shown in Figs. 5.2(b), 5.2(c), and 5.2(d), respectively, reveal that the typical peaks persist at finite temperatures. Note that the results for ground states in Fig. 5.2(a) and for the grand-canonical thermal states in Figs. 5.2(b), 5.2(c), and 5.2(d) are for a fixed particle filling  $\nu = 1/2$  and an average filling of one particle per rung.

### Signatures of the vortex phase at finite temperatures

Next, we elucidate the finite-temperature vortex-to-Meissner crossover. Considering the integrated leg-gauge momentum-distribution function  $\tilde{n}(k)$  of thermal states, we specify at which temperatures clear characteristics of the vortex phase can be detected and where the crossover can be observed. For this purpose, we introduce a measure for the contrast of finite-momentum maxima in  $\tilde{n}(k)$  via this definition

$$\delta = \frac{\max_k (\tilde{n}(k)) - \tilde{n}(k=0)}{\max_k (\tilde{n}(k))}. \quad (5.1)$$

Thus, on the one hand, values of  $\delta$  larger than zero indicate that two characteristic peaks at finite momenta can be resolved. Hence,  $\delta > 0$  is indicative of the vortex phase. On the other hand, values of  $\delta$  equal to zero mean that  $\tilde{n}(k)$  exhibits a single maximum at zero momentum, and, due to the blurring effect of finite temperatures, it cannot be decided whether the underlying values of  $J$ ,  $J_{\perp}$ , and  $\phi$  correspond to the vortex phase or to the

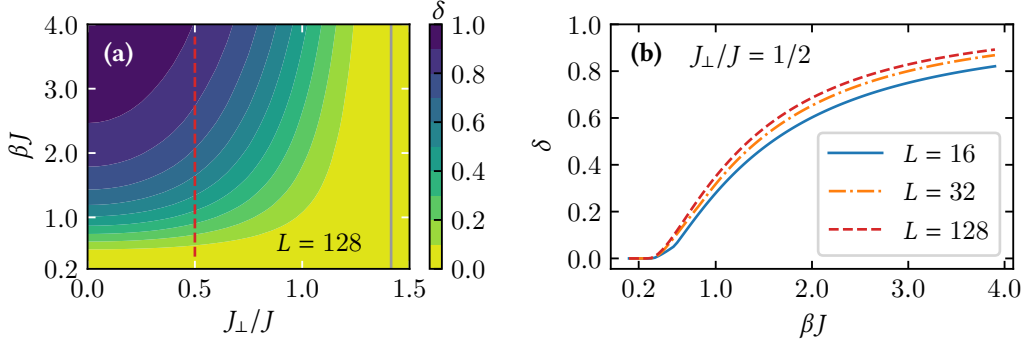


**Figure 5.4: Signatures of the vortex phase of noninteracting bosons at finite temperatures.** Considering a magnetic flux  $\phi = \pi/2$ . (a) Contrast  $\delta$  as a function of interleg coupling strength  $J_{\perp}$  and inverse temperature  $\beta$  calculated in grand-canonical thermal states with an average particle filling of one boson per rung. The solid gray line indicates the position of the zero-temperature vortex-to-Meissner transition occurring at  $J_{\perp}/J = \sqrt{2}$ . (b) Illustration of finite-size effects:  $\delta$  versus  $\beta J$  for ladders with  $L = 16$ , 32, and 128 rungs. Panel (b) is a cut through panel (a) at  $J_{\perp}/J = 1/2$ ; see the red dashed line in (a).

Meissner phase. The definition of the contrast  $\delta$ , Eq. (5.1), is illustrated in Fig. 5.3 using the abbreviations  $M = \max_k (\tilde{n}(k)) - \tilde{n}(0)$  and  $N = \max_k (\tilde{n}(k))$ . There, it is also shown that the characteristic peaks indicating the vortex phase are more distinctive at lower temperatures.

Considering grand-canonical thermal states with an average particle filling one-half, a contour plot of  $\delta$  as a function of the interleg coupling strength  $J_{\perp}$  and the inverse temperature  $\beta$  is shown in Fig. 5.4(a). It becomes apparent that the integrated leg-gauge momentum-distribution functions show clear signatures of the vortex phase at sufficiently small values of  $J_{\perp} \lesssim J$  and up to quite high temperatures  $\beta^{-1} \sim J$ . Note that the zero-temperature transition occurs at  $J_{\perp}/J = \sqrt{2}$ , as indicated in Fig. 5.4(a) by the solid gray line. The role of finite-size effects for the contrast  $\delta$  is studied in Fig. 5.4(b) by considering a cut through the graph in Fig. 5.4(a) at  $J_{\perp}/J = 1/2$ . We note that finite-size effects of  $\delta$  are overall small and, for a ladder of length  $L = 128$ , the differences to larger  $L$ , which are not shown here, are negligible on the scale of the plot. Furthermore, we only observe quantitative differences as  $L$  varies, yet the overall dependence of  $\delta$  on  $\beta$  is the same for all  $L$ .

Finally, we comment on another measure for the vortex phases that is often studied in the literature, namely the vortex density; see, for instance, Refs. [179, 184, 186]. In the study by Piraud et al. [184], the vortex density was extracted from a Fourier

transformation of the local rung-current patterns. At finite temperatures, however, the local rung currents are quickly washed out such that this approach cannot be used here. Rather, one would need to study the decay of rung-current equal-time autocorrelations. These are not easily accessible in experiments and we therefore do not further study measures for the vortex density here.

## 5.2 Noninteracting spinless fermions

In this section, we discuss chiral currents and momentum-distribution functions of noninteracting spinless fermions.

### Chiral currents

Chiral currents corresponding to the ground states of noninteracting spinless fermions behave fundamentally different from those corresponding to the ground states of noninteracting bosons. For bosons, the behavior close to the band minima is important, while for fermions the behavior close to the Fermi energy is relevant. One notable consequence is that already for  $U = 0$ , in the Meissner phase, noninteracting fermions exhibit a reversal of the direction of the chiral current with increasing filling  $\nu$  [194, 195]. Fermionic ground-state chiral currents are shown in Fig. 5.5(a) as a function of interleg coupling strength  $J_{\perp}$  for different particle fillings  $\nu$  ranging from  $1/(2L)$  to  $1/2$ . For each filling, a kink of the chiral current clearly reveals the critical value of  $J_{\perp}$  at the vortex-to-Meissner transition. Figure 5.5(b) concentrates on fermionic chiral currents at finite temperatures and average filling one-half. For temperatures below approximately  $J/10$  and values of  $J_{\perp}/J \gtrsim 2$  or  $J_{\perp}/J \lesssim 1$ , that is, deep in the Meissner phase or deep in the vortex phase, respectively, the chiral currents computed in grand-canonical thermal states coincide with the ones obtained in the fermionic ground state. However, even for the smallest temperature considered in Fig. 5.5(b), which is  $J/20$ , the chiral current does not exhibit a clear kink at the critical value,  $J_{\perp}/J = \sqrt{2}$ , of the vortex-to-Meissner transition. We note that the minima of the chiral current systematically overestimate the critical value of the interleg coupling strength  $J_{\perp}$  with increasing temperature.

### Integrated leg-gauge momentum-distribution functions

Within the Meissner phase, the integrated leg-gauge momentum-distribution functions corresponding to the ground state of noninteracting spinless fermions at filling  $\nu = 1/2$  take a constant value equal to one; see Fig. 5.6(a). Note that white corresponds to an occupation of one in the color coding of that figure. The constant momentum-distribution

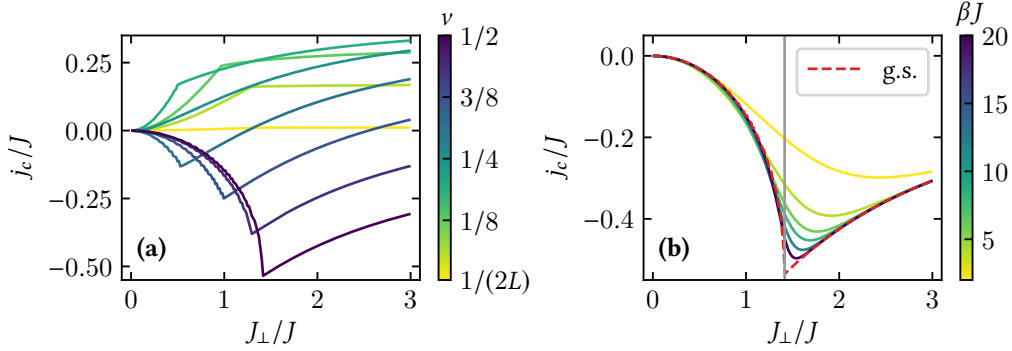


**Figure 5.5: Fermionic chiral currents at zero and finite temperatures.** Considering noninteracting fermions on a ladder with  $L = 128$  rungs, open boundary conditions, and a magnetic flux  $\phi = \pi/2$ . (a) Zero temperature: the ground-state results for different particle fillings  $1/(2L) \leq \nu \leq 1/2$  reveal a current reversal with increasing  $\nu$ . Note that values of  $\nu$  are indicated by the colorbar. At  $\nu = 1/2$ , the cusp of the ground-state chiral current clearly indicates the vortex-to-Meissner transition at  $J_\perp/J = \sqrt{2}$ . (b) Results for the chiral current  $j_c$  computed in grand-canonical thermal states for different inverse temperatures  $\beta$  at average filling one-half. Note that values of  $\beta$  are indicated by the colorbar. The chiral current corresponding to the ground state (g.s.) at filling one-half is shown for comparison (red dashed line). The vertical gray line indicates the zero-temperature critical  $J_\perp/J$  at particle filling  $\nu = 1/2$ .

function be readily understood from the overlap of the energetic bands discussed in the context of Eq. 2.10 and shown in Fig. 2.2(c). In the Meissner phase, the lower band is energetically well separated from the upper band. Hence, at filling one-half, it is fully occupied which leads to a constant momentum-distribution function. Note that the bands shown in Fig. 2.2 and referred to in Eq. (2.10) correspond to the ladder model with periodic boundary conditions while we show data for open boundary conditions in the figure. However, for systems with a large number of rungs  $L$ , boundary effects play a minor role and integrated leg-gauge momentum-distribution functions for open and periodic boundary conditions coincide. On the other hand, in the vortex phase, the ground-state integrated leg-gauge momentum-distribution function is piecewise constant and takes on the values zero, one, and two, corresponding to nonoccupied, singly occupied and doubly occupied momenta; see Fig. 5.6(a). With the onset of finite temperatures, the sharp features of the fermionic ground-state integrated leg-gauge momentum-distribution functions blur out and their discreteness is lost. Figures 5.6(b), 5.6(c), and 5.6(d) show integrated leg-gauge momentum-distribution functions computed in grand-canonical thermal states at average filling one-half and at different temperatures  $J/4$ ,  $J/2$ , and  $J$ , respectively. In the case of fermions, finite temperature

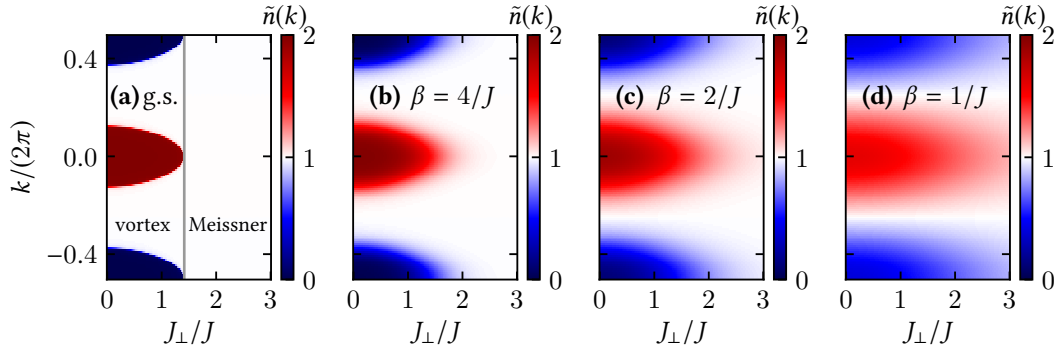


**Figure 5.6: Fermionic momentum-distribution functions at zero and finite temperatures.** Integrated leg-gauge momentum-distribution function  $\tilde{n}(k)$ , as defined in the context of Eq. (2.13), versus interleg coupling strength  $J_{\perp}$ . Considering noninteracting fermions on a ladder with  $L = 128$  rungs, open boundary conditions, and a magnetic flux  $\phi = \pi/2$ . (a) Ground-state (g.s.) momentum-distribution functions at filling  $\nu = 1/2$ . In the vortex phase, the ground-state momentum-distribution function shows a maximum value of two at certain momenta due to the occupation of the upper  $\epsilon_{-}$  band, as discussed in the context of Eq. (2.6). On the other hand, in the Meissner phase, the lower  $\epsilon_{+}$  band is energetically well separated from the upper  $\epsilon_{-}$  band, see Fig. 2.2(c). Thus, at filling  $\nu = 1/2$ , it is fully occupied. This leads to a constant momentum-distribution function  $\tilde{n}(k) = 1$ . The vertical gray line indicates the zero-temperature critical value of  $J_{\perp}/J$ . (b) - (d) Momentum-distribution functions computed in grand-canonical thermal states at average filling one-half and different inverse temperatures (b)  $\beta = 4/J$ , (c)  $\beta = 2/J$ , and (d)  $\beta = 1/J$ .

causes the peak structure characteristic for the vortex phase to extend into the Meissner region, opposite from the behavior of bosons.

### 5.3 Hard-core bosons

In this section, we give an account of our main results addressing the properties of hard-core bosons on the flux-ladder system introduced in Eq. (2.1) at finite temperatures. We emphasize that the hard-core constraint which is considered here applies to the lattice sites but not to the rungs, meaning that there can be at most one particle per site and at most two particles per rung. Also, we consider a magnetic flux  $\phi = \pi/2$ .

#### Chiral currents

Let us start with the presentation of our results concerning the chiral current  $j_c$ . In the thermodynamic limit, a kink at the maximum value of  $j_c$  indicates the critical

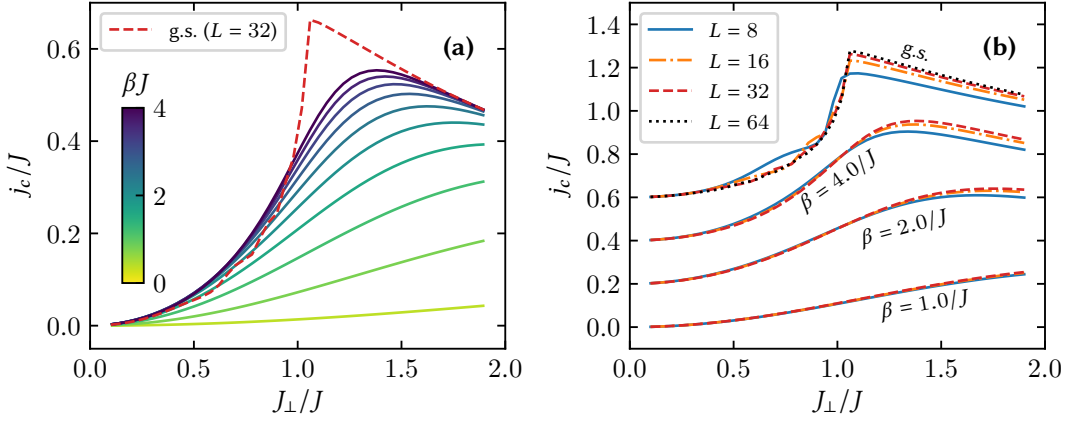


**Figure 5.7: Chiral currents at zero and finite temperatures in the presence of interactions.** Considering hard-core bosons, vanishing rungwise interactions  $V = 0$ , a particle filling  $\nu = 1/2$ , and a magnetic flux  $\phi = \pi/2$ . (a) Chiral currents  $j_c$  in canonical thermal states of hard-core bosons with a fixed number of particles as a function of the interleg coupling strength  $J_\perp$ . We show results for a ladder with  $L = 32$  rungs and different inverse temperatures  $\beta$  indicated by the colorbar. The corresponding chiral current in the ground-state (g.s.) is shown for comparison. (b) Illustration of finite-size effects, comparing the chiral currents for ladders of length  $L = 8, 16, 32$  (for all temperatures) and  $L = 64$  (ground states only). For a better visibility, chiral-current data for  $\beta = 2/J$ ,  $\beta = 4/J$ , and the ground states (g.s.) are vertically offset by 0.2, 0.4, and 0.6.

value of the interleg coupling strength  $J_\perp$  of the ground-state vortex-liquid-to-Meissner transition. By further increasing  $J_\perp$  in the Meissner phase,  $j_c$  is expected to decay to zero as  $j_c \propto 1/J_\perp$  [184].

Figure 5.7(a) shows the chiral current in the ground state of a ladder with  $L = 32$  rungs as a function of the interleg coupling strength  $J_\perp$  for a particle filling  $\nu = 1/2$ ; see the red dashed line. For this value of  $L$ , the kink of the chiral current clearly reveals the location of the ground-state vortex-liquid-to-Meissner transition in the proximity to  $J_\perp/J = 1$ . The solid colored lines in Fig. 5.7(a) show chiral currents corresponding to canonical thermal states of different temperatures ranging from  $0.25J$  to  $2.5J$  for a particle filling  $\nu = 1/2$ . Note that inverse temperatures  $\beta$  are indicated by the colorbar. For values of  $J_\perp$  approximately greater than  $1.5J$ , which is deep in the Meissner phase, and for temperatures below around  $J/3$ , which is deep in the vortex-liquid phase, the chiral currents corresponding to the canonical thermal states overlap with the ones corresponding to the ground state. Also, for sufficiently low temperatures, the finite-temperature currents show clear maxima. However, the positions of these maxima tend to systematically overestimate the critical value of  $J_\perp$  with increasing temperatures.

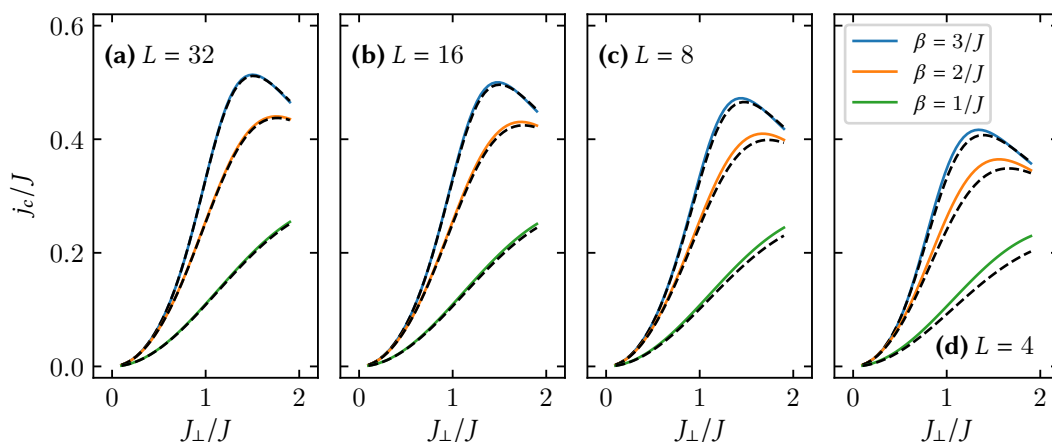


**Figure 5.8: Comparison of chiral currents in the canonical ensemble and in the grand-canonical ensemble.** Considering hard-core bosons, vanishing rungwise interactions  $V = 0$ , and a magnetic flux  $\phi = \pi/2$ . Chiral currents are computed in the canonical thermal states (solid colored lines) with a fixed particle filling  $\nu = 1/2$  and grand-canonical thermal states (black dashed lines) with an average particle filling one-half. We show data for ladders with (a)  $L = 32$ , (b)  $L = 16$ , (c)  $L = 8$ , and (d)  $L = 4$  rungs. In each panel, the lines correspond to inverse temperatures  $\beta = 1/J$ ,  $\beta = 2/J$  and  $\beta = 3/J$  (bottom to top).

Figure 5.7(b) elucidates the role of finite-size effects. The chiral currents computed in canonical thermal states with inverse temperatures  $\beta = 1/J$ ,  $\beta = 2/J$ ,  $\beta = 4/J$  at a particle filling  $\nu = 1/2$ , as well as in the corresponding ground state, are shown for ladders with  $L = 8$ ,  $L = 16$ ,  $L = 32$  and  $L = 64$  (the latter for the ground state only). At zero temperature and in the Meissner phase, the chiral currents for the  $L = 64$  system are slightly more pronounced than those for the  $L = 32$  system. However, as can be seen in Fig. 5.7(b), finite-size effects of the chiral currents play a minor quantitative role, in particular at finite temperatures, where there are only small differences between the  $L = 32$  and  $L = 16$  data for the selected values of  $\beta$ .

In Fig. 5.8, we show that, for small ladder systems, chiral currents corresponding to canonical setups with a fixed particle filling  $\nu = 1/2$  quantitatively differ from those corresponding to grand-canonical setups with an average particle filling one-half. On the other hand, for large systems, canonical and grand-canonical setups are expected to feature the same characteristics and the respective chiral currents should coincide. It can be seen in Fig. 5.8(a) that for a ladder with  $L = 32$  rungs and considered temperatures  $J$ ,  $J/2$  as well as  $J/3$ , canonical (solid colored lines) and grand-canonical chiral currents (dashed black lines) overlap on the scale of the figure. For small systems ( $L = 4$ ,  $L = 8$ ),

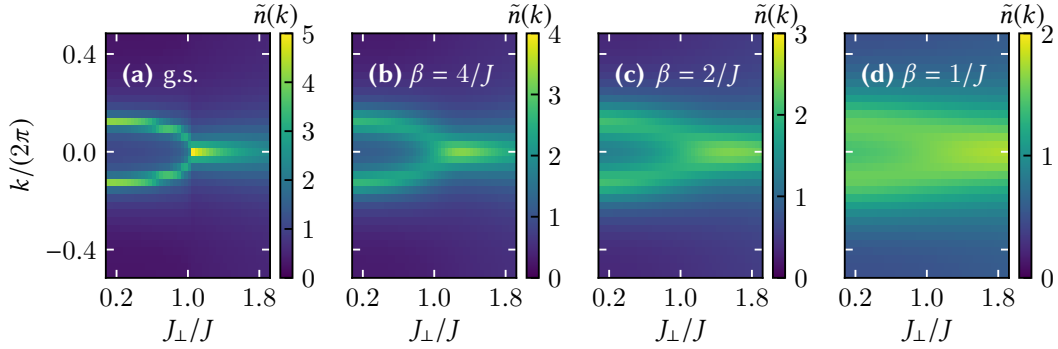


**Figure 5.9: Momentum-distribution functions of hard-core bosons at zero and finite temperatures.** Considering a fixed particle filling  $\nu = 1/2$ , vanishing rungwise interactions  $V = 0$ , and a magnetic flux  $\phi = \pi/2$ . The figure shows integrated leg-gauge momentum-distribution functions  $\tilde{n}(k)$  as a function of the interleg coupling strength  $J_{\perp}$  for a ladder with  $L = 32$  rungs and open boundary conditions. (a) Ground-state (g.s.) momentum-distribution functions. (b)-(d) Momentum-distribution functions corresponding to canonical thermal states with different inverse temperatures (b)  $\beta = 4/J$ , (c)  $\beta = 2/J$ , and (d)  $\beta = 1/J$ .

chiral currents computed from the grand-canonical systems are systematically smaller than those computed in the canonical ensemble. Note that the chiral currents are overall decreasing with decreasing system size due to the increased impact of boundary effects. In the following, we show only results obtained in the canonical ensemble.

### Integrated leg-gauge momentum-distribution functions

Next, we consider integrated leg-gauge momentum-distribution functions  $\tilde{n}(k)$  of hard-core bosons. In this quantity, the ground-state vortex-liquid-to-Meissner transition manifests itself in the transition from two distinct maxima at finite momenta to a single maximum at zero momentum as shown in Fig. 5.9(a). There, we show results for the integrated leg-gauge momentum-distribution functions computed in the ground state of a hard-core boson ladder with  $L = 32$  rungs, for a particle filling  $\nu = 1/2$ . Figure 5.9(b) demonstrates that the characteristic ground-state peaks persist in canonical systems with a finite temperature  $J/4$  and that the two peaks in the vortex-liquid phase can be clearly resolved. However, as expected, these sharp ground-state features blur out with increasing temperatures; see Fig. 5.9(c) and Fig. 5.9(d).

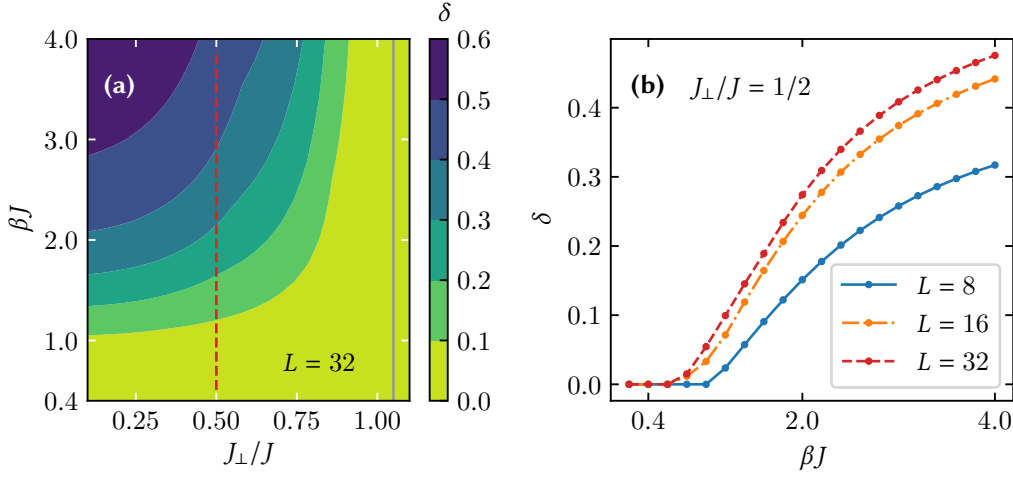


**Figure 5.10: Signatures of the vortex-liquid phase of hard-core bosons at finite temperatures.** Considering a ladder with  $L = 32$  rungs, a fixed particle filling  $\nu = 1/2$ , vanishing rungwise interactions  $V = 0$ , and a magnetic flux  $\phi = \pi/2$ . (a) Contour plot of the contrast  $\delta$ , as defined in Eq. (5.1), for different values of the interleg coupling strength  $J_{\perp}$  and the inverse temperature  $\beta$ . The critical value of  $J_{\perp}/J$  corresponding to the vortex-liquid-to-Meissner phase transition at zero temperature [184] is indicated by a solid gray line. (b) Illustration of finite-size effects: contrast  $\delta$  versus  $\beta J$  for ladders with  $L = 8, 16$ , and  $32$  rungs. Panel (b) shows a cut through panel (a) at  $J_{\perp}/J = 1/2$ , which is also indicated by the red dashed line in (a).

### Signatures of the vortex-liquid phase at finite temperatures

Here, we concentrate on the measure of contrast introduced in Eq. (5.1) in order to quantify at which temperatures clear signatures of the vortex-liquid phase can be detected. Considering a canonical half-filled hard-core boson ladder with  $L = 32$  rungs, Fig. 5.10(a) shows a contour plot of  $\delta$  as a function of the interleg coupling strength  $J_{\perp}$  and the inverse temperature  $\beta$ . For temperatures below around  $\beta^{-1} \lesssim J$  and sufficiently small values of  $J_{\perp} \lesssim 0.8J$ , one finds  $\delta > 1/10$ . This means that two different peaks, and thus a clear signature of the underlying vortex-liquid phase, can be detected. From Fig. 5.10(a), it also becomes apparent that, in the vortex-liquid regime, the contrast  $\delta$  increases with decreasing interleg coupling strength  $J_{\perp}$  and decreasing temperatures  $\beta^{-1}$ .

Moreover, the results for  $\delta$  shown in Fig. 5.10(a) do not suffer from significant finite-size effects as can be seen in Fig. 5.10(b). For the vertical cut at  $J_{\perp}/J = 1/2$  indicated by the red dashed line in Fig. 5.10(a), Fig. 5.10(b) shows the contrast  $\delta$  as a function of inverse temperature  $\beta$  for ladders with  $L = 8, L = 16$ , and  $L = 32$  rungs. Note how

sharply the curves for  $\delta$  drop to zero as signatures of the two maxima in  $\tilde{n}(k)$  are fully blurred out. Thus, the derivative of  $\delta$  with respect to  $\beta$  would also serve as a good indicator for the vortex-liquid-to-Meissner phase crossover. A comparison of the  $L = 32$  data from Fig. 5.10(b) and Fig. 5.4(c) reveals that for noninteracting systems a finite contrast persists at higher temperatures.

### Numerical approach

The finite-temperature results were obtained by means of the canonical purification approach presented in Ch. 3. For the propagation in imaginary time, we employed the second-order Trotter decomposition, which was discussed in the context of Eq. (3.44). We note that this method was implemented from scratch at an early stage of the work on this thesis. The convergence of all relevant observables was ensured by comparing results obtained for different truncation thresholds at fixed Trotter-step widths and vice versa.

## 5.4 Summary

In Ch. 5, we investigated the properties of strongly interacting bosons as well as non-interacting bosons and noninteracting spinless fermions on a two-leg flux ladder at zero and finite temperatures. A particular focus was on the most prominent vortex-to-Meissner quantum-phase transition and the corresponding crossover observed at finite temperatures. The chiral current and the momentum-distributions function were the key observables analyzed here. Our main results for strongly interacting bosons were obtained by means of the matrix-product-state based purification approach introduced in Ch. 3. This method is applicable to canonical setups with a fixed number of particles as well as grand-canonical setups.

Specifically, we presented a comparison between chiral currents in the canonical ensemble and those found in grand-canonical setups. As a result, even for the relatively small particle numbers typical for quantum gases in optical lattices, the technically simpler grand-canonical simulations give quantitatively reliable results for the observables of interest. Moreover, we showed that clearly detectable signatures of the underlying bosonic vortex-liquid phase persist in suitably chosen momentum-distribution functions at finite temperatures. For this, a measure of contrast was introduced in Eq. (5.1) that is sensitive to the presence of finite-momentum peaks in the integrated leg-gauge momentum-distribution function.

Considering the notorious difficulty of cooling a quantum gas to low energy densities [293], we expect our results to provide relevant guidance for future experiments which are naturally at nonzero temperature but allow control over the particle numbers. Our results for the contrast can be compared to the resolution of a given experiment and will thus provide an upper limit for the temperature at which the vortex-liquid phase is visible in the strongly interacting regime. The methods and results presented here might also be relevant in characterizing the final state in quantum-quench dynamics and state-preparation protocols [112, 114, 294].

## Probing the Hall voltage in synthetic quantum systems

In this chapter, we investigate the Hall response of multileg flux-ladder systems. This work is also stimulated by recent quantum gas experiments with artificial magnetic fields. We discuss feasible schemes to extend measurements of the Hall polarization to a study of the Hall voltage, allowing for direct comparison with solid state systems. Specifically, for bosonic flux ladders, we report on characteristic zero crossings and a remarkable robustness of the Hall voltage with respect to interparticle interaction strengths, particle fillings, and ladder geometries. This robustness is unobservable in the Hall polarization. Moreover, we investigate the site-resolved Hall response in spatially inhomogeneous quantum phases.

The realization of artificial gauge fields in ultracold gases opens up an exciting path for the quantum simulation of interacting particles in the presence of large magnetic fluxes; see, for instance, Refs. [27–29, 133–151]. In these platforms, the Hall-like response of a particle current constitutes a fingerprint of the presence of an emulated magnetic field. Pioneering experiments measured the transverse polarization  $p_{\perp}$  in synthetic few-leg flux ladders after inducing a transient longitudinal current  $j_{\parallel}$  [136, 139, 140, 149, 151]. This readily gives rise to the Hall polarization  $P_{\text{H}} = p_{\perp}/j_{\parallel}$ . Above and beyond that, there is the prospect of quantum gases probing the Hall response in the strongly interacting regime. As theoretical calculations remain challenging therein [213–219], quantum simulators might help addressing open questions concerning the Hall effect in strongly correlated quantum phases in solid state systems [295]. Complementarily to recent efforts in nanodevices [296, 297], they might open a new window to study ballistic magnetotransport [220, 298].

While quantum gas experiments typically focus on the measurement of the Hall polarization  $P_{\text{H}}$ , the central quantity of interest in solid state systems is the Hall voltage  $V_{\text{H}}$  or the closely related Hall coefficient  $R_{\text{H}}$ . For certain cases, such as noninteracting Chern-insulating states [149], the Hall polarization can be directly related to the Hall voltage. However, in general, this relation is nontrivial. Thus, it is desirable to generically access the Hall voltage in quantum gas experiments, paving the way for a direct comparison with solid state systems.

For finite systems with open boundaries, we show that the Hall voltage as well as the microscopically resolved Hall polarization can be probed in the transient dynamics induced by suitable quantum quenches, leading to a complementary characterization

of the Hall response in the interacting regime. For the paradigmatic example of bosonic flux ladders, extensive matrix-product-state based simulations and a semiclassical analysis reveal the characteristic zero crossings and the remarkable robustness of the Hall voltage in different quantum phases.

The remainder of this chapter is organized as follows. In Sec. 6.1, we introduce the multileg flux-ladder Hamiltonian which is at the core of our study of the Hall response. There, we also introduce the key quantities of interest, namely the Hall polarization  $P_H$  and the Hall voltage  $V_H$ . In Sec. 6.2, we present different approaches to the computation of the Hall voltage. In Sec. 6.3, we discuss our results concerning the Hall voltage in the interacting regime. There, we also detail on the semiclassical calculations. In Sec. 6.4 we investigate microscopically resolved features of the Hall response. Moreover, in Sec. 6.5, we discuss the overall robustness of the Hall voltage. We comment on the numerical calculations in Sec. 6.6. Finally, our work concerning the Hall response in multileg flux ladders is summarized in Sec. 6.7. Note that the results presented in this chapter were originally put forward in Ref. [1].

## 6.1 The Hall response in few-leg flux ladders

We specify our discussion of the Hall response for the case of synthetic few-leg flux ladders. They are sketched in Fig. 6.1 and governed by the following Hamiltonian

$$\begin{aligned}
H = & -J \sum_{m=0}^{M-1} \sum_{r=0}^{L-1} \left( e^{i\Theta_m} a_{r,m}^\dagger a_{r+1,m} + \text{H.c.} \right) \\
& - J_\perp \sum_{m=0}^{M-2} \sum_{r=0}^{L-1} \left( a_{r,m}^\dagger a_{r,m+1} + \text{H.c.} \right) \\
& + \frac{U}{2} \sum_{m=0}^{M-1} \sum_{r=0}^{L-1} n_{r,m} (n_{r,m} - 1) \\
& + \mu_\perp P_\perp, \tag{6.1}
\end{aligned}$$

where  $M$  denotes the number of legs and  $L$  denotes the number of rungs. As in previous chapters, particle hopping along the legs and rungs is parametrized by  $J$  and  $J_\perp$ , respectively. Moreover, a magnetic flux  $\phi$  piercing each plaquette of the ladder and a current-inducing Aharonov-Bohm flux  $\chi$  are incorporated in the leg hopping terms via

$$\Theta_m = \phi \left( m - \frac{M-1}{2} \right) + \chi/L. \tag{6.2}$$

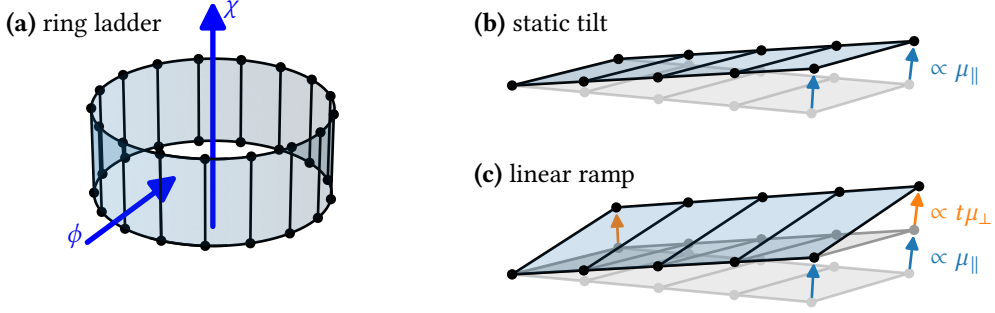


**Figure 6.1:** Sketch of the ring-ladder setup and the different quench schemes. (a) Ring ladder with periodic boundary conditions. Note that the current-inducing Aharonov-Bohm flux  $\chi$  pierces the ring, while the magnetic flux  $\phi$  pierces each plaquette of the ladder. (b) Statically tilted ladder with open boundaries. (c) Linear ramp scheme for the calculation of the Hall voltage  $V_H$ . For simplicity, the magnetic flux  $\phi$  is not shown in (b) and (c). Note that the figure shows two-leg ladders. However, in Sec. 6.5 we consider systems with up to  $M = 4$  legs.

For  $M = 2$  this corresponds to the leg gauge discussed in Ch. 2. In the case of periodic boundary conditions, as shown in Fig. 6.1(a), the magnetic flux  $\phi$  needs to be quantized,  $\phi = m2\pi/L$ , with an even integer  $m$  for an even number of bosons. Site-local interactions are parametrized by the interaction strength  $U$  and we recap that  $n_{r,m} = a_{r,m}^\dagger a_{r,m}$ . Most importantly, in Eq. (6.1) we explicitly account for a transverse potential  $\mu_\perp P_\perp$  with

$$P_\perp = \sum_{m=0}^{M-1} \sum_{r=0}^{L-1} \left( m - \frac{M-1}{2} \right) n_{r,m}. \quad (6.3)$$

This potential plays a crucial role for the definition of the Hall voltage  $V_H$ .

In the following, for the few-leg flux-ladder Hamiltonian (6.1), we introduce the transverse polarization  $p_\perp$ , the longitudinal current  $j_\parallel$ , and the chirality  $j_c(r)$ . The transverse polarization  $p_\perp$  is defined to be an intensive quantity with respect to the length and width of the ladder and given by means of

$$p_\perp = \frac{1}{ML} \langle P_\perp \rangle, \quad (6.4)$$

with  $P_\perp$  as defined in Eq. (6.3). As discussed in Ch. 2, operators representing local particle currents can be derived from the continuity equation for the occupation of local lattice sites,  $\frac{d}{dt} \langle n_{r,m} \rangle = -i \langle [n_{r,m}, H] \rangle$ . Thus, local particle currents  $j_{r,m}^\parallel$  and  $j_{r,m}^\perp$  representing the particle flow from site  $(r, m)$  to site  $(r+1, m)$  and from site  $(r, m)$  to site

$(r, m + 1)$ , respectively, take the form

$$j_{r,m}^{\parallel} = -iJ e^{i\Theta(m,\phi,\chi)} \langle a_{r,m}^{\dagger} a_{r+1,m} \rangle + \text{H.c.}, \quad (6.5)$$

$$j_{r,m}^{\perp} = -iJ_{\perp} \langle a_{r,m}^{\dagger} a_{r,m+1} \rangle + \text{H.c.}. \quad (6.6)$$

The longitudinal current  $j_{\parallel}$  measures the unidirectional particle transport in the (ring) ladder, while the chirality  $j_c(r)$  accounts for the rung-local current along the outer legs in opposite directions. They are defined by means of

$$j_{\parallel} = \frac{1}{ML} \sum_{m=0}^{M-1} \sum_{r=0}^{L-1} j_{r,m}^{\parallel}, \quad j_c(r) = \frac{1}{2} \sum_{r'=r-1}^r \left( j_{r',0}^{\parallel} - j_{r',M-1}^{\parallel} \right). \quad (6.7)$$

We emphasize that the polarization  $p_{\perp}$  as well as the longitudinal current  $j_{\parallel}$  are intensive quantities with respect to the number of lattice sites. It is worth noting that the chirality  $j_c(r)$  can be understood as a rung-resolved variant of the chiral current  $j_c$ , which was introduced in Ch. 2.

### Hall polarization and Hall voltage

On the one hand, in ring-ladder systems with periodic boundary conditions, as shown in Fig. 6.1(a), the theoretically appealing definition of a reactive ground-state Hall response is based on a current-inducing Aharonov-Bohm flux  $\chi$  piercing the ring [213, 214, 219, 220]. In general, a finite value of  $\chi$  induces a longitudinal current  $j_{\parallel}$  and a transverse polarization  $p_{\perp}$ . This readily gives rise to the Hall polarization  $P_{\text{H}}$ , which is defined in for a vanishing transverse potential  $\mu_{\perp} = 0$ ,

$$P_{\text{H}} = p_{\perp} / j_{\parallel}. \quad (6.8)$$

On the other hand, the induced polarization  $p_{\perp}$  might be compensated by means of the transverse potential  $\mu_{\perp} P_{\perp}$  in the Hamiltonian (6.1), enabling the definition of the Hall voltage  $V_{\text{H}}$ . Generalizing an idea by Prelovšek et al. [213], in which a Hall coefficient was determined in the limit of a vanishing magnetic flux,  $\phi \rightarrow 0$ , the Hall voltage  $V_{\text{H}}$  is here defined for finite values of the magnetic flux  $\phi$  by the requirement that the transverse polarization  $p_{\perp}$  vanishes for suitably chosen values of  $\chi$  and  $\mu_{\perp}$ ,

$$V_{\text{H}} = \mu_{\perp} / j_{\parallel}. \quad (6.9)$$

Despite their theoretical appeal, setups with periodic boundary conditions and longitudinal currents  $j_{\parallel}$  are hardly accessible in experiments. Hence, in the following, we propose alternative routes to compute the Hall voltage.

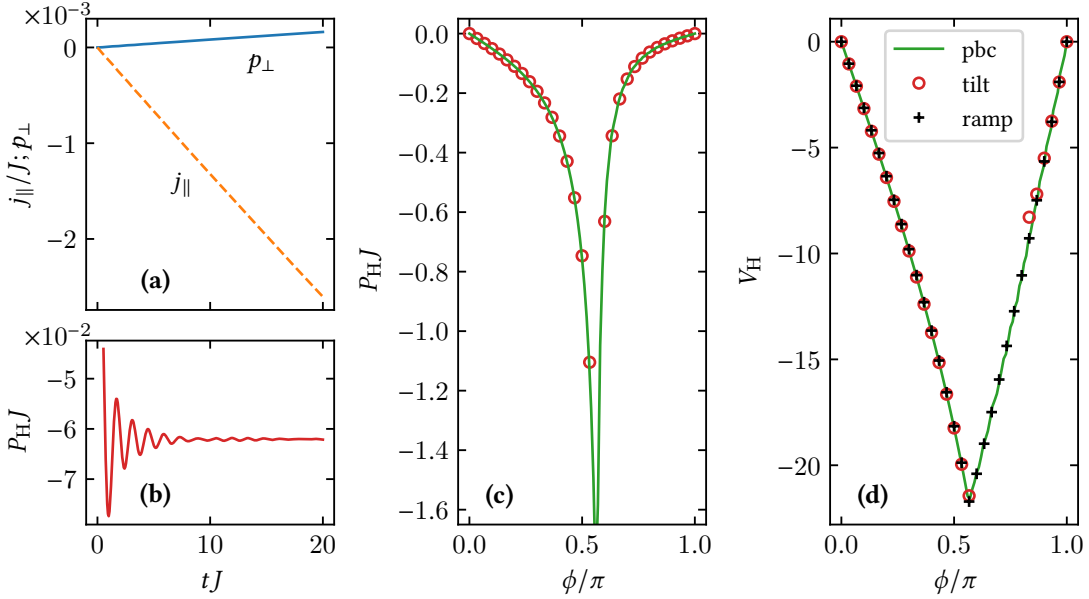


**Figure 6.2: Hall response of noninteracting fermions in a two-leg ladder consistently computed in adiabatic ring ladders, static tilt dynamics, and linear ramp protocols.** Considering noninteracting spinless fermions on a  $M = 2$  leg ladder, a particle filling  $\nu = 0.1$ , and an interleg coupling strength  $J_{\perp}/J = 1.6$ . (a) Transient dynamics in the longitudinal current  $j_{\parallel}$  and in the transverse polarization  $p_{\perp}$  induced by a statically tilted potential  $V_{\parallel}$ , as given in Eq. (6.10) with  $\mu_{\parallel}/J = 10^{-3}$ , for  $\phi/\pi = 0.8$ . (b) Transient dynamics in the Hall polarization  $P_H = p_{\perp}/j_{\parallel}$ . (c) Hall polarization  $P_H$  versus magnetic flux  $\phi$  as obtained from static tilt simulations (tilt) and adiabatic ring-ladder calculations (pbc). (d) Hall voltage  $V_H$  versus  $\phi$  as obtained from static tilt simulations, adiabatic ring-ladder calculations, and linear potential ramps (ramp). Note that the divergence of  $P_H$  and the kink in  $V_H$  indicate the Meissner-to-vortex transition. Similar results for a four-leg ladder are shown in Fig. 6.3.

## 6.2 Measuring the Hall voltage

In a system with open boundary conditions, the Hall voltage  $V_H$  can be efficiently computed in the transient dynamics induced by a linear ramp or a static tilt.

### Linear ramp

Starting off with the ground state of the Hamiltonian (6.1), the instantaneous turning on of a static potential

$$V_{\parallel} = \mu_{\parallel} \sum_{m=0}^{M-1} \sum_{r=0}^{L-1} r n_{r,m} \quad (6.10)$$

at time  $t = 0$ , as shown in Fig 6.1(b), induces a transient longitudinal current  $j_{\parallel}(t)$ , which, in the presence of a magnetic flux  $\phi$ , typically polarizes the system. However, by means of an additional time-dependent potential

$$V_{\perp}(t) = t\mu_{\perp}P_{\perp}, \quad (6.11)$$

as shown in Fig 6.1(c), the transverse polarization  $p_{\perp}$  might be compensated. Adjusting  $\mu_{\perp}$  such that the time average of the induced transverse polarization  $p_{\perp}$  vanishes,  $\langle p_{\perp}(t) \rangle_t = 0$ , the Hall voltage can be computed as

$$V_{\text{H}} = \left\langle \frac{\mu_{\perp}t}{j_{\parallel}(t)} \right\rangle_t. \quad (6.12)$$

Here, the time averages are computed as  $\langle \bullet \rangle_t = \int_{t_i}^{t_f} \frac{\bullet}{t_f - t_i} dt$  for a suitable time interval  $[t_i, t_f]$  in the transient regime.

### Static tilt

By neglecting the dual Hall effect, referring to the longitudinal current induced by the transverse polarization, the Hall voltage  $V_{\text{H}}$  can be effectively calculated using a simplified protocol. First, by instantaneously tilting the ladder by means of  $V_{\parallel}$ , the Hall polarization  $P_{\text{H}}$  can be computed by time averaging the quotient of the induced transverse polarization  $p_{\perp}$  and the induced longitudinal current  $j_{\parallel}$ ,

$$P_{\text{H}} = \left\langle \frac{p_{\perp}(t)}{j_{\parallel}(t)} \right\rangle_t, \quad (6.13)$$

in the transient dynamics. Moreover, in the static tilt protocol the Hall voltage  $V_{\text{H}}$  is approximated by means of

$$V_{\text{H}} = P_{\text{H}} \left( \frac{\mu_{\perp}}{p_{\perp}} \right), \quad (6.14)$$

where  $(\mu_{\perp}/p_{\perp})$  is obtained for open boundary conditions and in the limit  $\mu_{\perp} \rightarrow 0$ .

The static tilt protocol and the linear ramp protocol are both feasible in synthetic-dimension implementations [139, 140], where the legs of the ladder correspond to different internal states of the trapped atoms. In this case,  $V_{\parallel}$  and  $V_{\perp}(t)$  can be realized by shifting the optical confining potential [149] and by detuning the internal states [133], respectively. Further,  $j_{\parallel}$  can be probed in time-of-flight measurements and Stern-Gerlach separation allows for measurements of the leg-resolved particle density, giving rise to  $p_{\perp}$ . The protocols are also applicable to real-space implementations of flux ladders, in which quantum gas microscopes enable measurements of the relevant observables and optical gradients can realize  $V_{\parallel}$  and  $V_{\perp}(t)$  [105, 144], as well as to continuum systems with spin-orbit coupling [133, 134, 151].

### Hall response of noninteracting fermions

The consistency of both time-dependent protocols with the ring-ladder setup is exemplified for noninteracting spinless fermions in a two-leg ladder in Fig. 6.2. Figure 6.2(a) and Fig. 6.2(b) show transient dynamics in the polarization  $p_{\perp}$ , the longitudinal current  $j_{\parallel}$ , and the Hall polarization  $P_{\text{H}} = p_{\perp}/j_{\parallel}$  induced by the tilt potential  $V_{\parallel}$ . The time-averaged results for  $P_{\text{H}}$  perfectly agree with the analytic results for periodic boundary conditions for  $\phi \in [0, \pi]$ , as shown in Fig. 6.2(c). The Hall voltage  $V_{\text{H}}$ , shown in Fig. 6.2(d), as well as the Hall polarization  $P_{\text{H}}$  exhibit a nonanalyticity at the transition from a weak-flux Meissner region to a vortex phase found for large values of the magnetic flux  $\phi$ . Moreover, as shown in Fig. 6.2(d), the Hall voltage  $V_{\text{H}}$  as obtained from the linear ramp protocol perfectly agrees with the analytic results for periodic boundary conditions, while  $V_{\text{H}}$  as obtained from the static tilt approximation merely deviates in the immediate proximity to the quantum phase transition.

In Fig. 6.3, we exemplify the different quench protocols for the case of noninteracting spinless fermions in a four-leg flux ladder. Again, the results for the Hall polarization  $P_{\text{H}}$  and the Hall voltage  $V_{\text{H}}$  which are obtained from the linear ramp protocol are in perfect accordance with the exact results obtained from the ground states in setups with periodic boundaries for  $\phi \in [0, \pi]$ . The results obtained from the static tilt protocol overlap well with the exact curves except for a small window of parameters in the vicinity of a quantum phase transition.

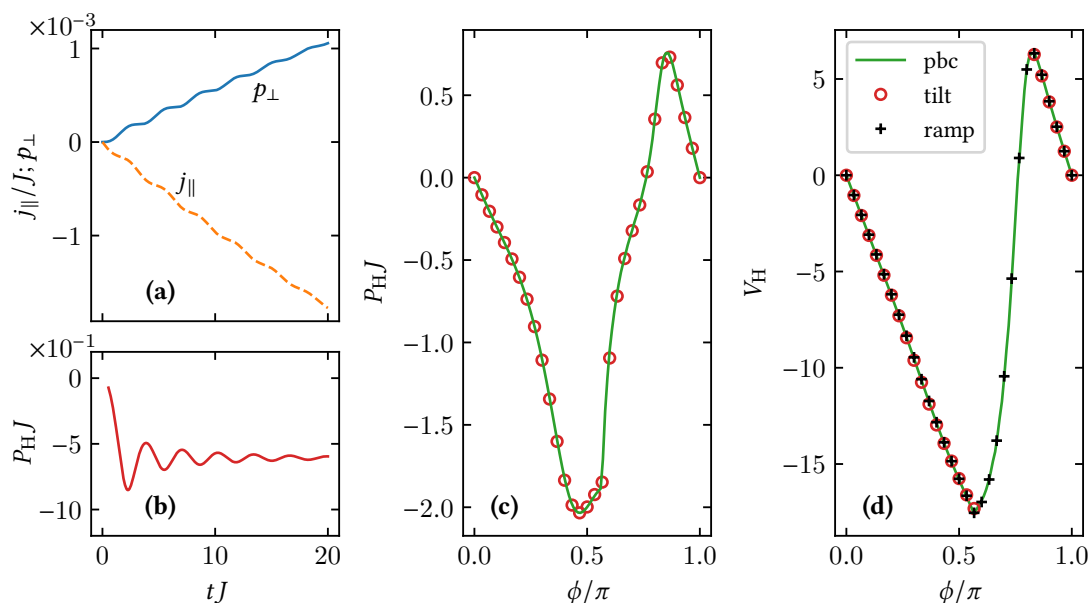


**Figure 6.3: Hall response of noninteracting fermions in a four-leg ladder consistently computed in adiabatic ring ladders, static tilt dynamics, and linear ramp protocols.** Considering noninteracting spinless fermions on a  $M = 4$  leg ladder, a particle filling  $\nu = 0.1$ , and an interleg coupling strength  $J_{\perp}/J = 1.6$ . (a) Transient dynamics in the longitudinal current  $j_{\parallel}$  and in the transverse polarization  $p_{\perp}$  induced by a statically tilted potential  $V_{\parallel}$ , as given in Eq. (6.10) with  $\mu_{\parallel}/J = 10^{-3}$ , for  $\phi/\pi = 0.2$ . (b) Transient dynamics in the Hall polarization  $P_H = p_{\perp}/j_{\parallel}$ . (c) Hall polarization  $P_H$  versus magnetic flux  $\phi$  as obtained from static tilt simulations (tilt) and adiabatic ring-ladder calculations (pbc). (d) Hall voltage  $V_H$  versus  $\phi$  as obtained from static tilt simulations, adiabatic ring-ladder calculations, and linear potential ramps (ramp). Note that similar results for a two-leg ladder are shown in Fig. 6.2.

### 6.3 Interacting systems

In the following, we examine the Hall voltage in bosonic flux ladders in the interacting regime. Employing extensive matrix-product-state based simulations, performed by means of the SyTen toolkit [245, 249], we calculate the Hall voltage in quantum quenches as well as in ring-ladder setups, providing evidence for the consistency of both approaches in the strongly correlated regime. Specifically, for ground-state calculations, we employ the single-site variant [250] of the density-matrix renormalization-group method, as discussed in Ch. 3. For quench simulations, we employ the time-dependent variational-principle algorithm [36, 284]. We detail on the matrix-product-state based simulations in Sec 6.6.

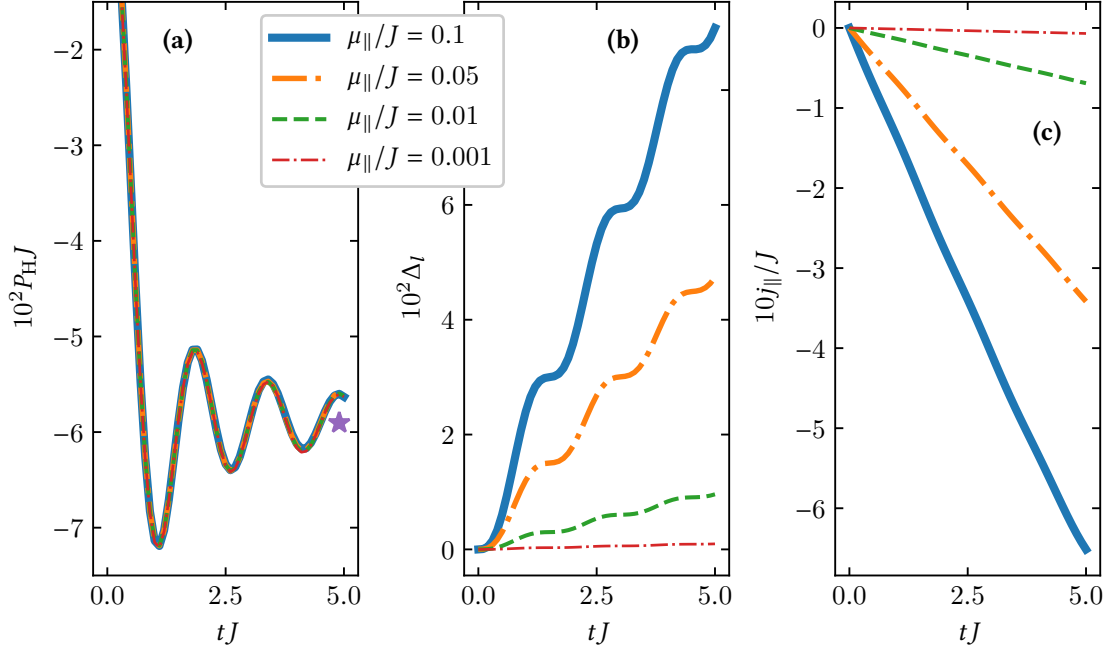


**Figure 6.4: Static tilts in the interacting Meissner phase.** Considering different values of  $\mu_{\parallel}$  for  $\phi/\pi = 0.2$ ,  $J_{\perp}/J = 1.6$ ,  $U/J = 2$ ,  $\nu = 0.8$ , and  $M = 2$ . (a) Transient dynamics in the Hall polarization  $P_{\text{H}}$ . Note that the curves for  $\mu_{\parallel}/J = 0.1, 0.05, 0.01$ , and  $0.001$  fall on top of each other. The Hall polarization calculated in the ground state of the corresponding ring ladder is indicated by the purple star and shown for comparison. (b) Transient dynamics in the population imbalance  $\Delta_l$  between the two legs of the ladder. As the particle-density profile is homogeneous in the Meissner phase, the population imbalance is the same for all rungs  $r$  in the center of the system. (c) Transient dynamics in the current  $j_{\parallel}$ .

Let us start off with Fig. 6.4. For an interacting two-leg ladder and model parameters corresponding to the Meissner phase, it is shown that the static tilt protocol is applicable to a broad range of values of  $\mu_{\parallel}$ . Concretely, we consider  $\mu_{\parallel}/J = 0.001, 0.01, 0.05$ , and  $0.1$  for  $\phi/\pi = 0.2$ ,  $J_{\perp}/J = 1.6$ ,  $U/J = 2$ , and  $\nu = 0.8$ . Figure 6.4(a) shows that the transient dynamics in the Hall polarization  $P_{\text{H}}$  are independent of the considered value of  $\mu_{\parallel}$ . However, the current  $j_{\parallel}$  and the polarization  $p_{\perp}$  induced by the static tilts scale roughly proportional to  $\mu_{\parallel}$ . Figure 6.4(b) and Fig. 6.4(c) show the leg-population imbalance

$$\Delta_l = |\langle n_{r,0} - n_{r,1} \rangle| / \langle n_{r,0} + n_{r,1} \rangle \quad (6.15)$$

and the current  $j_{\parallel}$  as a function of the time  $t$ , respectively. The Meissner phase exhibits a homogeneous particle-density profile. Thus, the population imbalance is the same for

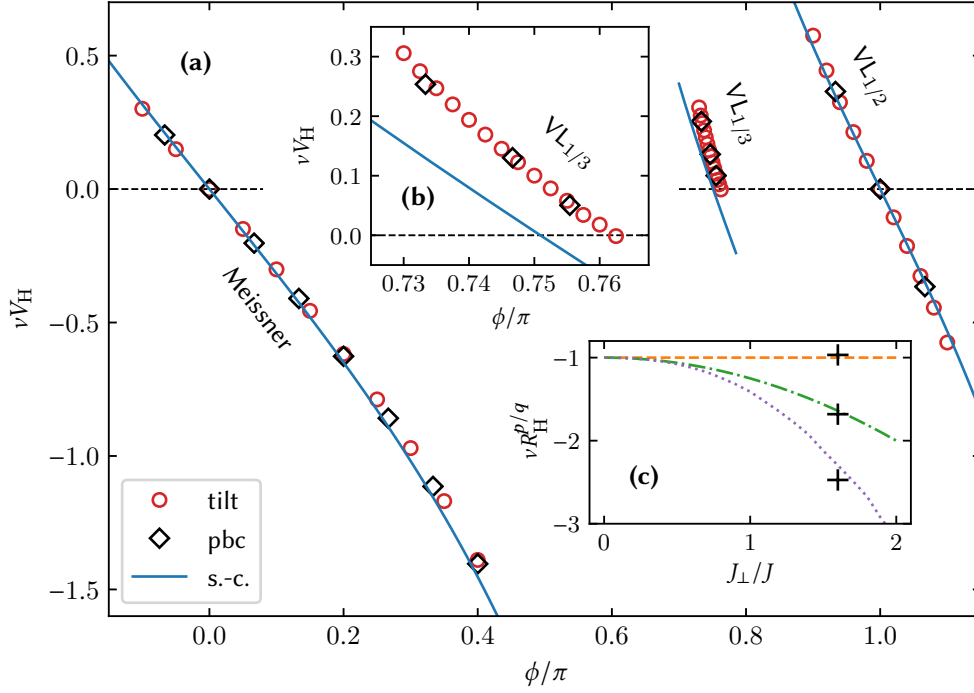


**Figure 6.5: Hall voltage versus magnetic flux in Meissner and vortex-lattice phases.** The figure shows the scaled Hall voltage  $\nu V_H$  as a function of the magnetic flux  $\phi$  for interacting bosons in a two-leg ladder. Considering a particle filling  $\nu = 0.8$ , an interaction strength  $U/J = 2$ , and an interleg coupling strength  $J_\perp/J = 1.6$ . (a) Symbols depict  $\nu V_H$  as obtained from matrix-product-state based static-tilt simulations (tilt) and adiabatic ring-ladder calculations (pbc) in the Meissner phase, in the vortex-lattice $_{1/2}$  phase (VL $_{1/2}$ ), and in the vortex-lattice $_{1/3}$  phase (VL $_{1/3}$ ). The solid blue line shows the semiclassical result (s.-c.) discussed in the context of Eq. (6.17). The upper inset (b) is a close-up of the vortex-lattice $_{1/3}$  data. The lower inset (c) shows the generalized Hall coefficient  $R_H^{p/q}$ , as defined in Eq. (6.22), for the Meissner phase (top dashed line), the vortex-lattice $_{1/2}$  phase (middle dashed-dotted line), and the vortex-lattice $_{1/3}$  phase (bottom dotted line) obtained from the semiclassical approach, showing quadratic scaling in accordance with Eq. (6.23). The crosses depict the matrix-product-state based data at  $J_\perp/J = 1.6$ .

all rungs  $r$  in the center of the system. For the strong tilt with  $\mu_\parallel/J = 0.1$  and at time  $t = 5/J$  the particle numbers in the two legs differ by more than 15%.

Moreover, Fig. 6.5 shows the Hall voltage  $V_H$  for a system of strongly correlated particles as a function of the magnetic flux  $\phi$ , considering  $U/J = 2$ ,  $J_\perp/J = 1.6$ , and an incommensurate particle filling  $\nu = 0.8$ , where  $\nu = N/(ML)$  and  $N$  denotes the number of particles. Specifically,  $V_H$  is shown in the Meissner phase, in the vortex-lattice $_{1/2}$  phase, and in the vortex-lattice $_{1/3}$  phase, noting that intermediate regions of

vortex-liquid phases are omitted [186]. The matrix-product-state based results obtained by simulating tilt dynamics show excellent agreement with the ones obtained from ground-state calculations in ring ladders with periodic boundary conditions. Moreover, our results shown in Fig. 6.5 reveal a remarkable interaction-driven effect: a series of linear zero crossings of the Hall voltage  $V_H$  in different vortex-lattice phases.

### Semiclassical approach

In order to approach the Hall response in the vortex-lattice phases from a different angle, we extend a semiclassical description [175–178]. This ansatz, which addresses the regime of weak but finite interaction strengths  $U$ , is well suited for the description of vortex-lattice phases. Assuming a local coherent Josephson phase  $\theta_{r,m}$  and a classical density  $v_{r,m}$ , we employ a coherent-state description of the ring ladder, replacing

$$a_{r,m} \longrightarrow \sqrt{v_{r,m}} e^{i\theta_{r,m}} \quad (6.16)$$

in the expectation value of the Hamiltonian (6.1). Thus, the starting point of the semiclassical approach is

$$\begin{aligned} \langle H \rangle = & -2J \sum_{m=0}^{M-1} \sum_{r=0}^{L-1} \sqrt{v_{r,m} v_{r+1,m}} \cos(\theta_{r+1,m} - \theta_{r,m} + \Theta_m) \\ & - 2J_{\perp} \sum_{m=0}^{M-2} \sum_{r=0}^{L-1} \sqrt{v_{r,m} v_{r,m+1}} \cos(\theta_{r,m} - \theta_{r,m+1}) \\ & + \frac{U}{2} \sum_{m=0}^{M-1} \sum_{r=0}^{L-1} v_{r,m} (v_{r,m} - 1) \\ & + \mu_{\perp} \sum_{m=0}^{M-1} \sum_{r=0}^{L-1} \left( m - \frac{M-1}{2} \right) n_{r,m}. \end{aligned} \quad (6.17)$$

Typical low-energy configurations of the Josephson phase  $\theta_{r,m}$  in vortex-lattice phases are shown in Fig. 6.6. They exhibit a regular series of localized vortices where  $\theta_{r,m}$  slips by  $\pi$ . In the intermediate regions the phases  $\theta_{r,0}$  and  $\theta_{r,1}$  are aligned, similar to a small Meissner phases. Moreover, the vortices delocalize as  $J_{\perp}/J$  decreases and typical low-energy configurations satisfy

$$\theta_{r+1,0} - \theta_{r,0} \approx -\theta_{r+1,1} + \theta_{r,1}. \quad (6.18)$$

It is worth noting that in the limit  $J_{\perp}/J \rightarrow 0$  and for a homogeneous particle density  $v_{r,m} = v$ , a complete devil's staircase of such vortex-lattice $_{p/q}$  phases, at each commensurate vortex density  $p/q$ , is predicted. Finite values of  $J_{\perp}/J$  and interactions gradually destabilize the vortex-lattice $_{p/q}$  phases with largest  $q$  [179].

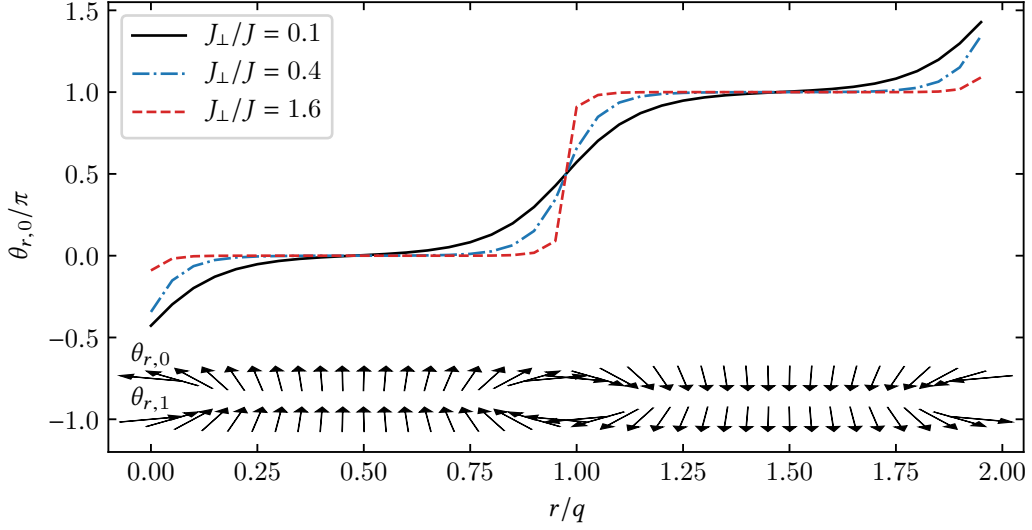


**Figure 6.6: Vortex-lattice ground-state configuration in the semiclassical approach.** Josephson phase  $\theta_{r,m=0}$  in the semiclassical approach introduced in the context of Eq. (6.17) for the vortex-lattice $_{1/20}$  phase considering an interaction strength  $U/J = 2$ , a particle filling  $\nu = 0.8$ , a magnetic flux  $\phi/\pi = 0.2$ , and different values of the interleg coupling strength  $J_{\perp}/J$ . The lower arrows sketch the real space behavior of the phases in the  $m = 0$  and  $m = 1$  leg of the ladder for  $J_{\perp}/J = 0.1$ . Vortices, corresponding to the  $\pi$ -phase slips, delocalize as  $J_{\perp}/J$  decreases.

For the practical calculation of the Hall response in the semiclassical approach, as well as for the calculation of the configurations shown in Fig. 6.6, we consider a homogeneous particle density per rung, employing the following parametrization for a two-leg ladder

$$v_{r,0} = 2\nu \cos^2(\alpha_r) \quad v_{r,1} = 2\nu \sin^2(\alpha_r) . \quad (6.19)$$

We minimize the energy  $\langle H \rangle$ , as given in Eq. (6.17), with respect to the parameters  $\alpha_r$  and  $\theta_{r,m}$  for  $r = 0, 1, \dots, L-1$  and  $m = 0, 1$ . For the calculation of the Hall voltage  $V_H$  the transverse gradient  $\mu_{\perp}$  in Eq. (6.17) is considered as a Lagrange multiplier. The Hall polarization  $P_H$  is obtained for  $\mu_{\perp} = 0$ . Hence, in the Meissner phase, which can also be understood as the vortex-lattice $_{(p/q)=0}$  phase, we find

$$V_H = -\frac{2}{\nu} \tan\left(\frac{\phi}{2}\right) . \quad (6.20)$$

Moreover, the semiclassical result for the Hall voltage in the vortex-lattice $_{1/2}$  phase reads

$$V_H = -\frac{1}{\nu} \frac{2 \sin(\phi) \left( \frac{J_{\perp}^2}{J^2} - 2 \cos(\phi) + 2 \right)}{\left( \frac{J_{\perp}^2}{J^2} + 4 \right) \cos(\phi) + \frac{J_{\perp}^2}{J^2} - \cos(2\phi) - 3}. \quad (6.21)$$

For vortex-lattice $_{1/q}$  phases with  $q > 2$ , we numerically compute minima of the energy  $\langle H \rangle$  in the vicinity to an initial configuration given by  $\alpha_r = \pi/4$  and  $\theta_{r,m} = \pi \lfloor r/q \rfloor$  for  $r = 0, 1, \dots, L-1$  and  $m = 0, 1$ . Thus, the vortex-lattice $_{p/q}$  configurations shown in Fig. 6.6 do not necessarily correspond to the true ground state in the semiclassical model (6.17) for the considered model parameters but resemble metastable configurations for a fixed vortex filling with  $p = 1$  vortices in  $q = 20$  rungs. In Fig. 6.5 the semiclassical results are depicted by the blue solid line. They show good agreement with the matrix-product-state based results, noting that Fig. 6.5(b) shows deviations in the vortex-lattice $_{1/3}$  phase.

In the semiclassical framework, the analysis of the Hall voltage  $V_H$  reveals a zero crossing in the center of each vortex-lattice $_{p/q}$  phase at a certain value of the magnetic flux  $\phi_{p/q}$ . Thus, we define generalized Hall coefficients

$$R_H^{p/q} = \left. \frac{dV_H}{d\phi} \right|_{\phi=\phi_{p/q}} \quad (6.22)$$

in analogy to the Hall coefficient obtained in the limit of a vanishing magnetic flux  $\phi \rightarrow 0$  by Prelovšek et al. [213]. Generically, the semiclassical approach yields

$$R_H^{p/q} \approx -\frac{1}{\nu} \left( 1 + \gamma_{p/q} \left( \frac{J_{\perp}}{J} \right)^2 \right), \quad (6.23)$$

with a constant  $\gamma_{p/q}$ . We emphasize that in the Meissner phase ( $\phi_{(p/q)=0} = 0$ ) and in the vortex-lattice $_{1/2}$  phase ( $\phi_{1/2} = \pi$ ), Eq. (6.23) holds exactly with  $\gamma_0 = 0$ , which is in accordance with Greschner et al. [219], and  $\gamma_{1/2} = 1/4$ . In the vortex-lattice $_{1/3}$  phase, we find  $\gamma_{1/3} \approx 0.51$  and higher order corrections in  $J_{\perp}/J$ . The lines in Figure 6.5(c) depict  $R_H^{p/q}$  in the Meissner phase, in the vortex-lattice $_{1/2}$  phase, and in the vortex-lattice $_{1/3}$  phase as obtained from the semiclassical approach. They are in accordance with the values calculated from the matrix-product-state based data for  $J_{\perp}/J = 1.6$ .

## 6.4 Rung-resolved Hall response

Microscopic features, such as the rung-resolved transverse polarization  $p_{\perp}$ , provide additional insight into the Hall response in spatially inhomogeneous vortex-lattice phases.

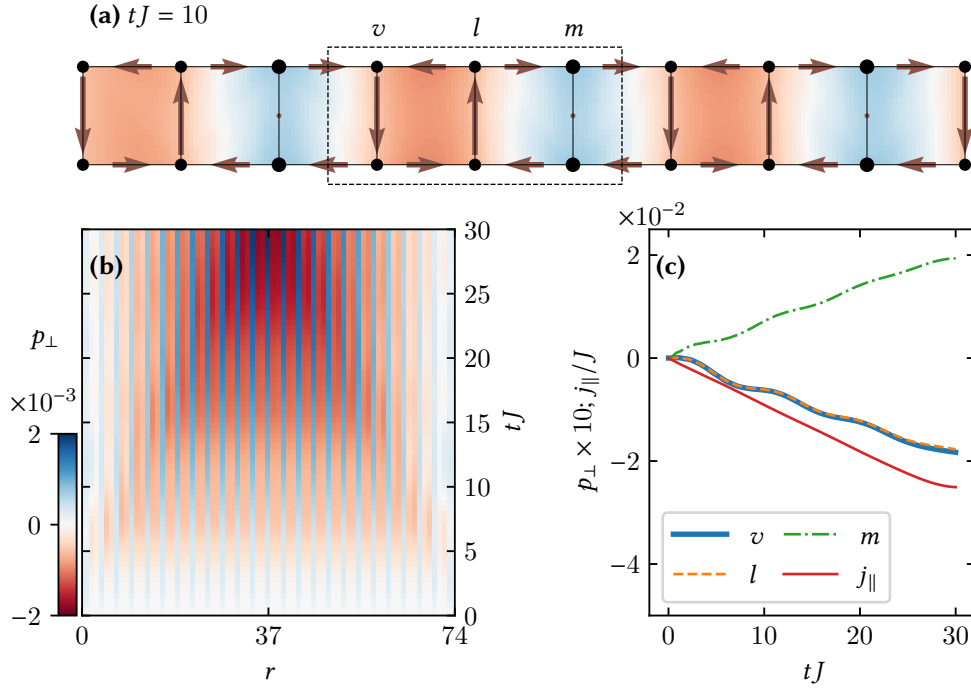


**Figure 6.7: Rung-resolved Hall response after a static tilt in the vortex-lattice phase.** Considering the vortex-lattice $_{1/3}$  phase in a two-leg ladder with  $L = 75$  rungs for a particle filling  $\nu = 0.8$ , an interaction strength  $U/J = 2$ , an interleg coupling strength  $J_{\perp}/J = 1.6$ , and a magnetic flux  $\phi/\pi = 0.75$ . The transient dynamics are induced by a static tilt as discussed in the context of Eq. (6.10) with  $\mu_{\parallel}/J = 10^{-3}$  and simulated by means of matrix-product states. (a) Snapshot of the ten most central rungs at time  $t = 10/J$  after the quench. The size of the dots depicts the local particle density, the background shading indicates the rung-local polarization  $p_{\perp}$  using the colorcode from (b), and the arrows show the strength of the local particle currents. (b) Rung-resolved time evolution of the polarization  $p_{\perp}$ . (c) Transient dynamics in  $p_{\perp}$ , considering the rungs  $v$ ,  $l$ , and  $m$  indicated in (a). The solid red line shows the nearly linear increase of the longitudinal current  $j_{\parallel}$ , which is spatially homogeneous in the center of the system.

Using matrix-product-state based simulations of the static tilt scheme introduced in Sec. 6.2, we examine the rung-resolved Hall response. Figure 6.7(a) depicts the local configuration of a tilted state in the vortex-lattice $_{1/3}$  phase, where vortices with currents circulating counter-clockwise are surrounded by Meissner-like regions of opposite chirality. Figure 6.7(b) and Fig. 6.7(c) show the transient dynamics in the rung-resolved polarization. Interestingly, the Hall response is strongly inhomogeneous, following the crystalline structure of the underlying vortex-lattice phase, which remains pinned during the time evolution induced by the tilt. In particular, we observe a positive Hall polarization of the vortices, while the Meissner-like rungs exhibit a negative Hall polarization. Thus, we are able to attribute to the different regions an effective local charge reflecting their Hall response. The vortices behave holelike, while the Meissner-like regions behave particlelike. At a certain value of the magnetic flux,  $\phi_{p/q}$  in each vortex-lattice $_{p/q}$  phase, the competing contributions from holelike and particlelike regions cancel out, leading to a vanishing macroscopic Hall response. The structure of the local Hall response may also be understood as a signature of the vortex-hole duality, meaning that vortices in a weakly interacting ladder may be identified with holes in a strongly interacting one-dimensional chain with a staggered potential related to thin-torus-limit states of the fractional quantum Hall effect [187].

Moreover, the spatially inhomogeneous Hall response following the structure of the underlying vortex-lattice phases can be recovered in the semiclassical framework. Indeed, numerical solutions confirm a direct relation between the rung-resolved Hall polarization  $P_H$  and the chirality  $j_c(r)$  of the local currents in the vortexlike and Meissner-like rungs, which has been tested for various vortex-lattice $_{1/q}$  phases up to  $q = 20$ . Figure 6.8(a) and Fig. 6.8(b) show  $P_H$  and  $j_c(r)$  in the vortex-lattice $_{1/20}$  phase for different values of the magnetic flux  $\phi$ . The vortices exhibit a holelike Hall response with  $V_H > 0$  and  $j_c > 0$ , while in the surrounding particlelike Meissner regions one finds  $V_H < 0$  and  $j_c < 0$ . Thus, quantum gas microscopy [144] might open a new window in the study of the Hall response of coherent quantum systems, addressing microscopic features of the Hall response and local effective charge distributions.

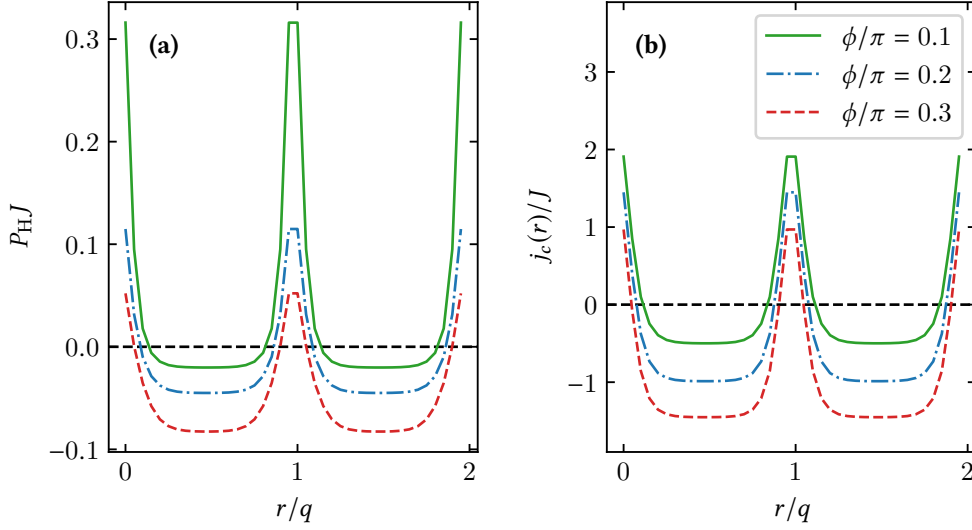


**Figure 6.8: Rung-resolved Hall response in the semiclassical approach.** (a) Rung-resolved Hall polarization  $P_H$  and (b) chirality  $j_c(r)$  in the vortex-lattice $_{1/20}$  phase, considering  $J_{\perp}/J = 0.4$ ,  $U/J = 2$ ,  $\nu = 0.8$ , and different values of the magnetic flux  $\phi$ . Note that for the model parameters considered here, the vortex-lattice $_{1/20}$  configurations are metastable solutions, which do not necessarily correspond to the ground state in the semiclassical model.

## 6.5 Robustness of the Hall voltage

The remarkable overlap between the matrix-product-state based results for the Hall voltage  $V_H$  in the strongly correlated regime and the results obtained from the semiclassical approach, as discussed in the context of Fig. 6.5, indicates a robustness of  $V_H$  with respect to the interaction strength  $U$ .

In Fig. 6.9 we examine this robustness in more detail. There, we consider different values of  $U$  and different particle fillings  $\nu$  for various values of the magnetic flux  $\phi$ . In contrast to the Hall polarization  $P_H$ , which depends nonuniversally on the values  $U$  and  $\nu$ , the scaled Hall voltage  $\nu V_H$  collapses to one curve for a broad regime of parameters in the Meissner phase and in the vortex-lattice $_{1/2}$  phase. Moreover, in the Meissner phase, up to  $M = 4$  legs are considered within the adiabatic ring-ladder framework as well as in the static tilt approach, revealing an additional robustness of the Hall voltage  $V_H$  with respect to the ladder geometry. We note that for strong interparticle interaction strengths and for particle fillings close to the transition to a vortex-liquid phase, we have observed deviations from the robust behavior. Finally, we emphasize that the robustness of the Hall voltage described here is different from other robust or universal

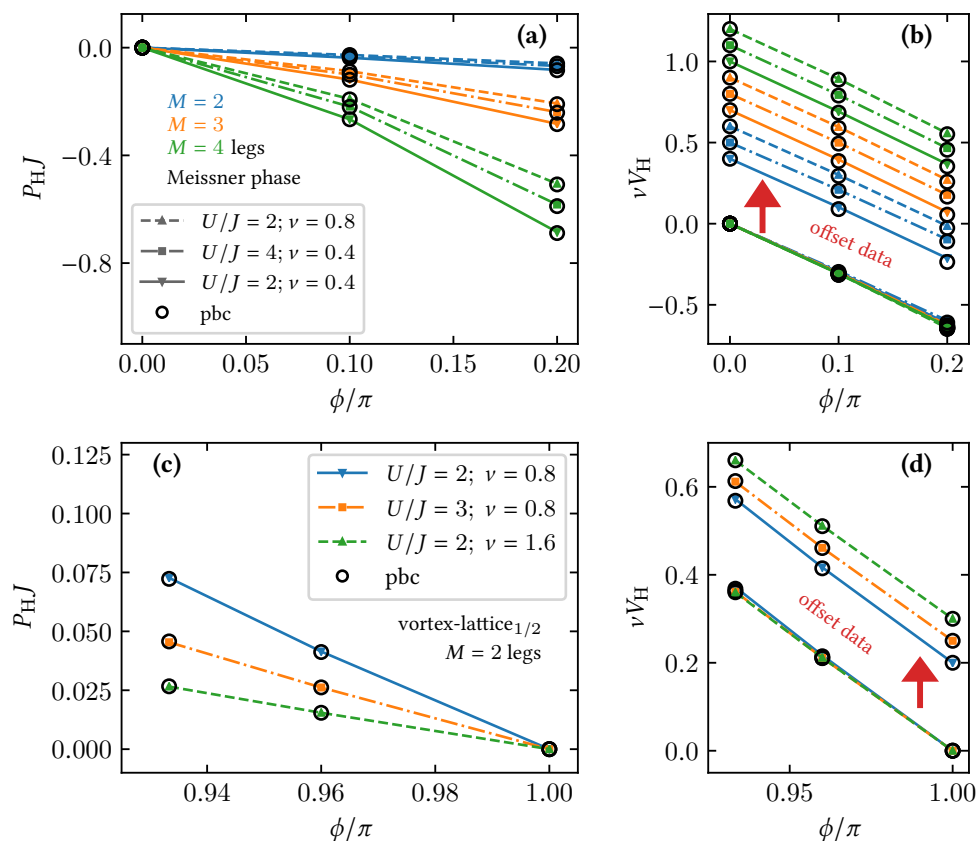


**Figure 6.9: Robustness of the Hall voltage.** Considering  $J_{\perp}/J = 1.6$ . (a) and (b) are for the Meissner phase, showing the Hall polarization  $P_H$  and the Hall voltage  $V_H$  as a function of the magnetic flux  $\phi$  for multileg ( $M = 2, 3, 4$ ) ladders, different particle fillings  $\nu = N/(LM)$ , and interparticle interactions strengths  $U$ . Note that the data in (b) are vertically offset by  $0.1n + 0.4$  (with  $n = 0, 1, 2, \dots$  for different values of  $M$ ,  $\nu$ , and  $U$ ) for the purpose of a clear presentation. (c) and (d) are for the vortex-lattice $_{1/2}$  phase. The data in (d) are also vertically offset by  $0.05n + 0.2$ .  $P_H$  and  $V_H$  are obtained by means of static tilt simulations (lines) and adiabatic ring-ladder calculations (open circles), as described in the text. Contrarily to  $P_H$ , the  $\nu V_H$  data scale on top of each other for different particle fillings  $\nu$ , interaction strengths  $U$ , and numbers of rungs  $M$ .

features of the Hall imbalance occurring in certain quench scenarios [220] and for the case of  $SU(M)$ -symmetric interactions and weak magnetic fields [219].

## 6.6 Numerical approach

Here, we provide additional information on the matrix-product-state based approaches employed for the calculation of the Hall response in the strongly correlated regime, acknowledging that both, ground-state calculations as well as time-dependent calculations, are performed by means of the SyTen toolkit [245, 249]. Throughout our work, the  $U(1)$  symmetry of the flux-ladder Hamiltonian (6.1) corresponding to the conservation of the total particle number is enforced on the level of the matrix-product-state tensors. Moreover, a cutoff at at most six bosons per lattice site is sufficient for the model parameters considered here.

### Ground states in the ring-ladder setup

The ground states in the ring-ladder setup are calculated by means of the density-matrix renormalization-group method [32, 35], as described in Ch. 3. Specifically, we employ the single-site variant of the algorithm using subspace expansion [250]. In the course of these calculations, we consider bond dimensions up to typically 3000.

In general, periodic boundary conditions complicate the variational ground-state optimization, and, in practice, they require an increased amount of sweeping as compared to the optimization in analogous systems with open boundary conditions. Moreover, the quantization of the magnetic flux  $\phi$ , as discussed in the context of the Hamiltonian (6.1), manifests itself as a challenging constraint. Especially for ground-state phases appearing in a narrow window of  $\phi$ , large systems may need to be considered. Concretely, in order to resolve the vortex-lattice<sub>1/3</sub> phase in Fig. 6.5, we consider ladders with  $L = 60, 75, \text{ and } 90$  rungs and periodic boundary conditions. For the calculation of ground states in the presence of a finite current-inducing Aharonov-Bohm flux  $\chi$ , we generically employ the ground states attained at  $\chi = 0$  as an initial state.

Convergence of the variationally optimized ground states is ensured by means of a comparison of the energies  $\langle H \rangle$ , the energetic variance  $\langle H^2 \rangle - \langle H \rangle^2$ , as well as all relevant global and local observables for different bond dimensions and different values of the site-local bosonic cutoff. Additionally, it is ensured that the ground states in the Meissner phase and in the vortex-lattice phases exhibit regular patterns of well-defined unit cells.

### Time-dependent simulations

The static tilt protocol is simulated using the two-site variant of the time-dependent variational-principle algorithm [36, 284] after obtaining the ground state in a ladder with open boundaries from a preliminary density-matrix renormalization-group calculation, as described above. For the propagation in time, we employ bond dimensions up to typically 500 and ensure the convergence of all relevant observables by varying the time-step size and the maximum bond dimension independently. Finally, the consistent Hall response, which is independently obtained from either time-dependent quench simulations or ground-state calculations in ring-ladder setups, confirms our results and the feasibility of both approaches.

## 6.7 Summary

We have shown that the Hall voltage  $V_H$  can be consistently calculated in few-leg flux ladders considering finite values of the magnetic flux and employing time-dependent quench protocols with longitudinal and transverse potential gradients. The quench protocols are realistic in state-of-the-art experiments with synthetic quantum matter and a study of the Hall voltage  $V_H$  in ultracold quantum gases might demonstrate its remarkable robustness with respect to the interaction strength  $U$ , the particle filling  $\nu$ , and the ladder geometry in suitable ground-state phases. Furthermore, time-dependent protocols open the exciting possibility to study  $V_H$  in clean and highly tunable optical lattice systems and allow for direct comparison with the Hall voltage measured in solid state devices. A site-resolved analysis of the Hall response in vortex-lattice $_{p/q}$  phases provided insight into characteristic zero crossings of the Hall voltage  $V_H$  at certain values of the magnetic flux  $\phi_{p/q}$ , where competing contributions from particlelike Meissner regions and holelike vortices cancel out. Our numerical results are in good agreement with a semiclassical analysis, which has been discussed in detail. The presented methods are expected to prove useful in future studies of the Hall response in interesting quantum states, such as biased-ladder states [185] and precursors of fractional quantum Hall states [6, 189–192].



## Conclusion and outlook

In this thesis, we studied various aspects of bosonic flux ladders, primarily employing matrix-product-state based simulations. Our studies are motivated by current quantum gas experiments with artificial magnetic fields, which were discussed in Ch. 1. The flux-ladder Hamiltonian as well as observables of interest and important many-body ground-state phases were reviewed in Ch. 2. The results presented throughout this thesis were obtained by means of extensive numerical calculations. The numerical methods were reviewed in Ch. 3. In particular, the density-matrix renormalization-group method was employed for the calculation of ground states. In order to investigate the finite-temperature regime, we implemented a purification approach, which is applicable to canonical setups with a fixed number of particles as well as grand-canonical setups. State-of-the-art time-evolution methods enabled the simulation of quench dynamics in interacting bosonic flux ladders. The main results were presented in Ch. 4, Ch. 5, and Ch. 6.

Ground-state phase diagrams of flux-ladder models have been extensively discussed and mapped out to a large extent in the existing literature. However, in Ch. 4 we put forward new results for model parameters that are specific for a synthetic dimension implementation which is envisioned to be realized by the ultracold quantum gases group at ICFO [2]. Explicitly, the focus was on rungwise  $SU(2)$  symmetric interparticle interactions, a particle filling of one boson per rung, and a specific value of the magnetic flux. We showed that a Mott-insulating Meissner phase as well as biased-ladder phases on top of Mott insulators and superfluids are stabilized for different hopping strengths and interparticle interaction strengths that are accessible in the future experiment. Most importantly, for suitably chosen initial states, we showed that the equilibrium properties of these ground-state phases can be probed in the transient dynamics induced by feasible quantum quenches. In particular, for the Meissner phase, the instantaneous turning on of leg hopping in a rung-localized initial state induces a transient chiral current which exhibits a similar dependence on the model parameters as the chiral current in the ground state of the corresponding post-quench Hamiltonian. Concentrating on the leg-population imbalance, we showed that an underlying biased-ladder phase leaves clear signatures in the short-time dynamics that are induced by the instantaneous turning on of interleg hopping in an experimentally accessible leg-localized initial state.

Most of the theoretical work on flux ladders so far has concentrated on ground states attained at zero temperature. In Ch. 5, we investigated strongly interacting bosons as well as noninteracting bosons and noninteracting spinless fermions on a

two-leg flux ladder at finite temperatures [3]. A particular focus was on the vortex-to-Meissner crossover, for which we studied experimentally accessible observables, namely the chiral current and momentum-distribution functions. Our main results for strongly interacting bosons were obtained using the matrix-product-state based purification approach. We showed that clearly detectable signatures of an underlying bosonic vortex-liquid phase persist in momentum-distribution functions at finite temperatures. For this, a measure of contrast, which is sensitive to the presence of finite-momentum peaks, was introduced. In view of the notorious difficulty of cooling a quantum gas to low energy densities, our approach might provide guidance for future experiments which are naturally at nonzero temperature.

In Ch. 6, we studied the Hall response of interacting flux ladders [1]. Building up on and extending previous work by Greschner et al. [219], we studied the Hall polarization as well as the Hall voltage in the Meissner phase and in vortex-lattice phases, which emerge at a finite value of the magnetic flux. Considering ring-ladder setups with an additional current-inducing Aharonov-Bohm flux, these quantities can be directly computed in the corresponding ground states. Most interestingly, we presented alternative approaches to the computation of the Hall response, which are based on time-dependent quench simulations in systems with open boundary conditions. The time-dependent protocols were discussed in detail and exemplified for the case of noninteracting fermions. Our main matrix-product-state based results for interacting bosons, which were independently obtained from the ring-ladder approach and time-dependent simulations, are in accordance with a semiclassical description, which is applicable for small but finite interparticle interaction strengths. We showed that in contrast to the Hall polarization, the Hall voltage exhibits a remarkable robustness with respect to the interparticle interaction strength, the particle filling, and the ladder geometry. A site-resolved analysis of the Hall response in vortex-lattice phases provided insight into characteristic zero crossings of the Hall voltage at certain values of the magnetic flux, where competing contributions from particlelike Meissner regions and holelike vortices cancel out. Importantly, the time-dependent protocols allow for the exciting possibility to study the Hall voltage in optical lattice systems. A quantum gas experiment might reveal the remarkable robustness of the Hall voltage.

## Outlook

Here, we touch on follow-up studies which are directly related to the results presented in this thesis.

The possibility of calculating finite-temperature states in interacting flux ladders allows for the extension of various studies focusing on the ground-state physics of the model [3]. The regime of finite interparticle interaction strengths, where the flux-ladder model hosts a panoply of emergent zero-temperature phases, is particularly interesting [186]. It is not clear to which extent characteristic signatures of vortex-lattice phases, such as rung-current correlations, persist at finite temperatures [183, 186]. Also, fingerprints of precursors of fractional quantum Hall states, as for instance in the chiral current, have attracted great interest [189–192]. Hence, it is interesting to study the fate of these currents with the onset of finite temperatures. Moreover, finite-temperature calculations are useful in the context of quantum state-preparation protocols [112, 114, 294]. Time-dependent ramps of Peierls phases in the bosonic two-leg flux-ladder model were recently studied by Wang et al. [207]. In the static case, different configurations of Peierls phases that give rise to the same magnetic flux per plaquette are related by a gauge transformation, describing the same physical situation. But, for a time-dependent ramp of the Peierls phases the different configurations induce different artificial electric forces. It turns out that for an efficient state preparation in the Meissner phase, a ramp in the so-called leg-gauge configuration [186] is optimal. Building up on these ideas by means of the purification approach enables an effective finite-temperature description of the prepared states, allowing for the further characterization of the efficiency of the time-dependent protocols.

Our studies of the synthetic dimension implementation of the flux-ladder model might well be extended to further quantum phases [2]. Of particular interest are particle fillings away from the case of one boson per rung, which was considered in this thesis because it can be most easily realized in the envisioned experiment. Indeed, preliminary results suggest that for a particle filling of one boson per two rungs, the synthetic dimension implementation hosts robust vortex-lattice phases. Hence, in analogy to our studies of the Meissner phase and the biased-ladder phase, it is interesting to investigate how the vortex-lattice phase can be probed in feasible quench protocols.

Most importantly, we expect our new protocols for the calculation of the Hall voltage to prove useful in future studies [1]. Of particular interest is the Hall response in the biased-ladder phase of the two-leg flux ladder [185] and in the precursors of fractional quantum Hall states [6, 189–192], which has not yet been investigated.



## References

- [1] M. Buser, S. Greschner, U. Schollwöck, and T. Giamarchi. *Probing the Hall Voltage in Synthetic Quantum Systems*. Phys. Rev. Lett. **126**, 030501 (2021).
- [2] M. Buser, C. Hubig, U. Schollwöck, L. Tarruell, and F. Heidrich-Meisner. *Interacting bosonic flux ladders with a synthetic dimension: Ground-state phases and quantum quench dynamics*. Phys. Rev. A **102**, 053314 (2020).
- [3] M. Buser, F. Heidrich-Meisner, and U. Schollwöck. *Finite-temperature properties of interacting bosons on a two-leg flux ladder*. Phys. Rev. A **99**, 053601 (2019).
- [4] M. Buser, J. Cerrillo, G. Schaller, and J. Cao. *Initial system-environment correlations via the transfer-tensor method*. Phys. Rev. A **96**, 062122 (2017).
- [5] J. Cerrillo, M. Buser, and T. Brandes. *Nonequilibrium quantum transport coefficients and transient dynamics of full counting statistics in the strong-coupling and non-Markovian regimes*. Phys. Rev. B **94**, 214308 (2016).
- [6] F. A. Palm, M. Buser, J. Léonard, M. Aidelsburger, U. Schollwöck, and F. Grusdt. *Bosonic Pfaffian State in the Hofstadter-Bose-Hubbard Model* (2020), arXiv:2011.02477.
- [7] P. A. M. Dirac. *Quantum mechanics of many-electron systems*. Proc. R. Soc. A **123**, 714–733 (1929).
- [8] P. W. Anderson. *More Is Different*. Science **177**, 393–396 (1972).
- [9] N. Goldenfeld and L. P. Kadanoff. *Simple Lessons from Complexity*. Science **284**, 87–89 (1999).
- [10] R. B. Laughlin and D. Pines. *The Theory of Everything*. Proc. Natl. Acad. Sci. USA **97**, 28–31 (2000).
- [11] J. Kanamori. *Electron Correlation and Ferromagnetism of Transition Metals*. J. Prog. Theor. Phys. **30**, 275–289 (1963).
- [12] M. C. Gutzwiller. *Effect of Correlation on the Ferromagnetism of Transition Metals*. Phys. Rev. Lett. **10**, 159–162 (1963).
- [13] J. Hubbard. *Electron correlations in narrow energy bands*. Proc. R. Soc. A **276**, 238–257 (1963).

- [14] P. W. Anderson. *The Resonating Valence Bond State in  $\text{La}_2\text{CuO}_4$  and Superconductivity*. Science **235**, 1196–1198 (1987).
- [15] I. M. Georgescu, S. Ashhab, and F. Nori. *Quantum simulation*. Rev. Mod. Phys. **86**, 153–185 (2014).
- [16] I. Bloch, J. Dalibard, and W. Zwerger. *Many-Body Physics with Ultracold Gases*. Rev. Mod. Phys. **80**, 885–964 (2008).
- [17] I. Bloch, J. Dalibard, and S. Nascimbène. *Quantum simulations with ultracold quantum gases*. Nat. Phys. **8**, 267–276 (2012).
- [18] C. Gross and I. Bloch. *Quantum simulations with ultracold atoms in optical lattices*. Science **357**, 995–1001 (2017).
- [19] M. Greiner, O. Mandel, T. Esslinger, T. W. Hänsch, and I. Bloch. *Quantum phase transition from a superfluid to a Mott insulator in a gas of ultracold atoms*. Nature (London) **415**, 39–44 (2002).
- [20] K. v. Klitzing, G. Dorda, and M. Pepper. *New Method for High-Accuracy Determination of the Fine-Structure Constant Based on Quantized Hall Resistance*. Phys. Rev. Lett. **45**, 494–497 (1980).
- [21] D. C. Tsui, H. L. Stormer, and A. C. Gossard. *Two-Dimensional Magnetotransport in the Extreme Quantum Limit*. Phys. Rev. Lett. **48**, 1559–1562 (1982).
- [22] D. J. Thouless, M. Kohmoto, M. P. Nightingale, and M. den Nijs. *Quantized Hall Conductance in a Two-Dimensional Periodic Potential*. Phys. Rev. Lett. **49**, 405–408 (1982).
- [23] B. Simon. *Holonomy, the Quantum Adiabatic Theorem, and Berry's Phase*. Phys. Rev. Lett. **51**, 2167–2170 (1983).
- [24] M. V. Berry. *Quantal phase factors accompanying adiabatic changes*. Proc. R. Soc. A **392**, 45–57 (1984).
- [25] R. Peierls. *Zur Theorie des Diamagnetismus von Leitungselektronen*. Z. Phys. **80**, 763–791 (1933).
- [26] D. R. Hofstadter. *Energy levels and wave functions of Bloch electrons in rational and irrational magnetic fields*. Phys. Rev. B **14**, 2239–2249 (1976).

- [27] M. Aidelsburger, M. Atala, S. Nascimbène, S. Trotzky, Y.-A. Chen, and I. Bloch. *Experimental Realization of Strong Effective Magnetic Fields in an Optical Lattice*. Phys. Rev. Lett. **107**, 255301 (2011).
- [28] M. Aidelsburger, M. Atala, M. Lohse, J. T. Barreiro, B. Paredes, and I. Bloch. *Realization of the Hofstadter Hamiltonian with Ultracold Atoms in Optical Lattices*. Phys. Rev. Lett. **111**, 185301 (2013).
- [29] H. Miyake, G. A. Siviloglou, C. J. Kennedy, W. C. Burton, and W. Ketterle. *Realizing the Harper Hamiltonian with Laser-Assisted Tunneling in Optical Lattices*. Phys. Rev. Lett. **111**, 185302 (2013).
- [30] D. Jaksch and P. Zoller. *Creation of effective magnetic fields in optical lattices: the Hofstadter butterfly for cold neutral atoms*. New J. Phys. **5**, 56–56 (2003).
- [31] A. R. Kolovsky. *Creating artificial magnetic fields for cold atoms by photon-assisted tunneling*. Europhys. Lett. **93**, 20003 (2011).
- [32] S. R. White. *Density matrix formulation for quantum renormalization groups*. Phys. Rev. Lett. **69**, 2863–2866 (1992).
- [33] S. R. White. *Density-matrix algorithms for quantum renormalization groups*. Phys. Rev. B **48**, 10345–10356 (1993).
- [34] U. Schollwöck. *The density-matrix renormalization group*. Rev. Mod. Phys. **77**, 259–315 (2005).
- [35] U. Schollwöck. *The density-matrix renormalization group in the age of matrix product states*. Ann. Phys. **326**, 96–192 (2011).
- [36] S. Paeckel, T. Köhler, A. Swoboda, S. R. Manmana, U. Schollwöck, and C. Hubig. *Time-evolution methods for matrix-product states*. Ann. Phys. **411**, 167998 (2019).
- [37] S. Sachdev. *Quantum phase transitions*. Cambridge University Press (2011).
- [38] M. P. A. Fisher, P. B. Weichman, G. Grinstein, and D. S. Fisher. *Boson localization and the superfluid-insulator transition*. Phys. Rev. B **40**, 546–570 (1989).
- [39] D. Jaksch, C. Bruder, J. I. Cirac, C. W. Gardiner, and P. Zoller. *Cold Bosonic Atoms in Optical Lattices*. Phys. Rev. Lett. **81**, 3108–3111 (1998).

- [40] S. Trotzky, L. Pollet, F. Gerbier, U. Schnorrberger, I. Bloch, N. V. Prokof'ev, B. Svistunov, and M. Troyer. *Suppression of the critical temperature for superfluidity near the Mott transition*. Nat. Phys. **6**, 998–1004 (2010).
- [41] L. Pollet. *A review of Monte Carlo simulations for the Bose–Hubbard model with diagonal disorder*. C. R. Phys. **14**, 712–724 (2013).
- [42] J. M. Kosterlitz and D. J. Thouless. *Ordering, metastability and phase transitions in two-dimensional systems*. J. Phys. C **6**, 1181–1203 (1973).
- [43] J. M. Kosterlitz. *The critical properties of the two-dimensional xy model*. J. Phys. C **7**, 1046–1060 (1974).
- [44] T. D. Kühner, S. R. White, and H. Monien. *One-dimensional Bose-Hubbard model with nearest-neighbor interaction*. Phys. Rev. B **61**, 12474–12489 (2000).
- [45] F. D. M. Haldane. *Nobel Lecture: Topological quantum matter*. Rev. Mod. Phys. **89**, 040502 (2017).
- [46] F. D. M. Haldane. *Ground State Properties of Antiferromagnetic Chains with Unrestricted Spin: Integer Spin Chains as Realisations of the  $O(3)$  Non-Linear Sigma Model* (2016), arXiv:1612.00076.
- [47] F. D. M. Haldane. *Continuum dynamics of the 1-D Heisenberg antiferromagnet: Identification with the  $O(3)$  nonlinear sigma model*. Phys. Lett. A **93**, 464–468 (1983).
- [48] F. D. M. Haldane. *Nonlinear Field Theory of Large-Spin Heisenberg Antiferromagnets: Semiclassically Quantized Solitons of the One-Dimensional Easy-Axis Néel State*. Phys. Rev. Lett. **50**, 1153–1156 (1983).
- [49] R. B. Laughlin. *Anomalous Quantum Hall Effect: An Incompressible Quantum Fluid with Fractionally Charged Excitations*. Phys. Rev. Lett. **50**, 1395–1398 (1983).
- [50] A. Y. Kitaev. *Fault-tolerant quantum computation by anyons*. Ann. Phys. **303**, 2–30 (2003).
- [51] C. Nayak, S. H. Simon, A. Stern, M. Freedman, and S. Das Sarma. *Non-Abelian anyons and topological quantum computation*. Rev. Mod. Phys. **80**, 1083–1159 (2008).
- [52] F. D. M. Haldane. *Model for a Quantum Hall Effect without Landau Levels: Condensed-Matter Realization of the "Parity Anomaly"*. Phys. Rev. Lett. **61**, 2015–2018 (1988).

- [53] S. Ryu, A. P. Schnyder, A. Furusaki, and A. W. Ludwig. *Topological insulators and superconductors: tenfold way and dimensional hierarchy*. *New J. Phys.* **12**, 065010 (2010).
- [54] C. L. Kane and E. J. Mele. *Quantum Spin Hall Effect in Graphene*. *Phys. Rev. Lett.* **95**, 226801 (2005).
- [55] C. L. Kane and E. J. Mele. *Z<sub>2</sub> Topological Order and the Quantum Spin Hall Effect*. *Phys. Rev. Lett.* **95**, 146802 (2005).
- [56] M. König, S. Wiedmann, C. Brüne, A. Roth, H. Buhmann, L. W. Molenkamp, X.-L. Qi, and S.-C. Zhang. *Quantum Spin Hall Insulator State in HgTe Quantum Wells*. *Science* **318**, 766–770 (2007).
- [57] X. Chen, Z.-C. Gu, Z.-X. Liu, and X.-G. Wen. *Symmetry protected topological orders and the group cohomology of their symmetry group*. *Phys. Rev. B* **87**, 155114 (2013).
- [58] F. Pollmann, A. M. Turner, E. Berg, and M. Oshikawa. *Entanglement spectrum of a topological phase in one dimension*. *Phys. Rev. B* **81**, 064439 (2010).
- [59] X. Chen, Z.-C. Gu, and X.-G. Wen. *Classification of gapped symmetric phases in one-dimensional spin systems*. *Phys. Rev. B* **83**, 035107 (2011).
- [60] F. Pollmann, E. Berg, A. M. Turner, and M. Oshikawa. *Symmetry protection of topological phases in one-dimensional quantum spin systems*. *Phys. Rev. B* **85**, 075125 (2012).
- [61] I. Affleck, T. Kennedy, E. H. Lieb, and H. Tasaki. *Rigorous results on valence-bond ground states in antiferromagnets*. *Phys. Rev. Lett.* **59**, 799–802 (1987).
- [62] I. Affleck, T. Kennedy, E. H. Lieb, and H. Tasaki. *Valence bond ground states in isotropic quantum antiferromagnets*. *Comm. Math. Phys.* **115**, 477 (1988).
- [63] X. Chen, Z.-C. Gu, and X.-G. Wen. *Local unitary transformation, long-range quantum entanglement, wave function renormalization, and topological order*. *Phys. Rev. B* **82**, 155138 (2010).
- [64] D. Hügél and B. Paredes. *Chiral ladders and the edges of quantum Hall insulators*. *Phys. Rev. A* **89**, 023619 (2014).
- [65] R. P. Feynman. *Simulating physics with computers*. *Int. J. Theor. Phys.* **21**, 467 (1982).

- [66] S. Lloyd. *Universal Quantum Simulators*. *Science* **273**, 1073–1078 (1996).
- [67] I. Buluta and F. Nori. *Quantum Simulators*. *Science* **326**, 108–111 (2009).
- [68] J. I. Cirac and P. Zoller. *Goals and opportunities in quantum simulation*. *Nat. Phys.* **8**, 264–266 (2012).
- [69] E. Altman, K. R. Brown, G. Carleo, L. D. Carr, E. Demler, C. Chin, B. DeMarco, S. E. Economou, M. A. Eriksson, K.-M. C. Fu, M. Greiner, et al. *Quantum Simulators: Architectures and Opportunities* (2019), arXiv:1912.06938.
- [70] J. Preskill. *Quantum computing and the entanglement frontier* (2012), arXiv:1203.5813.
- [71] J. Preskill. *Quantum Computing in the NISQ era and beyond*. *Quantum* **2**, 79 (2018).
- [72] F. Arute, K. Arya, R. Babbush, et al. *Quantum supremacy using a programmable superconducting processor*. *Nature (London)* **574**, 505–510 (2019).
- [73] H.-S. Zhong, H. Wang, Y.-H. Deng, M.-C. Chen, L.-C. Peng, Y.-H. Luo, J. Qin, D. Wu, X. Ding, Y. Hu, P. Hu, X.-Y. Yang, W.-J. Zhang, H. Li, Y. Li, X. Jiang, L. Gan, G. Yang, L. You, Z. Wang, L. Li, N.-L. Liu, C.-Y. Lu, and J.-W. Pan. *Quantum computational advantage using photons*. *Science* **370**, 1460–1463 (2020).
- [74] S. Aaronson and A. Arkhipov. *The Computational Complexity of Linear Optics*. *Theory of Computing* **9**, 143–252 (2013).
- [75] A. P. Lund, M. J. Bremner, and T. C. Ralph. *Quantum sampling problems, BosonSampling and quantum supremacy*. *npj Quantum Inf.* **3**, 1–8 (2017).
- [76] S. Boixo, S. V. Isakov, V. N. Smelyanskiy, R. Babbush, N. Ding, Z. Jiang, M. J. Bremner, J. M. Martinis, and H. Neven. *Characterizing quantum supremacy in near-term devices*. *Nat. Phys.* **14**, 595–600 (2018).
- [77] E. Pednault, J. A. Gunnels, G. Nannicini, L. Horesh, and R. Wisnieff. *Leveraging Secondary Storage to Simulate Deep 54-qubit Sycamore Circuits* (2019), arXiv:1910.09534.
- [78] Y. Zhou, E. M. Stoudenmire, and X. Waintal. *What limits the simulation of quantum computers?* *Phys. Rev. X* **10**, 041038 (2020).
- [79] M. A. Broome, A. Fedrizzi, S. Rahimi-Keshari, J. Dove, S. Aaronson, T. C. Ralph, and A. G. White. *Photonic Boson Sampling in a Tunable Circuit*. *Science* **339**, 794–798 (2013).

- [80] J. B. Spring, B. J. Metcalf, P. C. Humphreys, W. S. Kolthammer, X.-M. Jin, M. Barbieri, A. Datta, N. Thomas-Peter, N. K. Langford, D. Kundys, J. C. Gates, B. J. Smith, P. G. R. Smith, and I. A. Walmsley. *Boson sampling on a photonic chip*. *Science* **339**, 798–801 (2013).
- [81] H. Wang, J. Qin, X. Ding, M.-C. Chen, S. Chen, X. You, Y.-M. He, X. Jiang, L. You, Z. Wang, C. Schneider, J. J. Renema, S. Höfling, C.-Y. Lu, and J.-W. Pan. *Boson Sampling with 20 Input Photons and a 60-Mode Interferometer in a  $10^{14}$ -Dimensional Hilbert Space*. *Phys. Rev. Lett.* **123**, 250503 (2019).
- [82] Y. Li, M. Chen, Y. Chen, H. Lu, L. Gan, C. Lu, J. Pan, H. Fu, and G. Yang. *Benchmarking 50-Photon Gaussian Boson Sampling on the Sunway TaihuLight* (2020), arXiv:2009.01177.
- [83] F. Arute, K. Arya, R. Babbush, D. Bacon, J. C. Bardin, R. Barends, S. Boixo, M. Broughton, B. B. Buckley, D. A. Buell, et al. *Hartree-fock on a superconducting qubit quantum computer*. *Science* **369**, 1084–1089 (2020).
- [84] A. W. Sandvik. *Computational Studies of Quantum Spin Systems*. AIP Conf. Proc. **1297**, 135 (2010).
- [85] H. Q. Lin. *Exact diagonalization of quantum-spin models*. *Phys. Rev. B* **42**, 6561–6567 (1990).
- [86] L. Pollet. *Recent developments in quantum Monte Carlo simulations with applications for cold gases*. *Rep. Prog. Phys.* **75**, 094501 (2012).
- [87] J. Eisert. *Entanglement and tensor network states* (2013), arXiv:1308.3318.
- [88] M. A. Nielsen and I. L. Chuang. *Quantum Computation and Quantum Information*. Cambridge University Press (2010).
- [89] S. Trotzky, Y.-A. Chen, A. Flesch, I. P. McCulloch, U. Schollwöck, J. Eisert, and I. Bloch. *Probing the relaxation towards equilibrium in an isolated strongly correlated one-dimensional Bose gas*. *Nat. Phys.* **8**, 325–330 (2012).
- [90] S. Krinner, T. Esslinger, and J.-P. Brantut. *Two-terminal transport measurements with cold atoms*. *J. Phys. Condens. Matter* **29**, 343003 (2017).
- [91] D. J. Gorman, B. Hemmerling, E. Megidish, S. A. Moeller, P. Schindler, M. Sarovar, and H. Haefner. *Engineering Vibrationally Assisted Energy Transfer in a Trapped-Ion Quantum Simulator*. *Phys. Rev. X* **8**, 011038 (2018).

- [92] D. Loss and D. P. DiVincenzo. *Quantum computation with quantum dots*. Phys. Rev. A **57**, 120–126 (1998).
- [93] R. Grimm, M. Weidemüller, and Y. B. Ovchinnikov. *Optical dipole traps for neutral atoms*. Adv. At. Mol. Opt. Phys. **42**, 95 (2000).
- [94] M. Greiner, I. Bloch, O. Mandel, T. W. Hänsch, and T. Esslinger. *Exploring Phase Coherence in a 2D Lattice of Bose-Einstein Condensates*. Phys. Rev. Lett. **87**, 160405 (2001).
- [95] L. Tarruell, D. Greif, T. Uehlinger, G. Jotzu, and T. Esslinger. *Creating, moving and merging Dirac points with a Fermi gas in a tunable honeycomb lattice*. Nature (London) **483**, 302–305 (2012).
- [96] G.-B. Jo, J. Guzman, C. K. Thomas, P. Hosur, A. Vishwanath, and D. M. Stamper-Kurn. *Ultracold Atoms in a Tunable Optical Kagome Lattice*. Phys. Rev. Lett. **108**, 045305 (2012).
- [97] S. Fölling, S. Trotzky, P. Cheinet, M. Feld, R. Saers, A. Widera, T. Müller, and I. Bloch. *Direct observation of second-order atom tunnelling*. Nature (London) **448**, 1029–1032 (2007).
- [98] C. Chin, R. Grimm, P. Julienne, and E. Tiesinga. *Feshbach resonances in ultracold gases*. Rev. Mod. Phys. **82**, 1225–1286 (2010).
- [99] E. A. Cornell and C. E. Wieman. *Nobel Lecture: Bose-Einstein condensation in a dilute gas, the first 70 years and some recent experiments*. Rev. Mod. Phys. **74**, 875–893 (2002).
- [100] W. Ketterle. *Nobel lecture: When atoms behave as waves: Bose-Einstein condensation and the atom laser*. Rev. Mod. Phys. **74**, 1131–1151 (2002).
- [101] W. S. Bakr, J. I. Gillen, A. Peng, S. Fölling, and M. Greiner. *A quantum gas microscope for detecting single atoms in a Hubbard-regime optical lattice*. Nature (London) **462**, 74–77 (2009).
- [102] J. F. Sherson, C. Weitenberg, M. Endres, M. Cheneau, I. Bloch, and S. Kuhr. *Single-atom-resolved fluorescence imaging of an atomic Mott insulator*. Nature (London) **467**, 68–72 (2010).
- [103] C. Weitenberg, M. Endres, J. F. Sherson, M. Cheneau, P. Schauß, T. Fukuhara, I. Bloch, and S. Kuhr. *Single-spin addressing in an atomic Mott insulator*. Nature (London) **471**, 319–324 (2011).

- [104] T. Fukuhara, A. Kantian, M. Endres, M. Cheneau, P. Schauß, S. Hild, D. Bellem, U. Schollwöck, T. Giamarchi, C. Gross, I. Bloch, and S. Kuhr. *Quantum dynamics of a mobile spin impurity*. Nat. Phys. **9**, 235–241 (2013).
- [105] P. Zupancic, P. M. Preiss, R. Ma, A. Lukin, M. E. Tai, M. Rispoli, R. Islam, and M. Greiner. *Ultra-precise holographic beam shaping for microscopic quantum control*. Opt. Express **24**, 13881–13893 (2016).
- [106] C. S. Chiu, G. Ji, A. Bohrdt, M. Xu, M. Knap, E. Demler, F. Grusdt, M. Greiner, and D. Greif. *String patterns in the doped Hubbard model*. Science **365**, 251–256 (2019).
- [107] B. S. Rem, N. Käming, M. Tarnowski, L. Asteria, N. Fläschner, C. Becker, K. Sengstock, and C. Weitenberg. *Identifying quantum phase transitions using artificial neural networks on experimental data*. Nat. Phys. **15**, 917–920 (2019).
- [108] A. Bohrdt, C. S. Chiu, G. Ji, M. Xu, D. Greif, M. Greiner, E. Demler, F. Grusdt, and M. Knap. *Classifying snapshots of the doped Hubbard model with machine learning*. Nat. Phys. **15**, 921–924 (2019).
- [109] C. Miles, A. Bohrdt, R. Wu, C. Chiu, M. Xu, G. Ji, M. Greiner, K. Q. Weinberger, E. Demler, and E.-A. Kim. *Correlator Convolutional Neural Networks: An Interpretable Architecture for Image-like Quantum Matter Data* (2020), arXiv:2011.03474.
- [110] A. Bohrdt, S. Kim, A. Lukin, M. Rispoli, R. Schittko, M. Knap, M. Greiner, and J. Léonard. *Analyzing non-equilibrium quantum states through snapshots with artificial neural networks* (2020), arXiv:2012.11586.
- [111] T. Langen, R. Geiger, M. Kuhnert, B. Rauer, and J. Schmiedmayer. *Local emergence of thermal correlations in an isolated quantum many-body system*. Nat. Phys. **9**, 640–643 (2013).
- [112] T. Langen, R. Geiger, and J. Schmiedmayer. *Ultracold atoms out of equilibrium*. Annu. Rev. Condens. Matter Phys. **6**, 201–217 (2015).
- [113] A. M. Kaufman, M. E. Tai, A. Lukin, M. Rispoli, R. Schittko, P. M. Preiss, and M. Greiner. *Quantum thermalization through entanglement in an isolated many-body system*. Science **353**, 794–800 (2016).
- [114] J. Eisert, M. Friesdorf, and C. Gogolin. *Quantum many-body systems out of equilibrium*. Nat. Phys. **11**, 124–130 (2015).

- [115] L. D'Alessio, Y. Kafri, A. Polkovnikov, and M. Rigol. *From quantum chaos and eigenstate thermalization to statistical mechanics and thermodynamics*. Adv. Phys. **65**, 239–362 (2016).
- [116] D. A. Abanin, E. Altman, I. Bloch, and M. Serbyn. *Colloquium: Many-body localization, thermalization, and entanglement*. Rev. Mod. Phys. **91**, 021001 (2019).
- [117] J. M. Deutsch. *Quantum statistical mechanics in a closed system*. Phys. Rev. A **43**, 2046–2049 (1991).
- [118] M. Srednicki. *Chaos and quantum thermalization*. Phys. Rev. E **50**, 888–901 (1994).
- [119] M. Schreiber, S. S. Hodgman, P. Bordia, H. P. Lüschen, M. H. Fischer, R. Vosk, E. Altman, U. Schneider, and I. Bloch. *Observation of many-body localization of interacting fermions in a quasirandom optical lattice*. Science **349**, 842–845 (2015).
- [120] S. Scherg, T. Kohlert, P. Sala, F. Pollmann, H. M. Bharath, I. Bloch, and M. Aidelsburger. *Observing non-ergodicity due to kinetic constraints in tilted Fermi-Hubbard chains* (2020), arXiv:2010.12965.
- [121] N. R. Cooper, J. Dalibard, and I. B. Spielman. *Topological bands for ultracold atoms*. Rev. Mod. Phys. **91**, 015005 (2019).
- [122] M. Aidelsburger, S. Nascimbène, and N. Goldman. *Artificial gauge fields in materials and engineered systems*. C. R. Phys. **19**, 394–432 (2018).
- [123] N. Goldman, J. C. Budich, and P. Zoller. *Topological quantum matter with ultracold gases in optical lattices*. Nat. Phys. **12**, 639–645 (2016).
- [124] N. Goldman, G. Juzeliūnas, P. Öhberg, and I. B. Spielman. *Light-induced gauge fields for ultracold atoms*. Rep. Prog. Phys. **77**, 126401 (2014).
- [125] V. Galitski and I. B. Spielman. *Spin-orbit coupling in quantum gases*. Nature (London) **494**, 49–54 (2013).
- [126] J. Dalibard, F. Gerbier, G. Juzeliūnas, and P. Öhberg. *Colloquium: Artificial gauge potentials for neutral atoms*. Rev. Mod. Phys. **83**, 1523–1543 (2011).
- [127] P. Roushan, C. Neill, A. Megrant, Y. Chen, R. Babbush, R. Barends, B. Campbell, Z. Chen, B. Chiaro, A. Dunsworth, et al. *Chiral ground-state currents of interacting photons in a synthetic magnetic field*. Nat. Phys. **13**, 146–151 (2017).

- [128] P. Roushan, C. Neill, J. Tangpanitanon, V. M. Bastidas, A. Megrant, R. Barends, Y. Chen, Z. Chen, B. Chiaro, A. Dunsworth, et al. *Spectroscopic signatures of localization with interacting photons in superconducting qubits*. *Science* **358**, 1175–1179 (2017).
- [129] Z. Wang, Y. Chong, J. D. Joannopoulos, and M. Soljačić. *Observation of unidirectional backscattering-immune topological electromagnetic states*. *Nature (London)* **461**, 772–775 (2009).
- [130] K. Fang, Z. Yu, and S. Fan. *Experimental demonstration of a photonic Aharonov-Bohm effect at radio frequencies*. *Phys. Rev. B* **87**, 060301 (2013).
- [131] J. Ningyuan, C. Owens, A. Sommer, D. Schuster, and J. Simon. *Time- and Site-Resolved Dynamics in a Topological Circuit*. *Phys. Rev. X* **5**, 021031 (2015).
- [132] C. Owens, A. LaChapelle, B. Saxberg, B. M. Anderson, R. Ma, J. Simon, and D. I. Schuster. *Quarter-flux Hofstadter lattice in a qubit-compatible microwave cavity array*. *Phys. Rev. A* **97**, 013818 (2018).
- [133] Y.-J. Lin, R. L. Compton, A. R. Perry, W. D. Phillips, J. V. Porto, and I. B. Spielman. *Bose-Einstein Condensate in a Uniform Light-Induced Vector Potential*. *Phys. Rev. Lett.* **102**, 130401 (2009).
- [134] Y.-J. Lin, R. L. Compton, K. Jimenez-Garcia, J. V. Porto, and I. B. Spielman. *Synthetic magnetic fields for ultracold neutral atoms*. *Nature (London)* **462**, 628–632 (2009).
- [135] J. Struck, C. Ölschläger, M. Weinberg, P. Hauke, J. Simonet, A. Eckardt, M. Lewenstein, K. Sengstock, and P. Windpassinger. *Tunable Gauge Potential for Neutral and Spinless Particles in Driven Optical Lattices*. *Phys. Rev. Lett.* **108**, 225304 (2012).
- [136] M. Atala, M. Aidelsburger, M. Lohse, J. T. Barreiro, B. Paredes, and I. Bloch. *Observation of chiral currents with ultracold atoms in bosonic ladders*. *Nat. Phys.* **10**, 588–593 (2014).
- [137] G. Jotzu, M. Messer, R. Desbuquois, M. Lebrat, T. Uehlinger, D. Greif, and T. Esslinger. *Experimental realization of the topological Haldane model with ultracold fermions*. *Nature (London)* **515**, 237–240 (2014).
- [138] M. Aidelsburger, M. Lohse, C. Schweizer, M. Atala, J. Barreiro, S. Nascimbène, N. Cooper, I. Bloch, and N. Goldman. *Observation of chiral currents with ultracold atoms in bosonic ladders*. *Nat. Phys.* **11**, 162–166 (2015).

- [139] B. Stuhl, H.-I. Lu, L. Aycocock, D. Genkina, and I. Spielman. *Visualizing edge states with an atomic Bose gas in the quantum Hall regime*. *Science* **349**, 1514–1518 (2015).
- [140] M. Mancini, G. Pagano, G. Cappellini, L. Livi, M. Rider, J. Catani, C. Sias, P. Zoller, M. Inguscio, M. Dalmonte, and L. Fallani. *Observation of chiral edge states with neutral fermions in synthetic Hall ribbons*. *Science* **349**, 1510–1513 (2015).
- [141] L. F. Livi, G. Cappellini, M. Diem, L. Franchi, C. Clivati, M. Frittelli, F. Levi, D. Calonico, J. Catani, M. Inguscio, and L. Fallani. *Synthetic Dimensions and Spin-Orbit Coupling with an Optical Clock Transition*. *Phys. Rev. Lett.* **117**, 220401 (2016).
- [142] N. Fläschner, B. S. Rem, M. Tarnowski, D. Vogel, D.-S. Lühmann, K. Sengstock, and C. Weitenberg. *Experimental Reconstruction of the Berry Curvature in a Floquet Bloch Band*. *Science* **352**, 1091–1094 (2016).
- [143] F. A. An, E. J. Meier, and B. Gadway. *Direct observation of chiral currents and magnetic reflection in atomic flux lattices*. *Sci. Adv.* **3**, e1602685 (2017).
- [144] M. E. Tai, A. Lukin, M. Rispoli, R. Schittko, T. Menke, D. Borgnia, P. M. Preiss, F. Grusdt, A. M. Kaufman, and M. Greiner. *Microscopy of the interacting Harper–Hofstadter model in the two-body limit*. *Nature (London)* **546**, 519–523 (2017).
- [145] S. Kolkowitz, S. L. Bromley, T. Bothwell, M. L. Wall, G. E. Marti, A. P. Koller, X. Zhang, A. M. Rey, and J. Ye. *Spin–orbit-coupled fermions in an optical lattice clock*. *Nature (London)* **542**, 66–70 (2017).
- [146] J. H. Kang, J. H. Han, and Y. Shin. *Realization of a Cross-Linked Chiral Ladder with Neutral Fermions in a 1D Optical Lattice by Orbital-Momentum Coupling*. *Phys. Rev. Lett.* **121**, 150403 (2018).
- [147] F. A. An, E. J. Meier, and B. Gadway. *Engineering a Flux-Dependent Mobility Edge in Disordered Zigzag Chains*. *Phys. Rev. X* **8**, 031045 (2018).
- [148] J. H. Han, J. H. Kang, and Y. Shin. *Band Gap Closing in a Synthetic Hall Tube of Neutral Fermions*. *Phys. Rev. Lett.* **122**, 065303 (2019).
- [149] D. Genkina, L. M. Aycocock, H.-I. Lu, M. Lu, A. M. Pineiro, and I. B. Spielman. *Imaging topology of Hofstadter ribbons*. *New J. Phys.* **21**, 053021 (2019).
- [150] L. Asteria, D. T. Tran, T. Ozawa, M. Tarnowski, B. S. Rem, N. Fläschner, K. Sengstock, N. Goldman, and C. Weitenberg. *Measuring quantized circular dichroism in ultracold topological matter*. *Nat. Phys.* **15**, 449–454 (2019).

- [151] T. Chalopin, T. Satoor, A. Evrard, V. Makhalov, J. Dalibard, R. Lopes, and S. Nascimbène. *Probing chiral edge dynamics and bulk topology of a synthetic Hall system*. Nat. Phys. **16**, 1017–1021 (2020).
- [152] M. Bukov, L. D’Alessio, and A. Polkovnikov. *Universal high-frequency behavior of periodically driven systems: from dynamical stabilization to Floquet engineering*. Adv. Phys. **64**, 139–226 (2015).
- [153] A. Eckardt. *Colloquium: Atomic quantum gases in periodically driven optical lattices*. Rev. Mod. Phys. **89**, 011004 (2017).
- [154] J. H. Shirley. *Solution of the Schrödinger Equation with a Hamiltonian Periodic in Time*. Phys. Rev. **138**, B979–B987 (1965).
- [155] A. Rubio-Abadal, M. Ippoliti, S. Hollerith, D. Wei, J. Rui, S. L. Sondhi, V. Khemani, C. Gross, and I. Bloch. *Floquet Prethermalization in a Bose-Hubbard System*. Phys. Rev. X **10**, 021044 (2020).
- [156] K. Viebahn, J. Minguzzi, K. Sandholzer, A.-S. Walter, F. Görg, and T. Esslinger. *Suppressing dissipation in a Floquet-Hubbard system* (2020), arXiv:2003.05937.
- [157] K. Wintersperger, M. Bukov, J. Näger, S. Lellouch, E. Demler, U. Schneider, I. Bloch, N. Goldman, and M. Aidelsburger. *Parametric Instabilities of Interacting Bosons in Periodically Driven 1D Optical Lattices*. Phys. Rev. X **10**, 011030 (2020).
- [158] K. Singh, C. J. Fujiwara, Z. A. Geiger, E. Q. Simmons, M. Lipatov, A. Cao, P. Dotti, S. V. Rajagopal, R. Senaratne, T. Shimasaki, M. Heyl, A. Eckardt, and D. M. Weld. *Quantifying and Controlling Prethermal Nonergodicity in Interacting Floquet Matter*. Phys. Rev. X **9**, 041021 (2019).
- [159] T. Boulier, J. Maslek, M. Bukov, C. Bracamontes, E. Magnan, S. Lellouch, E. Demler, N. Goldman, and J. V. Porto. *Parametric Heating in a 2D Periodically Driven Bosonic System: Beyond the Weakly Interacting Regime*. Phys. Rev. X **9**, 011047 (2019).
- [160] M. Messer, K. Sandholzer, F. Görg, J. Minguzzi, R. Desbuquois, and T. Esslinger. *Floquet Dynamics in Driven Fermi-Hubbard Systems*. Phys. Rev. Lett. **121**, 233603 (2018).
- [161] M. Reitter, J. Näger, K. Wintersperger, C. Sträter, I. Bloch, A. Eckardt, and U. Schneider. *Interaction Dependent Heating and Atom Loss in a Periodically Driven Optical Lattice*. Phys. Rev. Lett. **119**, 200402 (2017).

- [162] M. Weinberg, C. Ölschläger, C. Sträter, S. Prella, A. Eckardt, K. Sengstock, and J. Simonet. *Multiphoton interband excitations of quantum gases in driven optical lattices*. Phys. Rev. A **92**, 043621 (2015).
- [163] G. Sun and A. Eckardt. *Optimal frequency window for Floquet engineering in optical lattices*. Phys. Rev. Research **2**, 013241 (2020).
- [164] D. A. Abanin, W. De Roeck, and F. Huveneers. *Exponentially Slow Heating in Periodically Driven Many-Body Systems*. Phys. Rev. Lett. **115**, 256803 (2015).
- [165] L. D'Alessio and M. Rigol. *Long-time Behavior of Isolated Periodically Driven Interacting Lattice Systems*. Phys. Rev. X **4**, 041048 (2014).
- [166] P. Bordia, H. Lüschen, U. Schneider, M. Knap, and I. Bloch. *Periodically driving a many-body localized quantum system*. Nat. Phys. **13**, 460–464 (2017).
- [167] A. Eckardt, C. Weiss, and M. Holthaus. *Superfluid-insulator transition in a periodically driven optical lattice*. Phys. Rev. Lett. **95**, 260404 (2005).
- [168] A. Zenesini, H. Lignier, D. Ciampini, O. Morsch, and E. Arimondo. *Coherent Control of Dressed Matter Waves*. Phys. Rev. Lett. **102**, 100403 (2009).
- [169] H. Lignier, C. Sias, D. Ciampini, Y. Singh, A. Zenesini, O. Morsch, and E. Arimondo. *Dynamical Control of Matter-Wave Tunneling in Periodic Potentials*. Phys. Rev. Lett. **99**, 220403 (2007).
- [170] D. H. Dunlap and V. M. Kenkre. *Dynamic localization of a charged particle moving under the influence of an electric field*. Phys. Rev. B **34**, 3625–3633 (1986).
- [171] E. Dagotto and T. M. Rice. *Surprises on the Way from One- to Two-Dimensional Quantum Magnets: The Ladder Materials*. Science **271**, 618–623 (1996).
- [172] A. Celi, P. Massignan, J. Ruseckas, N. Goldman, I. B. Spielman, G. Juzeliūnas, and M. Lewenstein. *Synthetic Gauge Fields in Synthetic Dimensions*. Phys. Rev. Lett. **112**, 043001 (2014).
- [173] O. Boada, A. Celi, J. Rodríguez-Laguna, J. I. Latorre, and M. Lewenstein. *Quantum simulation of non-trivial topology*. New J. Phys. **17**, 045007 (2015).
- [174] S. Mugel, A. Dauphin, P. Massignan, L. Tarruell, M. Lewenstein, C. Lobo, and A. Celi. *Measuring Chern numbers in Hofstadter strips*. SciPost Phys. **3**, 012 (2017).

- [175] M. Kardar. *Josephson-junction ladders and quantum fluctuations*. Phys. Rev. B **33**, 3125–3128 (1986).
- [176] E. Granato. *Phase transitions in josephson-junction ladders in a magnetic field*. Phys. Rev. B **42**, 4797–4799 (1990).
- [177] J. J. Mazo, F. Falo, and L. M. Floría. *Josephson junction ladders: Ground state and relaxation phenomena*. Phys. Rev. B **52**, 10433–10440 (1995).
- [178] C. Denniston and C. Tang. *Phases of Josephson Junction Ladders*. Phys. Rev. Lett. **75**, 3930–3933 (1995).
- [179] E. Orignac and T. Giamarchi. *Meissner effect in a bosonic ladder*. Phys. Rev. B **64**, 144515 (2001).
- [180] A. Dhar, M. Maji, T. Mishra, R. V. Pai, S. Mukerjee, and A. Paramekanti. *Bose-Hubbard model in a strong effective magnetic field: Emergence of a chiral Mott insulator ground state*. Phys. Rev. A **85**, 041602 (2012).
- [181] A. Dhar, T. Mishra, M. Maji, R. V. Pai, S. Mukerjee, and A. Paramekanti. *Chiral Mott insulator with staggered loop currents in the fully frustrated Bose-Hubbard model*. Phys. Rev. B **87**, 174501 (2013).
- [182] A. Petrescu and K. Le Hur. *Bosonic Mott Insulator with Meissner Currents*. Phys. Rev. Lett. **111**, 150601 (2013).
- [183] S. Greschner, M. Piraud, F. Heidrich-Meisner, I. P. McCulloch, U. Schollwöck, and T. Vekua. *Spontaneous Increase of Magnetic Flux and Chiral-Current Reversal in Bosonic Ladders: Swimming against the Tide*. Phys. Rev. Lett. **115**, 190402 (2015).
- [184] M. Piraud, F. Heidrich-Meisner, I. P. McCulloch, S. Greschner, T. Vekua, and U. Schollwöck. *Vortex and Meissner phases of strongly interacting bosons on a two-leg ladder*. Phys. Rev. B **91**, 140406 (2015).
- [185] R. Wei and E. J. Mueller. *Theory of bosons in two-leg ladders with large magnetic fields*. Phys. Rev. A **89**, 063617 (2014).
- [186] S. Greschner, M. Piraud, F. Heidrich-Meisner, I. P. McCulloch, U. Schollwöck, and T. Vekua. *Symmetry-broken states in a system of interacting bosons on a two-leg ladder with a uniform Abelian gauge field*. Phys. Rev. A **94**, 063628 (2016).

- [187] S. Greschner and T. Vekua. *Vortex-Hole Duality: A Unified Picture of Weak- and Strong-Coupling Regimes of Bosonic Ladders with Flux*. Phys. Rev. Lett. **119**, 073401 (2017).
- [188] F. Grusdt and M. Höning. *Realization of fractional Chern insulators in the thin-torus limit with ultracold bosons*. Phys. Rev. A **90**, 053623 (2014).
- [189] A. Petrescu and K. Le Hur. *Chiral Mott insulators, Meissner effect, and Laughlin states in quantum ladders*. Phys. Rev. B **91**, 054520 (2015).
- [190] E. Cornfeld and E. Sela. *Chiral currents in one-dimensional fractional quantum Hall states*. Phys. Rev. B **92**, 115446 (2015).
- [191] A. Petrescu, M. Piraud, G. Roux, I. P. McCulloch, and K. Le Hur. *Precursor of the Laughlin state of hard-core bosons on a two-leg ladder*. Phys. Rev. B **96**, 014524 (2017).
- [192] M. Calvanese Strinati, E. Cornfeld, D. Rossini, S. Barbarino, M. Dalmonte, R. Fazio, E. Sela, and L. Mazza. *Laughlin-like States in Bosonic and Fermionic Atomic Synthetic Ladders*. Phys. Rev. X **7**, 021033 (2017).
- [193] M. Calvanese Strinati, S. Sahoo, K. Shtengel, and E. Sela. *Pretopological fractional excitations in the two-leg flux ladder*. Phys. Rev. B **99**, 245101 (2019).
- [194] S. T. Carr, B. N. Narozhny, and A. A. Nersesyan. *Spinless fermionic ladders in a magnetic field: Phase diagram*. Phys. Rev. B **73**, 195114 (2006).
- [195] G. Roux, E. Orignac, S. R. White, and D. Poilblanc. *Diamagnetism of doped two-leg ladders and probing the nature of their commensurate phases*. Phys. Rev. B **76**, 195105 (2007).
- [196] A. Tokuno and A. Georges. *Ground states of a Bose–Hubbard ladder in an artificial magnetic field: Field-theoretical approach*. New J. Phys. **16**, 073005 (2014).
- [197] M. Di Dio, S. De Palo, E. Orignac, R. Citro, and M.-L. Chiofalo. *Persisting Meissner state and incommensurate phases of hard-core boson ladders in a flux*. Phys. Rev. B **92**, 060506 (2015).
- [198] S. Uchino and A. Tokuno. *Population-imbalance instability in a Bose-Hubbard ladder in the presence of a magnetic flux*. Phys. Rev. A **92**, 013625 (2015).
- [199] S. Uchino. *Analytical approach to a bosonic ladder subject to a magnetic field*. Phys. Rev. A **93**, 053629 (2016).

- [200] T. Bilitewski and N. R. Cooper. *Synthetic dimensions in the strong-coupling limit: Supersolids and pair superfluids*. Phys. Rev. A **94**, 023630 (2016).
- [201] E. Orignac, R. Citro, M. D. Dio, S. D. Palo, and M.-L. Chiofalo. *Incommensurate phases of a bosonic two-leg ladder under a flux*. New J. Phys. **18**, 055017 (2016).
- [202] E. Orignac, R. Citro, M. Di Dio, and S. De Palo. *Vortex lattice melting in a boson ladder in an artificial gauge field*. Phys. Rev. B **96**, 014518 (2017).
- [203] D. Hügél, H. U. R. Strand, P. Werner, and L. Pollet. *Anisotropic Harper-Hofstadter-Mott model: Competition between condensation and magnetic fields*. Phys. Rev. B **96**, 054431 (2017).
- [204] R. Citro, S. De Palo, M. Di Dio, and E. Orignac. *Quantum phase transitions of a two-leg bosonic ladder in an artificial gauge field*. Phys. Rev. B **97**, 174523 (2018).
- [205] M. Calvanese Strinati, R. Berkovits, and E. Shimshoni. *Emergent bosons in the fermionic two-leg flux ladder*. Phys. Rev. B **100**, 245149 (2019).
- [206] E. Coira, P. Barmettler, T. Giamarchi, and C. Kollath. *Finite-temperature dynamical correlations for the dimerized spin- $\frac{1}{2}$  chain*. Phys. Rev. B **98**, 104435 (2018).
- [207] B. Wang, X.-Y. Dong, F. N. Ünal, and A. Eckardt. *Robust and Ultrafast State Preparation by Ramping Artificial Gauge Potentials* (2020), arXiv:2009.00560.
- [208] M. C. Strinati, F. Gerbier, and L. Mazza. *Spin-gap spectroscopy in a bosonic flux ladder*. New J. Phys. **20**, 015004 (2018).
- [209] C. Repellin and N. Goldman. *Detecting Fractional Chern Insulators through Circular Dichroism*. Phys. Rev. Lett. **122**, 166801 (2019).
- [210] L. Wang, A. A. Soluyanov, and M. Troyer. *Proposal for Direct Measurement of Topological Invariants in Optical Lattices*. Phys. Rev. Lett. **110**, 166802 (2013).
- [211] T.-S. Zeng, C. Wang, and H. Zhai. *Charge Pumping of Interacting Fermion Atoms in the Synthetic Dimension*. Phys. Rev. Lett. **115**, 095302 (2015).
- [212] L. Taddia, E. Cornfeld, D. Rossini, L. Mazza, E. Sela, and R. Fazio. *Topological Fractional Pumping with Alkaline-Earth-Like Atoms in Synthetic Lattices*. Phys. Rev. Lett. **118**, 230402 (2017).
- [213] P. Prelovšek, M. Long, T. Markež, and X. Zotos. *Hall Constant of Strongly Correlated Electrons on a Ladder*. Phys. Rev. Lett. **83**, 2785–2788 (1999).

- [214] X. Zotos, F. Naef, M. Long, and P. Prelovšek. *Reactive Hall Response*. Phys. Rev. Lett. **85**, 377–380 (2000).
- [215] A. Lopatin, A. Georges, and T. Giamarchi. *Hall effect and interchain magneto-optical properties of coupled Luttinger liquids*. Phys. Rev. B **63**, 075109 (2001).
- [216] G. León, C. Berthod, and T. Giamarchi. *Hall effect in strongly correlated low-dimensional systems*. Phys. Rev. B **75**, 195123 (2007).
- [217] S. D. Huber and N. H. Lindner. *Topological transitions for lattice bosons in a magnetic field*. Proc. Natl. Acad. Sci. USA **108**, 19925–19930 (2011).
- [218] A. Auerbach. *Hall Number of Strongly Correlated Metals*. Phys. Rev. Lett. **121**, 066601 (2018).
- [219] S. Greschner, M. Filippone, and T. Giamarchi. *Universal Hall Response in Interacting Quantum Systems*. Phys. Rev. Lett. **122**, 083402 (2019).
- [220] M. Filippone, C.-E. Bardyn, S. Greschner, and T. Giamarchi. *Vanishing Hall Response of Charged Fermions in a Transverse Magnetic Field*. Phys. Rev. Lett. **123**, 086803 (2019).
- [221] F. Kolley, M. Piraud, I. McCulloch, U. Schollwöck, and F. Heidrich-Meisner. *Strongly interacting bosons on a three-leg ladder in the presence of a homogeneous flux*. New J. Phys. **17**, 092001 (2015).
- [222] S. Greschner and F. Heidrich-Meisner. *Quantum phases of strongly interacting bosons on a two-leg Haldane ladder*. Phys. Rev. A **97**, 033619 (2018).
- [223] S. Barbarino, L. Taddia, D. Rossini, L. Mazza, and R. Fazio. *Magnetic crystals and helical liquids in alkaline-earth fermionic gases*. Nat. Commun. **6**, 8134 (2015).
- [224] J. Eisert, M. Cramer, and M. B. Plenio. *Colloquium: Area laws for the entanglement entropy*. Rev. Mod. Phys. **82**, 277–306 (2010).
- [225] D. N. Page. *Average entropy of a subsystem*. Phys. Rev. Lett. **71**, 1291–1294 (1993).
- [226] S. K. Foong and S. Kanno. *Proof of Page’s conjecture on the average entropy of a subsystem*. Phys. Rev. Lett. **72**, 1148–1151 (1994).
- [227] S. Sen. *Average Entropy of a Quantum Subsystem*. Phys. Rev. Lett. **77**, 1–3 (1996).

- [228] F. Verstraete and J. I. Cirac. *Matrix product states represent ground states faithfully*. Phys. Rev. B **73**, 094423 (2006).
- [229] N. Schuch, M. M. Wolf, F. Verstraete, and J. I. Cirac. *Entropy Scaling and Simulability by Matrix Product States*. Phys. Rev. Lett. **100**, 030504 (2008).
- [230] M. B. Hastings. *An area law for one-dimensional quantum systems*. J. Stat. Mech. Theor. Exp. **2007**, P08024 (2007).
- [231] G. Vidal, J. I. Latorre, E. Rico, and A. Kitaev. *Entanglement in Quantum Critical Phenomena*. Phys. Rev. Lett. **90**, 227902 (2003).
- [232] T. Barthel, M.-C. Chung, and U. Schollwöck. *Entanglement scaling in critical two-dimensional fermionic and bosonic systems*. Phys. Rev. A **74**, 022329 (2006).
- [233] I. P. McCulloch. *From density-matrix renormalization group to matrix product states*. J. Stat. Mech. Theor. Exp. **2007**, P10014 (2007).
- [234] G. M. Crosswhite, A. C. Doherty, and G. Vidal. *Applying matrix product operators to model systems with long-range interactions*. Phys. Rev. B **78**, 035116 (2008).
- [235] G. M. Crosswhite and D. Bacon. *Finite automata for caching in matrix product algorithms*. Phys. Rev. A **78**, 012356 (2008).
- [236] F. Fröwis, V. Nebendahl, and W. Dür. *Tensor operators: Constructions and applications for long-range interaction systems*. Phys. Rev. A **81**, 062337 (2010).
- [237] B. Pirvu, V. Murg, J. I. Cirac, and F. Verstraete. *Matrix product operator representations*. New J. Phys. **12**, 025012 (2010).
- [238] M. L. Wall and L. D. Carr. *Out-of-equilibrium dynamics with matrix product states*. New J. Phys. **14**, 125015 (2012).
- [239] J. Motruk, M. P. Zaletel, R. S. K. Mong, and F. Pollmann. *Density matrix renormalization group on a cylinder in mixed real and momentum space*. Phys. Rev. B **93**, 155139 (2016).
- [240] S. Paeckel, T. Köhler, and S. R. Manmana. *Automated construction of  $U(1)$ -invariant matrix-product operators from graph representations*. SciPost Phys. **3**, 035 (2017).
- [241] C. Hubig, I. P. McCulloch, and U. Schollwöck. *Generic construction of efficient matrix product operators*. Phys. Rev. B **95**, 035129 (2017).

- [242] I. P. McCulloch. *The matrix product toolkit*. URL <https://people.smp.uq.edu.au/IanMcCulloch/mptoolkit/>.
- [243] M. Fishman, E. M. Stoudenmire, and S. R. White. *Itensor library*. URL <http://itensor.org/>.
- [244] J. Hauschild and F. Pollmann. *Efficient numerical simulations with Tensor Networks: Tensor Network Python (TeNPy)*. SciPost Phys. Lect. Notes **5** (2018).
- [245] C. Hubig, F. Lachenmaier, N.-O. Linden, T. Reinhard, L. Stenzel, A. Swoboda, and M. Grundner. *The SYTEN toolkit*. URL <https://syten.eu>.
- [246] C. Hubig. *Abelian and non-abelian symmetries in infinite projected entangled pair states*. SciPost Phys. **5**, 47 (2018).
- [247] I. P. McCulloch and M. Gulácsi. *The non-abelian density matrix renormalization group algorithm*. Europhys. Lett. **57**, 852–858 (2002).
- [248] A. Weichselbaum. *Non-abelian symmetries in tensor networks: A quantum symmetry space approach*. Ann. Phys. **327**, 2972–3047 (2012).
- [249] C. Hubig. *Symmetry-Protected Tensor Networks*. PhD thesis, LMU München (2017). URL <https://edoc.ub.uni-muenchen.de/21348/>.
- [250] C. Hubig, I. P. McCulloch, U. Schollwöck, and F. A. Wolf. *Strictly single-site DMRG algorithm with subspace expansion*. Phys. Rev. B **91**, 155115 (2015).
- [251] C. Lanczos. *An iteration method for the solution of the eigenvalue problem of linear differential and integral operators*. J. Res. Natl. Bur. Stand. **45**, 255–282 (1950).
- [252] E. R. Davidson and W. J. Thompson. *Monster matrices: Their eigenvalues and eigenvectors*. Comput. Phys. **7**, 519–522 (1993).
- [253] G. L. G. Sleijpen and H. A. Van der Vorst. *A Jacobi–Davidson Iteration Method for Linear Eigenvalue Problems*. SIAM J. Matrix Anal. Appl. **17**, 401–425 (1996).
- [254] N. Schuch, I. Cirac, and F. Verstraete. *Computational Difficulty of Finding Matrix Product Ground States*. Phys. Rev. Lett. **100**, 250501 (2008).
- [255] C. Hubig, J. Haegeman, and U. Schollwöck. *Error estimates for extrapolations with matrix-product states*. Phys. Rev. B **97**, 045125 (2018).
- [256] R. J. Baxter. *Dimers on a Rectangular Lattice*. J. Math. Phys. **9**, 650–654 (1968).

- [257] M. Fannes, B. Nachtergaele, and R. F. Werner. *Exact antiferromagnetic ground states of quantum spin chains*. Europhys. Lett. **10**, 633–637 (1989).
- [258] M. Fannes, B. Nachtergaele, and R. F. Werner. *Finitely correlated states on quantum spin chains*. Comm. Math. Phys. **144**, 443–490 (1992).
- [259] S. Östlund and S. Rommer. *Thermodynamic Limit of Density Matrix Renormalization*. Phys. Rev. Lett. **75**, 3537–3540 (1995).
- [260] S. Rommer and S. Östlund. *Class of ansatz wave functions for one-dimensional spin systems and their relation to the density matrix renormalization group*. Phys. Rev. B **55**, 2164–2181 (1997).
- [261] J. Dukelsky, M. A. Martín-Delgado, T. Nishino, and G. Sierra. *Equivalence of the variational matrix product method and the density matrix renormalization group applied to spin chains*. Europhys. Lett. **43**, 457–462 (1998).
- [262] I. P. McCulloch. *Infinite size density matrix renormalization group, revisited* (2008), arXiv:0804.2509.
- [263] A. J. Daley, C. Kollath, U. Schollwöck, and G. Vidal. *Time-dependent density-matrix renormalization-group using adaptive effective Hilbert spaces*. J. Stat. Mech. Theor. Exp. **2004**, P04005 (2004).
- [264] B. Bruognolo, Z. Zhu, S. R. White, and E. M. Stoudenmire. *Matrix product state techniques for two-dimensional systems at finite temperature* (2017), arXiv:1705.05578.
- [265] J. Hauschild, E. Leviatan, J. H. Bardarson, E. Altman, M. P. Zaletel, and F. Pollmann. *Finding purifications with minimal entanglement*. Phys. Rev. B **98**, 235163 (2018).
- [266] T. Barthel. *Matrix product purifications for canonical ensembles and quantum number distributions*. Phys. Rev. B **94**, 115157 (2016).
- [267] M. P. Zaletel, R. S. K. Mong, C. Karrasch, J. E. Moore, and F. Pollmann. *Time-evolving a matrix product state with long-ranged interactions*. Phys. Rev. B **91**, 165112 (2015).
- [268] A. C. Tiegel, S. R. Manmana, T. Pruschke, and A. Honecker. *Matrix product state formulation of frequency-space dynamics at finite temperatures*. Phys. Rev. B **90**, 060406 (2014).

- [269] G. Alvarez. *Production of minimally entangled typical thermal states with the Krylov-space approach*. Phys. Rev. B **87**, 245130 (2013).
- [270] C. Karrasch, J. H. Bardarson, and J. E. Moore. *Reducing the numerical effort of finite-temperature density matrix renormalization group calculations*. New J. Phys. **15**, 083031 (2013).
- [271] C. Karrasch, J. H. Bardarson, and J. E. Moore. *Finite-Temperature Dynamical Density Matrix Renormalization Group and the Drude Weight of Spin-1/2 Chains*. Phys. Rev. Lett. **108**, 227206 (2012).
- [272] E. M. Stoudenmire and S. R. White. *Minimally entangled typical thermal state algorithms*. New J. Phys. **12**, 055026 (2010).
- [273] T. Barthel, U. Schollwöck, and S. R. White. *Spectral functions in one-dimensional quantum systems at finite temperature using the density matrix renormalization group*. Phys. Rev. B **79**, 245101 (2009).
- [274] A. E. Feiguin and S. R. White. *Finite-temperature density matrix renormalization using an enlarged Hilbert space*. Phys. Rev. B **72**, 220401 (2005).
- [275] F. Verstraete, J. J. García-Ripoll, and J. I. Cirac. *Matrix Product Density Operators: Simulation of Finite-Temperature and Dissipative Systems*. Phys. Rev. Lett. **93**, 207204 (2004).
- [276] R. J. Bursill, T. Xiang, and G. A. Gehring. *The density matrix renormalization group for a quantum spin chain at non-zero temperature*. J. Phys. Condens. Matter **8**, L583 (1996).
- [277] A. E. Feiguin and G. A. Fiete. *Spectral properties of a spin-incoherent Luttinger liquid*. Phys. Rev. B **81**, 075108 (2010).
- [278] A. Nocera and G. Alvarez. *Symmetry-conserving purification of quantum states within the density matrix renormalization group*. Phys. Rev. B **93**, 045137 (2016).
- [279] T. Köhler, S. Rajpurohit, O. Schumann, S. Paeckel, F. R. A. Biebl, M. Sotoudeh, S. C. Kramer, P. E. Blöchl, S. Kehrein, and S. R. Manmana. *Relaxation of photoexcitations in polaron-induced magnetic microstructures*. Phys. Rev. B **97**, 235120 (2018).
- [280] M. Suzuki. *Generalized Trotter's formula and systematic approximants of exponential operators and inner derivations with applications to many-body problems*. Comm. Math. Phys. **51**, 183–190 (1976).

- [281] S. R. White and A. E. Feiguin. *Real-Time Evolution Using the Density Matrix Renormalization Group*. Phys. Rev. Lett. **93**, 076401 (2004).
- [282] J. J. García-Ripoll. *Time evolution of Matrix Product States*. New J. Phys. **8**, 305 (2006).
- [283] P. E. Dargel, A. Wöllert, A. Honecker, I. P. McCulloch, U. Schollwöck, and T. Pruschke. *Lanczos algorithm with matrix product states for dynamical correlation functions*. Phys. Rev. B **85**, 205119 (2012).
- [284] J. Haegeman, J. I. Cirac, T. J. Osborne, I. Pižorn, H. Verschelde, and F. Verstraete. *Time-Dependent Variational Principle for Quantum Lattices*. Phys. Rev. Lett. **107**, 070601 (2011).
- [285] J. Haegeman, C. Lubich, I. Oseledets, B. Vandereycken, and F. Verstraete. *Unifying time evolution and optimization with matrix product states*. Phys. Rev. B **94**, 165116 (2016).
- [286] M. Yang and S. R. White. *Time-dependent variational principle with ancillary Krylov subspace*. Phys. Rev. B **102**, 094315 (2020).
- [287] N. Schuch, M. M. Wolf, K. G. H. Vollbrecht, and J. I. Cirac. *On entropy growth and the hardness of simulating time evolution*. New J. Phys. **10**, 033032 (2008).
- [288] M. Lysebo and L. Veseth. *Feshbach resonances and transition rates for cold homonuclear collisions between  $^{39}\text{K}$  and  $^{41}\text{K}$  atoms*. Phys. Rev. A **81**, 032702 (2010).
- [289] L. Tanzi, C. R. Cabrera, J. Sanz, P. Cheiney, M. Tomza, and L. Tarruell. *Feshbach resonances in potassium Bose-Bose mixtures*. Phys. Rev. A **98**, 062712 (2018).
- [290] F. Zhan, J. Sabbatini, M. J. Davis, and I. P. McCulloch. *Miscible-immiscible quantum phase transition in coupled two-component Bose-Einstein condensates in one-dimensional optical lattices*. Phys. Rev. A **90**, 023630 (2014).
- [291] L. Barbiero, M. Abad, and A. Recati. *Magnetic phase transition in coherently coupled Bose gases in optical lattices*. Phys. Rev. A **93**, 033645 (2016).
- [292] P. Calabrese and J. Cardy. *Entanglement entropy and quantum field theory*. J. Stat. Mech. Theory and Exp. **2004**, P06002 (2004).
- [293] D. McKay and B. DeMarco. *Cooling in strongly correlated optical lattices: prospects and challenges*. Rep. Prog. Phys. **74**, 054401 (2011).

- [294] A. Polkovnikov, K. Sengupta, A. Silva, and M. Vengalattore. *Colloquium: Nonequilibrium dynamics of closed interacting quantum systems*. Rev. Mod. Phys. **83**, 863–883 (2011).
- [295] S. Badoux, W. Tabis, F. Laliberté, et al. *Change of carrier density at the pseudogap critical point of a cuprate superconductor*. Nature (London) **531**, 210–214 (2016).
- [296] L. Ella, A. Rozen, J. Birkbeck, M. Ben-Shalom, D. Perello, J. Zultak, T. Taniguchi, K. Watanabe, A. K. Geim, S. Ilani, and J. A. Sulpizio. *Simultaneous voltage and current density imaging of flowing electrons in two dimensions*. Nat. Nanotechnol. **14**, 480–487 (2019).
- [297] M. D. Bachmann, A. L. Sharpe, A. W. Barnard, C. Putzke, M. König, S. Khim, D. Goldhaber-Gordon, A. P. Mackenzie, and P. J. Moll. *Super-geometric electron focusing on the hexagonal Fermi surface of PdCoO<sub>2</sub>*. Nat. Commun. **10**, 5081 (2019).
- [298] G. Salerno, H. M. Price, M. Lebrat, S. Häusler, T. Esslinger, L. Corman, J.-P. Brantut, and N. Goldman. *Quantized Hall Conductance of a Single Atomic Wire: A Proposal Based on Synthetic Dimensions*. Phys. Rev. X **9**, 041001 (2019).